Development and characterization of high-k sub-nanometric laminates of binary oxides for applications in high density capacitances

Mudit Upadhyay

Normandie Université

THÈSE

Pour obtenir le diplôme de doctorat

Spécialité ELECTRONIQUE, MICROELECTRONIQUE, OPTIQUE ET LASERS, OPTOELECTRONIQUE MICROONDES

Préparée au sein de l'Université de Caen Normandie

Development and Characterization of high-k Sub-nanometric Laminates of Binary Oxides for Applications in High Density Capacitances

Présentée et soutenue par
MUDIT UPADHYAY

Thèse soutenue le 19/03/2021 devant le jury composé de		
M. EMMANUEL DEFAY	Chercheur, Luxembourg Institute of Sciences and Tec	Rapporteur du jury
M. ALAIN SYLVESTRE	Professeur des universités, Université Grenoble 1 Joseph Fourier	Rapporteur du jury
M. FLORENT LALLEMAND	Ingénieur, Murata Integrated Passive Solutions	Membre du jury
M. WILFRID PRELLIER	Directeur de recherche au CNRS, ENSICAEN	Membre du jury
M. JÉRÔME WOLFMAN	Chargé de recherche au CNRS, Université de Tours François Rabelais	Membre du jury
MME MARYLINE GUILLOUX-VIRY	Professeur des universités, Université Rennes 1	Président du jury
MME ULRIKE LUDERS	Directeur de recherche au CNRS, ENSICAEN	Directeur de thèse

Thèse dirigée par ULRIKE LUDERS, Laboratoire de cristallographie et sciences des materiaux (Caen)

UNIVERSITÉ CAEN NORMANDIE

ENSI CAEN
ÉCOLE PUBLIQUE D'INGÉNIEURS
CENTRE DE RECHERCHE

ED 591 PSIME

RISM

Table of Content

LIST OF TABLE

List of Figures

ACKNOWLEDGEMENTS

Finally, I finished writing my thesis and I cannot express the immense happiness I am feeling right now. This thesis is not just a document but my journey of 3 years in CRISMAT laboratory. I remember my first day in CRISMAT when I lost my way out from the long corridors of the lab and now after 3 years, I have beautiful memories and a story from each corner of those corridors. However, my 3 years in CRISMAT could have been much better if 2020 would not be one of these years. But I can not thank enough to all the amazing people of the lab who helped me to keep going even through the tough times of lockdown and horror of this pandemic.

First and foremost, I wish to thank my supervisor Dr Ulrike LÜDERS for being so supportive and helpful during these 3 years of my project. From helping me find my first apartment to helping me prepare for my thesis defense by listening to my 45 minutes long mock presentations again and again, Ulrike was such a great support as she was always encouraging and motivating me. Thanks to her for helping me understand the science of dielectrics and broaden my scientific mindset with valuable suggestions and comments. This project could not have been complete without her constant guidance and feedback.

Thin-film depositions were time taking and problematic sometimes, as the machine does not always work the way we want but I was lucky to have Bernard Mercy in the lab for helping me resolving those issues and teaching me insights about the technique. I greatly appreciate his help I received throughout 3 years. My thanks also go out to Arnaud Fouchet and Adrian David for helping me learn XRD and AFM and also for their support whenever I needed it.

I would like to thank Stéphanie Gascoin and Sophie Dufourd for helping me get some of the crucial XRD data of my samples, even when I asked them for some measurements urgently, they never said no.

Even when the XRD machine was not working in our lab I never had to stop my experimental work because of Clara Grygiel (GANIL Caen). She helped me to collect the XRR data of some calibration samples. Without her cooperation, this project could have been delayed by months. Thanks to Clara for all this help.

A special thanks to the members of my CSI committee: Dr Ranjith Ramadurai and Dr Christelle Harnois, for their valuable suggestions and feedback during the evaluation of my

project each year. The discussions with them helped me to get a different perspective of my work and their feedback helped me to improve my knowledge.

I am also very grateful to all the administrative staff at the CRISMAT laboratory, especially Veronique Baclet, Elizabeth and Marie Slavary for helping me with all the administrative work and making my life hustle free for three years. A very special thank goes to the director of the CRISMAT laboratory, Dr Wilfrid PRELLIER, Without his help and support this project would not have been finished.

My deep appreciation goes out to the members of the G2E laboratory, Grenoble. Their excellent support for the high-temperature dielectric studies has made an invaluable contribution to my PhD. I am also grateful to them for the amazing time I spent with them in the Alpes.

Many thanks to the members of GREMAN laboratory, Tours: Jerome Wolfman and Beatrice Negulescu for letting me use their laboratory and helping me finish the critical dielectric measurements. And special thanks goes to Antoine Ruyter for introducing me to the GREMAN lab and helping me with my stay in Tours.

Special acknowledgement goes to my office mates Antoine Ruyter, Ali Fakhi for constantly ~~disturbing~~ motivating me always. I highly appreciate the efforts you guys put in to make me come to the office early in the morning, but I am sorry that you never succeed. Thanks for making the office so much fun.

I truly understood the importance of the long coffee breaks with Marie, Deepak, Mariya, Aimane and Tathamay. Thank you for making life so much fun **"because"** you guys are the best.

I am indebted to all my friends Moussa, Marie, Ali Fakhi, Maryline, Oualyd, Abhishek, Mufeed, Mart, Pavan, Neetu, Radia, Abdel, Krishnendu, Alvaro, Vishant, Shivang, Amit and Nishu for always being there (specially on Friday nights). Without them, the life would have been so boring.

And finally, to my family, my emotional support. Thank you very much for supporting me no matter how wrong I was. Without their support, I cannot imagine finishing this journey.

Chapter 1 Introduction

Growing economies and the developing world in the 21st century lead to high energy consumption. This became evident in the current scenario of the COVID-19, during the lockdown, when the trembling economies throughout the world were leading to a low energy consumption. These high energy demands are and will be growing within the coming years. This is the reason a lot of research has been done in the last few decades to develop various energy generation technologies. Apart from generating, efficiently storing the energy is also a great challenge, and it demands the research and development of devices and technologies. Fuel cells, batteries, electrochemical supercapacitors, and dielectric capacitors are commercially available devices. These devices can be differentiated and used in different applications based on their energy storage time. Batteries and fuel cell possess high energy density, but their charging and discharging takes longer time due to the slow movement of the ionic charge carriers. Electrochemical supercapacitors and dielectric capacitors possess high power density and have an essential role in power electronics. Dielectric capacitors have attracted attention because of their extremely fast power density and charging rate. These high-density capacitors can have many applications including microprocessor decoupling capacitors, analog/filter capacitors, RF bypass capacitors, DRAM storage cell capacitors, and power electronic flying capacitors [1,2,3]. These dielectric capacitors are the main building components of transistors and hence the processors and electronic devices.

The electronic industry has seen a tremendous growth in last 50 years. From the first programable computer “ENIAC” (1945) to the smallest programmable Michigon micromote M3 (2015), it was possible to reduce the size of the devices and improve the performance by many orders of magnitude. This all was possible because of the use of transistors in the electronic devices at the first place, and the following increase in their density in the integrated circuits. In 1978, Moore observed that in order to improve the performance of the electronic devices, the number of transistors placed on a single chip would be doubled every year [4,5]. Figure 1 represents the revolutionary law of Moore; it shows the prediction of the growth of the number of components on a chip with each year [6]. However, in 1995, Moore revised his predictions and

expected that the number of transistors would be doubling every 2 to 3 years. This observation by Moore can be considered as a revolutionary law in electronics industries. Based on Moore's predictions, many different components were kept on a single circuit performing various functions and improving circuit performance, at the same time, the manufacturing cost of the device can be reduced. This miniaturization of devices primarily concerns MOSFET and other CMOS devices, with a small imprint on the chip while performing multiple functions.

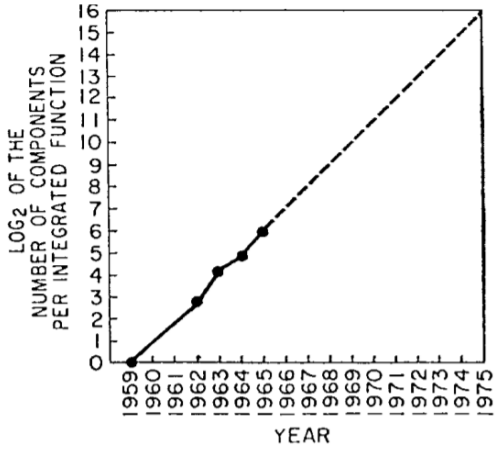

Figure 1 Moore's original prediction until 1975 [5]

In order to keep respect the voltage scaling, the reduction in the transistor size leads to the thinning of the dielectric layer, historically SiO_2. SiO_2 has a dielectric constant of 3.8 and was highly used as the dielectric layer on Si based integrated circuits because of its insulating properties, as well as the easy growth process on Si substrates. Problems arise as the SiO_2 layer becomes too thin (<1.2 nm), as the quantum tunneling effect causes high dielectric losses and leakage currents through the SiO_2 layer. Figure 2 shows a schematic representation of a field effect transistor and the black layer indicates the dielectric layer, and a TEM image of the SiO_2 layer. The tunneling current through the dielectric layer created a need to replace SiO_2 with a material having a higher dielectric constant than SiO_2, so that a thick layer of the material can be used in FETs. Thus, we need to improve the capacitive density by using a material with high dielectric constant. These high-density dielectric capacitors will further promote the miniaturization, and the development of compact and lightweight electronic devices.

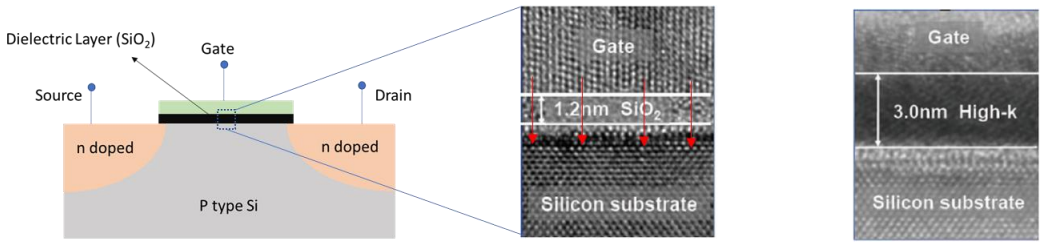

Figure 2 Schematic representation of CMOS transistor and the zoomed TEM image of the SiO_2 layer used as a dielectric oxide

This thesis is an effort to develop dielectric capacitors with high capacitance density. In order to improve the density of the capacitors, two possible ways were identified: (i) device shape engineering and (ii) dielectric material development. We have chosen the second one. We develop dielectric capacitors with different dielectric materials aiming at high dielectric constants, based on a controlled Maxwell Wagner effect. The following sections of this chapter will take you through the basics of capacitors and dielectric materials, highlighting the central concepts important for the understanding of the following experimental work.

1.1. Basics of dielectric capacitors

Figure 3 shows the typical example of a parallel plate capacitor consisting of two conducting plates separated by the dielectric material. The ability to store charges and energy by the capacitor is termed as the capacitance, which depends on the physical dimensions of the capacitor, but also on the characteristics of the dielectric. In case of the parallel plate capacitor as shown in Figure 3, the capacitance is inversely proportional to the separation distance between the plates and directly proportional to the area of the plates. It can be expressed as the following relation:

$$C = \frac{kA\varepsilon_0}{t} \qquad (1)$$

where C represents the capacitance, k the dielectric permittivity of the material between the parallel plates, ε_0 is the electric permittivity of vacuum with the value 8.854 x 10^{-12} Fm^{-1}, A is the area of the plates and t is the separation distance between the plates.

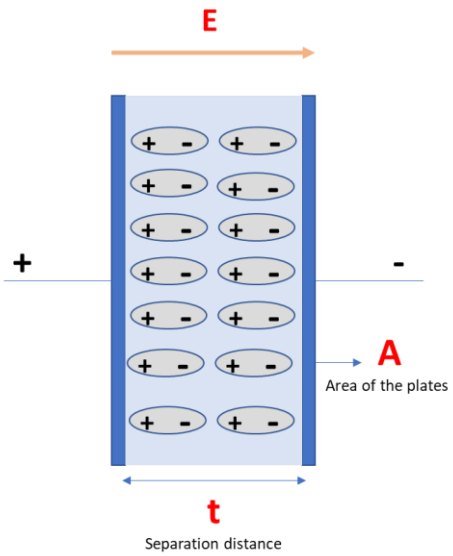

Figure 3 Schematic representation of a parallel plate capacitor under the application of an external electric field

When an electric field E is applied to the capacitor, the charges in the dielectric material orient themselves according to the polarity of the electric field and a depolarization field is generated internally, opposing the applied electric field. A detailed explanation of the process is presented in next section (1.2).

In order to improve the capacitance density of a given capacitor, the following methods can be used:

(i) Changing the dimensions of the capacitor

By an increase of the surface area (A) of the electrodes and by decreasing the separation distance between electrodes, the capacitance can be improved (equation (1)). In 1978, Bean proposed a method so that the area of the electrodes can be improved, without changing the external device dimensions, by etching ridges in the Si substrate [7]. These ridges enlarge the internal capacitor area while keeping the Si substrate area of the capacitor constant [8]. Figure 4 shows the schematics of a more up-to-date 3D Si substrate with a dielectric layer coating the internal surface of the pores inside the Si substrate. The pores are afterwards filled with the top electrode material, giving electrical access to the dielectric in the pores. However, the drawback of this technology is the challenge to grow a homogeneous dielectric layer in the trenches. This challenge limits the use of deposition techniques and the dielectric material. Deposition of complex oxides is still hard to be achieved homogeneously in these trenches. Hence, only a few

binary oxides can be grown for the moment in these trenches, using deposition techniques like Atomic Layer deposition (ALD) and thermal oxidation [8].

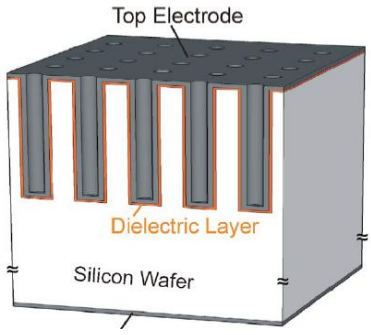

Figure 4 Trenches in Si substrate filled with the dielectric material and the top electrode, and hence the active area of the electrode is high. [8]

Similarly, we can increase the capacitance by decreasing the separation distance between the electrodes (equation (1)), i.e. the thickness of the dielectric. However, the minimum thickness of the dielectric layer is restricted by the requirement for high breakdown voltages, as for power devices apart from having high capacitance, the endurance under high voltage is a crucial factor [9]. Also, the small thickness of the dielectric layer can create problems of tunneling currents. This problem has been explored well in the case of SiO_2 layer in gate oxide applications in the last decade [10,11].

Based on these demerits explained above, changing the dimensions of the capacitor is still a difficult solution to increase the capacitance density, although it is used now in micro-electronics industry in a certain extent.

(ii) Replacing the dielectric material with a high dielectric constant material

A promising way to improve the capacitive density is by filling the separation between the plates with a material which has a high dielectric constant k. In this thesis, the development of new materials was carried out in order to have a high dielectric constant, combined with low losses.

1.2. Introduction to dielectrics

Dielectrics are electrically insulating materials. An ideal dielectric would possess an infinite electrical resistivity, but no real dielectric is a perfect insulator. According to band theory, we can classify dielectric materials (insulators) as a material having an energy band gap. For practical reasons, it is favorable to use materials with a band gap of at least about 4 eV. This large band gap in dielectrics reduces the possibility of the transfer of electrons from the valence band to the conduction band, and therefore the establishment of currents.

In general, metal oxides are considered as suitable dielectrics. Their bond character is primarily ionic, where the bonding electrons are strongly localized. The movement of these charges in dielectrics can be only possible at the cost of a high energy. An external electric field can only displace these charges to a small extent, unlike in metals and semiconductors. This small displacement can shift the center of gravity of the positive charges as compared to the negative charges, generating a polarization in the dielectric. However, when a sufficiently high electric field is applied to the dielectric material, the dielectric behaves like a conductor as the electrons can have sufficient energy to cross the energy gap and reach the conduction band. As no dielectric is perfect, there is always a conduction component associated to a storage of energy, called dielectric losses. Low dielectric losses are related to a low dissipation of energy, which is an important aspect to select the right dielectric material for capacitor applications.

1.2.1. Dielectric polarization

When a dielectric material is placed in an external electric field, the positive and negative charges are displaced from their equilibrium positions throughout the dielectric. This displacement causes the formation of dipoles with some dipole moment in the direction of the electric field. This dielectric polarization (P) can be defined as the total dipole moment per unit volume of the material and can be expressed as:

$$P = \sum q_n r_n \qquad (2)$$

where q_n is the charge and r_n its position vector. The displacement of charges within the material gives rise to a local electrical field opposing the applied electrical field, which is called

depolarization field. The total polarization in a material can contain different contributions: electronic polarization, ionic polarization, interfacial/space charge polarization and dipolar polarization. These polarization mechanisms are dependent on the frequency of the applied electric field, and are explained in the following:

(i) Electronic polarization:

The displacement of the center of mass of the electron cloud with respect to the center of mass of the atomic nucleus gives rise to the electronic polarization in materials, as shown in Figure 5(a). The frequency of the applied electric field has an exceedingly small influence on the electronic polarization, and in the optical frequency range (10^{10} - 10^{16} Hz), the entire polarization in any dielectric materials arise from the electronic contributions only (Figure 6).

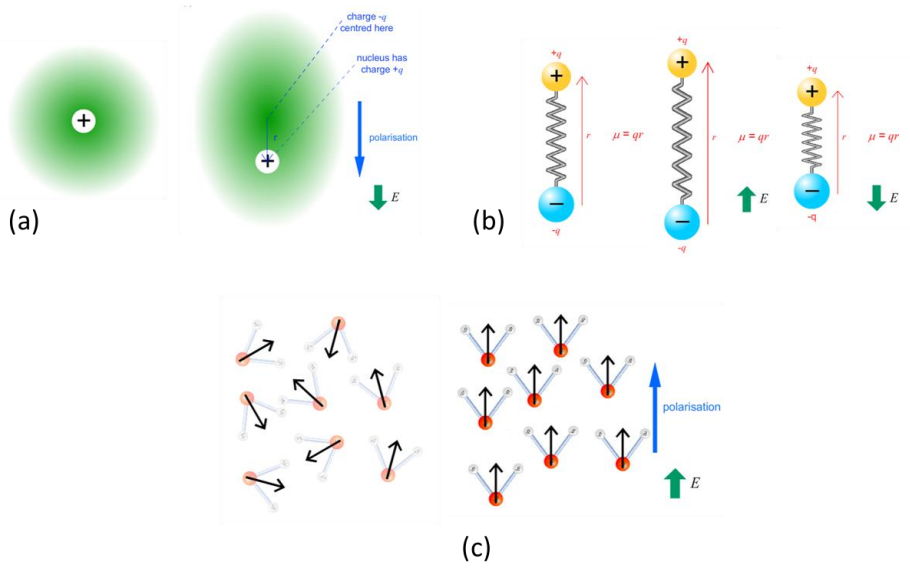

Figure 5 Schematic representation of different polarization mechanisms under the influence of an external electric field: (a) electronic polarization, (b) ionic polarization, and (c) dipolar polarization.

(ii) Ionic polarization

In ionic materials, the displacement of negative ions with respect to the positive ions under the electrical field gives rise to the ionic polarization (Figure 5(b)). The ionic polarization is dependent on the frequency of the applied field, and at high frequency, it has no contributions in total polarization of the material. This is due to the fact that ions are heavy, and they exert inertia

upon the displacement force of the external field. Therefore, the effect is restricted to relatively low frequencies (Figure 6).

(iii) Dipolar polarization

Figure 5(c) shows an example of dipolar polarization under the influence of the external field. When materials possess permanent dipoles oriented in random directions in the absence of an applied field, resulting in a net dipole moment of zero, in an external field, the dipoles reorient themselves according to the direction of the applied field. This reorientation of dipoles gives rise a net dipole moment in the material called dipolar polarization—for example for H_2O, CO_2 … Similar to the ionic polarization, the dipolar polarization also becomes negligible at high frequencies of the applied field.

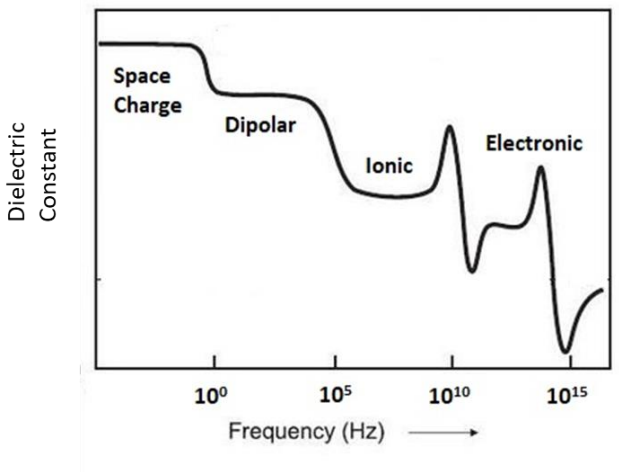

Figure 6 Dielectric polarization as a function of the frequency of applied electric field (adapted from Wikipedia)

(iv) Space charge polarization

Interfacial or space charge polarization occurs in the case of heterogeneous materials. The accumulation of charges under an applied field at an internal interface between two materials, or between two regions within a material, gives rise to the space charge or interfacial polarization. This kind of polarization has a particular interest in the device design, as the used materials in devices are mostly heterogeneous. This polarization affects free charges in the material and is most common in the case of amorphous and polycrystalline materials.

From the above discussion, it is clear that the dielectric polarization is directly related to the applied electric field. This relation can be expressed in terms of the dielectric susceptibility (χ) of the material as:

$$P = \varepsilon_0 \chi^* E \qquad (3)$$

where E is the macroscopic electric field. The macroscopic electric field in the matter is a vector sum of the applied field and the depolarization field generated in the material, and is directly proportional to the dielectric displacement (D) and the polarization (P) as:

$$D = \varepsilon_0 E + P \qquad (4)$$

From equations (*3*) and *(4)* we can write

$$D = \varepsilon_0 (1 + \chi^*) E \qquad (5)$$

where complex dielectric permittivity $\varepsilon^* = 1 + \chi^*$and the susceptibility of material are related, and we can rewrite Equation 5 as:

$$D = \varepsilon_0 \varepsilon^* E \qquad (6)$$

The complex dielectric permittivity ε* of the material is a function of the time-dependent electric field and changes with its frequency or the temperature. For the characterization of dielectric materials, often the term dielectric constant (ratio of dielectric permittivity of material and the permittivity of free space) is used, as the dielectric constant is an intrinsic property of the material and depends on its structure and density. In this thesis, we have analyzed the dielectric constant of the deposited films and laminates, and we have studied the effect of various parameters on the dielectric constant in order to optimize its value.

The relaxation phenomena in dielectrics are related to fluctuations of dipoles in an electric field. The drift motion of mobile charge carriers (electrons, ions or charged defects) causes conductive contributions to the dielectric response. The frequency dependent microprocesses within a material under the application of a time-dependent electric field give rise to the changes in the dielectric displacements (equation 5). The applied time dependent electric field ($E = E_0 e^{-iwt}$) gives rise to the complex dielectric constant:

$$\varepsilon^* = \varepsilon' - i\varepsilon'' \qquad (7)$$

where ε' represents the real part of dielectric permittivity, also called k in this thesis, related to charge storage and ε'' is the imaginary part of the permittivity related to the conduction of charge carriers in the dielectric or the energy dissipated through the dielectric. The dependence of the complex dielectric function on angular frequency (ω) and the temperature arises from different processes: microscopic fluctuations of dipoles, translational diffusion of mobile charges and the separation of charges at interfaces… We can express this complex dielectric constant as the sum of the high frequency dielectric constant (ε_∞) related to the instantaneous polarization (P_∞) due to the electron displacement with respect to their nuclei, and a time dependent part of the dielectric constant related to the polarization caused by the orientation of dipoles in the electric field (E). Mathematically, we can represent the complex dielectric constant in terms of time dependent dielectric constant ε(t) as:

$$\varepsilon^*(\omega) = \varepsilon_\infty - \int_0^\infty \frac{d\varepsilon(t)}{d(t)} e^{(-i\omega t)}\, dt \qquad (8)$$

where ε(t) can be calculated as $\varepsilon(t) = (P(t) - P_\infty) \,/\, E_0\varepsilon_0$. The real and imaginary parts of the complex dielectric constant are related to each other by the Kramer-Kronig relations [12].

As the relaxation is the change of polarization with the time dependent applied electric field, in 1929, Debye explains the simplest scenario of dielectric relaxation by considering a single relaxation time (τ_D), implying that the rate of change in the polarization with time is proportional to its value. Based on these assumptions, Debye related the complex dielectric function with the relaxation time (τ_D) and the angular frequency (ω) of the applied electric field as:

$$\varepsilon^*(\omega) = \varepsilon_\infty + \frac{\Delta\varepsilon}{1 + i\omega\tau_D} \qquad (9)$$

where $\Delta\varepsilon$ is the difference of the time dependent dielectric constant ε(t) and the instantaneous dielectric constant (ε_∞). Based on Debye's model, we can extend the complex dielectric function to include multiple time constants that relate to different processes, which is usually the case for a practical system. For example, Figure 6 shows different dielectric relaxations related to the different mechanisms at their different characteristic frequencies.

In case of non – Debye relaxation behaviors, the measured dielectric curve does not follow equation *(9)* and has an asymmetric shape with a broad loss peak. Various different model functions have been developed based on the Debye function, as for example the Cole/Cole function, Cole/Davidson function, Havriliak/Negami function. Details regarding these functions are out of scope of this thesis but can be studied from reference [12].

1.2.2. Dielectric conductivity

The time derivative of the dielectric displacement can be represented as a current density in the material, which can be expressed in terms of the time-dependent electric field and the complex conductivity of the material as

$$j = \sigma^* E = \frac{dD}{dt} \qquad (10)$$

where σ* is the complex conductivity of the material. From equation (*6*) we can get a relation between the complex conductivity σ* and the complex dielectric constant ε* under a time-dependent electric field as

$$\sigma^* = i\omega\varepsilon_0\varepsilon^* \qquad (11)$$

The real part of the complex conductivity gives the insights of the charge movements in the dielectric material. The activation energy of these charges can be calculated by analyzing the dielectric constant of the material at different temperatures. These topics will be further developed in the experimental chapters dedicated to the analysis of the conduction behavior of the dielectric films and laminates used in my thesis.

1.2.3. The Maxwell-Wagner effect

An important objective of this thesis is to obtain and control the Maxwell-Wagner effect in the layered structures consisting of alternative layers of an insulator and a semiconductor. This effect has been observed in various systems in the literature i.e. Al_2O_3/TiO_2 laminates [15,16], CCTO [15], etc. and is known to enhance spectacularly the dielectric constant of the materials. Here we present the basic understanding of the Maxwell-Wagner effect.

The Maxwell–Wagner effect is related to charge accumulation at the interface of two materials, as a result of the difference of charge carrier relaxation of these two materials.

Macroscopically, the ratio of the real parts of the dielectric constant (ε) and the conductivity (σ) describes the relaxation time $\tau = \frac{\varepsilon}{\sigma}$. Charge accumulation is allowed at the interface between two materials with different relaxation times. When an electric field is applied to this heterogeneous system, the current flows across the interface with an accumulation of the charges, giving rise to an additional contribution to the polarization. This interfacial accumulation of charge is called the Maxwell–Wagner (MW) effect and the polarization induced by these accumulated charges is known as the Maxwell – Wagner polarization.

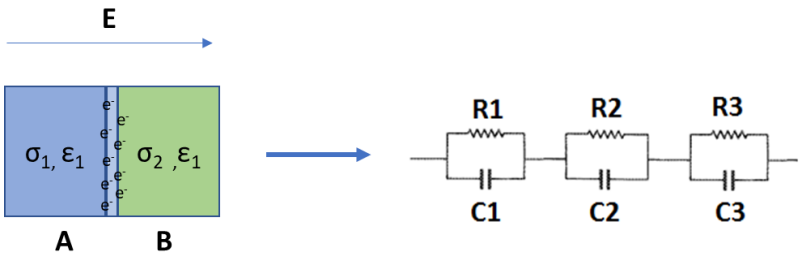

Figure 7 The interface between two materials A and B having different conductivities and dielectric constants, and its equivalent circuit

As any interfacial polarization as discussed in 1.2.1 – (iv), the MW effect is considered as a space charge polarization and occurs for a variety of heterogeneous systems including interfaces between grains and grain boundaries in polycrystalline systems [13, 14], interfaces between the electrode and the dielectric material, and also domain boundaries [17] . Figure 7 shows a schematic representation of a heterogeneous system consisting of two different materials A and B with different electrical conductivities and dielectric constants. When this system is exposed to a time-variable electrical field, mobile charges are accumulated at the interface. This accumulation of charges changes the electrical properties (σ, ε) in the proximity of the interface.

The complex dielectric function of the layered structure, as shown in Figure 7, can be expressed by the Debye relaxation equation as explained in equation *(9)* as:

$$\varepsilon^* = \varepsilon' + i\varepsilon'' = \varepsilon_\infty + \frac{\varepsilon_s - \varepsilon_\infty}{1 + i\omega\tau_m} \qquad (12)$$

If we consider that material A has a volume fraction *f* and B a volume fraction *(1-f)* in the system, we can express ε_∞ (dielectric constant at high frequency) and ε_s (dielectric constant at low frequency) as:

$$\varepsilon_S = \frac{\varepsilon_A \varepsilon_B}{\varepsilon_A f + \varepsilon_B (1-f)} \text{ and } \varepsilon_\infty = \frac{\varepsilon_A}{f} + \frac{\varepsilon_B}{(1-f)}$$

Thus, the low frequency dielectric constant of a MW system is higher than the series capacitance of the two materials, which would be the weighted sum of the reciprocal dielectric constant of the individual materials (and therefore governed by the material with the lower dielectric constant). It is also larger than the dielectric constant of the solid solution, which is the high frequency limit of the MW dielectric constant. The MW effect leads therefore to an enhancement of the macroscopic dielectric constant, which we want to use to develop innovative high k materials for the use in integrated electronics.

Due to its character of a space charge polarization, the relaxation frequency of the effect, limiting the working frequency of the material, may be quite low (Figure 6). To estimate the relaxation frequency, the relaxation time for MW polarization (τ_{MW}) can be used:

$$\tau_{MW} = \varepsilon_0 \frac{\varepsilon_A f + \varepsilon_B (1-f)}{\sigma_A f + \sigma_B (1-f)} \qquad (13)$$

Equation (13) shows that the relaxation time of the MW effect is inversely proportional to the conductivity of the materials, i.e. the lower the resistivity of the constituent materials, the higher is the working frequency. However, if the resistivities are low, losses and leakage currents may become important. Therefore, the conductivities and the dielectric constants of the constituent materials have to be optimized with care.

The equivalent circuit of the heterogeneous system is shown also in Figure 7, where three RC circuits represent the different constituents: material A, material B, and the interface. The resistance (R) is associated with the conduction current through the material, while the capacitance (C) is related to the stored charges in the material. R and C can be expressed as:

$$R = \frac{l}{\sigma A} \qquad \text{and} \qquad C = \frac{kA\varepsilon_0}{l}$$

where l is the thickness of each constituent and A is the area of the electrode. We will use this description of the MW system to analyze the dielectric properties of the laminates in detail, especially to extract the properties of the constituent materials. The technical details are described in section 2.4.3.

1.3. Dielectric Materials for integrated circuits

Since the last two decades a lot of research has been done to find the suitable dielectric material for various applications in electronics with the aim of having high capacitance density and low dielectric losses [18]. As the important electronic CMOS and FET devices are made from Si, SiO_2 was an obvious choice as a dielectric material because it is easy to grow on Si and has a dielectric constant of 3.9 with a bandgap of 8.6 eV [19]. In fact, although SiO_2 provides good insulation for charges because of its high bandgap, its capacitive density is still limited due to the low dielectric constant, far from the requirements for a high capacitance density projected by the 2002 ITRS roadmap [20]. The capacitive density of SiO_2 can be improved by reducing the dielectric thickness but it may lead to the problems of tunneling current and low breakdown voltage [10]. Hence, to avoid the problems of leakage current and low capacitive density, the adoption of a high-k material is required. Using a thick film of high-k dielectric film may potentially improve the overall electrical performances.

As the basic requirement, the new material should have a high dielectric constant and a high energy band gap. However, it has been pointed out in many studies [19], that the dielectric constants of binary oxides vary inversely with their energy band gap as shown in Figure 8. A low energy band gap of the dielectric is coupled with the reduction in the break down voltage and high dielectric losses. J. McPherson pointed out the direct relation between the breakdown voltage and the dielectric constant and found that the breakdown voltage closely follows $k^{\left(-\frac{1}{2}\right)}$ [9]. This inverse relation between dielectric constant and band gap for dielectrics is a major limitation for the selection of suitable high-k material that can improve both the capacitive density and the breakdown voltage.

For the selection of a suitable dielectric material for integrated circuits, various important factors have to be kept in mind:

(i) High dielectric constant

As pointed out by Robertson [19], the dielectric constant should be above 10, but preferably so large that for future reduction of the capacitor's size, a high layer thickness can be used to avoid

tunneling current and dielectric losses. All the materials shown in Figure 8 have a higher dielectric constant than SiO_2 and have been studied extensively.

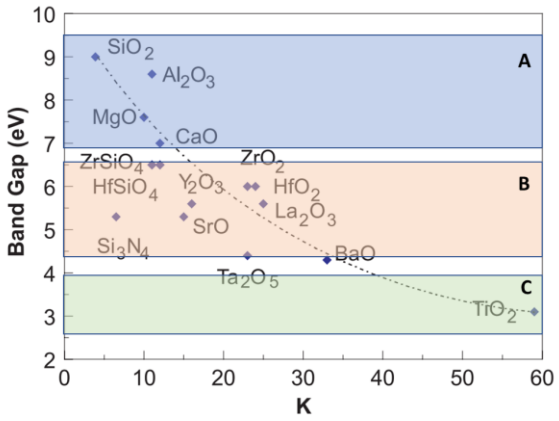

Figure 8 Static dielectric constant vs. band gap for candidate binary oxides [19]

(ii) Thermodynamic stability with Si

The thermodynamic stability with Si is an important factor and the probable high-k oxide should have a higher (negative) energy of formation than SiO_2. This would avoid the formation of a SiO_2 layer at the interface of the Si and the dielectric layer, which would reduce the total capacitance of the device. This demand will exclude the possibility of using TiO_2, Ta_2O_5 etc. even if they possess a high dielectric constant.

(iii) High band offset with Si

To avoid charge conduction because of Schottky emission into the Si from the dielectric layer, a high band offset between Si and the dielectric is required [21]. Materials like Al_2O_3, Y_2O_3 etc. have a high band offset with the Si.

(iv) Amorphous nature of the dielectric

The interface of the dielectric and the Si should be of high electrical quality (low roughness and low defects at interface). Therefore, amorphous materials are preferable over crystalline dielectrics. The amorphous layers can also be cost effective due to their easier synthesis, have isotropic dielectric properties, and have no grain boundaries, which can act as conduction pathways for the charge carriers. Amorphous films of binary oxides like HfO_2, ZrO_2, Al_2O_3 etc. have been studied to investigate this interface quality [22].

Various high k materials have been investigated for high capacitive density and low losses, especially in thin film form. It is impossible here to give a thorough overview on all available literature due to the large number of studies and results. Therefore, the following state-of-the-art is restricted to publications directly related to the topic of this thesis, and is restricted to materials based on binary oxides or their solid solutions.

1.3.1. Binary oxides

Figure 8 shows the probable binary oxides to replace the SiO_2. We can divide all the materials based on their energy band gaps. Materials with a high energy band gap (above 7 eV, group A in Figure 8) seem to meet the above-mentioned requirements, since they allow to obtain high breakdown voltages. Al_2O_3, CaO and MgO have been studied largely as a replacement for SiO_2 [22,23,24]. These materials can be used in the amorphous state and can have good interfaces with Si. Al_2O_3 has a high thermal stability and stays in the amorphous state even at high deposition or annealing temperatures. However, this group of materials show quite low dielectric constants in the range of 6 to 10, which is not high enough for the future reduction of the capacitor size during a reasonable time of scaling [19]. CaO is highly reactive with water and will have reliability issues if used in devices [26].

The materials of group B (Figure 8), including Ta_2O_5, Y_2O_3, HfO_2, ZrO_2, La_2O_5 etc., have an energy bandgap between 4 and 7. These binary oxides have comparatively large dielectric constants (15 - 30). They have been studied extensively in the last decade for the replacement of SiO_2. Despite having a high dielectric constant and a high enough bandgap, some of these binary oxides do not respond to all the requirements. Ta_2O_5 is thermodynamically unstable on Si, and the possibility of forming an interfacial layer of SiO_2 is more likely at the interface [19]. ZrO_2 is known to diffuse oxygen into the Si substrate during the post-annealing process [21]. Through a proper balance of all the requirements, HfO_2 emerged as the best suitable binary oxide for the high k dielectrics. Hafnium dioxide has a high dielectric constant (25) and a relatively large bandgap (5.7 eV), large heat of formation (-271 kcal/mol, more than that of SiO_2: -218 kcal/mol), good thermal and chemical stability on silicon and considerable barrier heights at interfaces with Si. Since 2007, the microelectronics industry is using hafnium-based devices. Although, HfO_2 is

the most promising among all oxides but the interface with Si is still not as good as SiO_2, the formation of the interface SiO_2 rules out its probability for the future high-k material [27].

Group C (Figure 8) materials have a high dielectric constant but a small energy bandgap. TiO_2 is having a dielectric constant of 60 arising from the soft phonon involving Ti ions, but the energy bandgap of 3.2 eV makes it not suitable for the use as a dielectric [27,28].

1.3.2. Ternary oxides

Other than the binary oxides, alloys of different materials are of great interest as alloying allows tuning the materials properties to the desired values. Ternary oxides, as for example $HfSi_xO_y$, $ZrSi_xO_y$, $Hf_xAl_{1-x}O_y$, $Ti_xAl_{1-x}O_y$ and $ZnO\text{-}Al_2O_3$ alloys, have been studied for replacing SiO_2. These compounds are typically the solid solutions of binary oxides, where a material with a high dielectric constant is combined with a material with a high band gap, and show a typical dielectric constant value of about 10 – 50, but the dielectric losses stay a critical issue for their integration in circuits. In case of Al doped ZrO_2 and Al doped HfO_2, the dielectric constant reaches the value of 30 - 35 and the dielectric losses were decreased with increasing the Al concentration in the films [30]. Still, these ternary oxides are not suitable for application because their properties highly depend on composition and even a small variation may degrade the properties.

As the polarizability of Ti ions is high, the addition of Ti could increase the dielectric constant of the material. In case of the $Ti_xAl_{1-x}O_y$, a high capacitive density of around 7.7–8.3 $\mu F/cm^2$ was obtained and 1eV increment in the bandgap was achieved [31]. However, these results are encouraging but still not satisfactory for integrated circuit applications.

1.3.3. Laminates and stacked dielectrics

Similar to the principle of alloying, in order to harness the strengths of two different materials, it is possible to use laminate stacks. In these laminate structures, the properties of the individual materials are conserved and hence improved properties compared to their individual constituents are expected. Robertson proposed that with laminates of a material with high dielectric constant and another material having high energy band gap, the required properties could be achieved [19]. In the last decade, a lot of research has been accomplished on the multilayered form or laminates of various binary oxides. The electrical and dielectric behaviors

of these laminates have been studied extensively. For example, Al_2O_3 with a high energy band gap of 8 eV is integrated with binary oxides with a high dielectric constant (TiO_2, HfO_2, ZrO_2) [31, 32,33,34]. Out of many laminate structures, Al_2O_3/TiO_2 and Al_2O_3/HfO_2 have shown some promising results and will be detailed further in the following.

Al_2O_3 / HfO_2 laminates

HfO_2 on Al_2O_3 laminated dielectrics have been reported by many researchers as a high k dielectric material for gate oxide applications. Hang Hu reported that HfO_2 and Al_2O_3 laminates with individual thickness of 5 nm and 1 nm, respectively, shows a capacitive density of 12.8 $fF/\mu m^2$ with a leakage current at 2 V of $7.45 \cdot 10^{-9}$ A/cm^2 [35]. In another study, a 55 nm thick HfO_2 layer was sandwiched between 2 nm thick top and bottom layer of Al_2O_3, and an increase in the capacitive density was observed. The Al_2O_3 layer between the dielectric and substrate was reducing the direct insertion of charges into the substrate and also reducing the crystallization of the HfO_2 layer, which is then reducing the grain boundary channels for the charge carrier conduction [36]. Park et al observed that the dielectric constant of laminates increased with the reduction of the sublayer thickness, which was attributed to the interfacial layer between Al_2O_3 and HfO_2 [37]. Mahata et al compared a two-layer structure composed of HfO_2/Al_2O_3 (3.5/3.5 nm) on InGaAs substrate with a single HfO_2 film. They observed negligible difference in the dielectric constant, however the leakage current decreased comparatively [38]. A comparative study between the laminates of HfO_2/Al_2O_3 and the ternary compound Hf_xAl_yO on InGaAs substrate was published by Igor et al [39]. They reported that when the sublayer thickness in laminate structures was decreasing, the effective dielectric constant was increasing. However, the maximum dielectric constant attained was 17 for the Hf_xAl_yO laminate. Even though laminates of HfO_2 on Si showed similar properties, Raffaella Lo Nigro et al pointed out that the laminate structure of Al_2O_3/HfO_2 remains amorphous in nature even after annealing at 800°C [32]. Apart from this, other HfO_2 based laminates have been studied and investigated, as for example $HfO_2/LaAlO_3$ [40] (where a dielectric constant of 20 was obtained) or HfO_2/Ta_2O_5 [41]. HfO_2/ZnO laminates have shown the presence of MW effect and the dielectric constant of up to 300 was obtained at low frequencies [42]. However, high dielectric losses limit their applicability.

Al_2O_3 / TiO_2 laminates

Other than the HfO_2 based stacks, Al_2O_3/TiO_2 laminates have been studied extensively and showed promising results. Al_2O_3 (k = 9 and bandgap = 8.6eV) and TiO_2 (k = 60 – 90 in the crystalline state, 20 – 30 in the amorphous phase, bandgap = 3.2eV) are the materials with insulating and semiconducting characters, respectively. The dielectric constant of Al_2O_3/TiO_2 laminates has been reported as 8 in amorphous laminates, 20 in crystalline laminates, and 26 when TiO_2 layer was sandwiched between two Al_2O_3 layers [12,13,14]. It has been pointed out in many studies that the interface between the oxides plays a critical role in defining the optical, mechanical and electrical properties of the laminates [33]. However, the dielectric constants of these laminates are not high enough for future devices.

Revolutionary changes were observed in Al_2O_3/TiO_2 laminates when the thickness of the individual layers is reduced to the sub-nanometric range, motivating more studies on laminates with individual layer thicknesses in the sub-nanometric ranges. Sub-nanometric laminates of Al_2O_3/TiO_2 reported by P.Walke et al. showed a giant dielectric constant up to 10^4 [13]. These amorphous sub-nanometric laminates prepared by Pulsed Laser Deposition can reach such a value when the thickness of the individual layers is in the sub-nanometric range (< 1nm). This huge dielectric constant was explained by the presence of Maxwell Wagner effect (section 1.2.3). Figure 9(a) shows the dielectric constant and dielectric losses as a function of frequency for Al_2O_3/TiO_2 (0.7 / 0.8nm) laminates, obtained by P. Walke et al. W. Li et al showed that when the thickness of the individual layer is reduced from the nanometric range to sub-nanometric range, the dielectric constant increases by a magnitude of three and a value of 10^3 was achieved for ALD (atomic layer deposition) grown amorphous Al_2O_3/TiO_2 (0.2 /0.2 nm) laminates [13]. According to this study, the high dielectric constant is due to the presence of MW relaxation at the interface originated from the presence of oxygen vacancies. At the interface region, the charges of the semiconducting layer originated by oxygen vacancies in the TiO_2 layer are accumulated. These charges move from one interface to the other when an alternating electric field is applied to them. Figure 9(b) shows a schematic representation. However, when the thickness of the individual layer is in the nanometric range, the charges cannot reach the opposite interfaces at

the observed frequencies and show hence no MW relaxation. This could be one explanation behind the presence of the MW effect in sub-nanometric laminates, but not in nanometric ones.

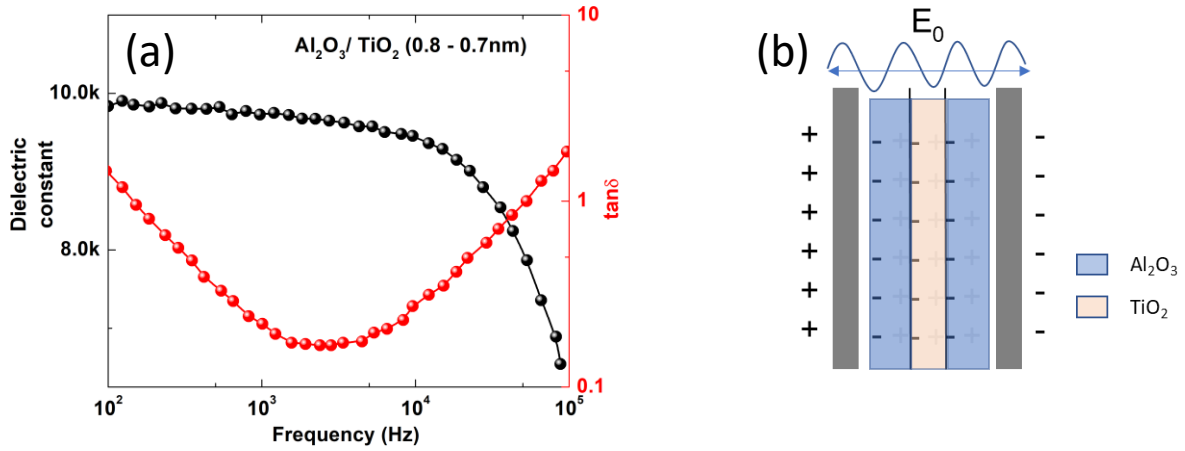

Figure 9 (a) Dielectric constant and dielectric loss of the Al_2O_3 / TiO_2 (0.8 / 0.7nm) laminates observed by P.Walke et al [15], (b) Schematic representation of the MW effect in laminates under the influence of an alternating electric field

G. Lee et al. showed that in sub-nanometric laminates the dielectric properties could be tailored based on the sublayer thickness, even a few Å change in sublayer thickness dramatically increases the relaxation cut-off frequency by more than 3 orders of magnitude with high dielectric constant (k>800)[46]. The properties of ALD grown laminates were further studied by A. Kahouli et al, through the dependence on the electrode material [47], the conduction mechanisms [48], and capacitance – voltage characteristics [49], underlining the critical role of the accumulation of the TiO_2 charges at the internal interfaces. The dielectric losses stay a problem in these laminates, although they can be limited by the choice of electrode or the introduction of a thick Al_2O_3 layer at the laminate/electrode interface [50].

1.4. Objective of the thesis and chosen materials

As discussed in the last section, the sub-nanometric laminates of alternating layers of an insulator and semiconductor can induce a high dielectric permittivity arriving from the interfacial MW relaxation. Al_2O_3/TiO_2 sub-nanometric laminates have shown some promising results except a certain problem of reproducibility. Although in itself consistent, a wide range of available literature show different properties. However, in every study, the role of the interface has been considered as a critical factor, which governs the dielectric properties of the laminate structure.

Charge accumulated at the interface gives rise to the MW relaxation and hence the dielectric constant of the laminates.

In this thesis, we will explore the possibility of enhancing the dielectric constant originating from MW relaxation in laminates of Al_2O_3, Y_2O_3 and ZnO. In order to understand the properties of the interface driven dielectric properties, a detailed study on the single films of Al_2O_3, Y_2O_3 and ZnO is conducted. As the explained for the case of Al_2O_3/TiO_2 laminates, the semiconducting TiO_2 provides the free charges for interface accumulation and then enhance the polarization. We explore the possibility of introducing another semiconducting oxide (ZnO) layer in insulators like Al_2O_3 and Y_2O_3. ZnO is known for its tunable electrical properties [51] including a highly conducting state when doped with charges, hence, it is expected to provide more levers for tuning the dielectric properties of the laminates. More details regarding these materials are explained in the next sections.

1.4.1. Al_2O_3

Aluminum oxide (Al_2O_3) is a high bandgap (8.9 eV) insulator having a dielectric constant of about 9, and large thermal conductivity [52]. A large conduction offset with Si (2.8 eV) makes it a suitable material for integrated circuits. Crystalline and amorphous films of Al_2O_3 have been studied in detail for various application in non-volatile semiconductor memories [52], dynamic random-access memory (DRAM), capacitors [52] etc. Al_2O_3 is known to have a defect free interface with Si and the stability of the Al_2O_3/SiO_2 interface was estimated by thermodynamic approach using bond enthalpies by R.G. Bankras et al [53].

Various techniques have been used for the growth of Al_2O_3 thin films. Chemical vapor deposited films of Al_2O_3 are found to be amorphous and transparent. However, annealing of films at 1100°C results in the crystalline α-Al_2O_3 phase [54]. Sputtered Al_2O_3 thin films were studied by Prasanna et al, showing an amorphous structure until 550°C and a stoichiometric ratio of approximately 1.5, with a dielectric constant of 7.5 [55]. ALD grown Al_2O_3 films were also found to be amorphous and had a very small defect density even in at low thicknesses of 2nm [56].

A good interface with Si, a high band gap to limit the dielectric losses and an amorphous character even at high deposition or annealing temperatures make Al_2O_3 a perfect material to be used in dielectric films. In this thesis, I have grown the amorphous Al_2O_3 thin films by PLD and

studied their dielectric properties to understand the defects in the films. These defects are mainly related to the deposition pressure during the deposition of the films.

1.4.2. Y_2O_3

Y_2O_3 is known for having excellent thermodynamic stability with Si even at high temperature [22], a large bandgap of 5.8eV [57,56] and a high dielectric constant (12 – 17) [58]. These properties of Y_2O_3 make it a strong candidate for future high-k oxides in integrated circuits. Several methods such as ion beam sputtering, thermal decomposition, chemical vapor deposition, electron beam evaporation and pulsed laser deposition (PLD) have been used to prepare crystalline Y_2O_3 thin films [58,59,60]. In these studies, a strong relationship between the deposition parameters, the crystallinity, and the dielectric properties of the thin films has been observed. The amorphous Y_2O_3 thin films have shown smaller leakage current densities as compared to their crystalline counterparts [62] and can have applications in optical communications as optical amplifiers [63], because of the reduced grain boundary scattering losses [64]. A detailed theoretical study on bulk Y_2O_3 by J. X. Zheng et al [65] showed that oxygen vacancies are the dominant defect type in Y_2O_3 when the Fermi level is within the bandgap of Si. The effect of these oxygen vacancies on the electronic structure of Y_2O_3 was also established by F. Jollet et al [66], showing that even the binding character is modified. In amorphous Y_2O_3 films, oxygen defects can create a high quantity of localized charges in the insulating gap, enhancing the conduction and deteriorating the voltage response. Therefore, a study of the properties of amorphous Y_2O_3 films with different oxygen stoichiometry was accomplished in this thesis. Further, a detailed analysis of the stacks of Y_2O_3/Al_2O_3 and Y_2O_3/ZnO have been achieved with an aim of reaching a high dielectric constant due to the MW effect.

1.4.3. ZnO

Zinc oxide (ZnO) is an n-type semiconductor with excellent optoelectronic properties: it has a dielectric constant of 9, a wide band gap (3.36 eV), and a high thermal stability [67]. Because of these properties, ZnO can be used in a wide range of applications including gas sensors and bio sensor applications [68] , surface acoustic wave (SAW) devices [9] and solar cells [68]. ZnO thin films have been prepared and studied by various different deposition techniques such as

pulsed laser deposition [69], sol-gel method, chemical vapor deposition [70] , RF sputtering and atomic layer deposition [70]. The electrical properties of the ZnO are highly dependent on the defect concentration in ZnO films. ZnO is known to have native point defects such as Zn and O vacancies and Zn and O interstitials [71]. The conductivity of ZnO can be varied based on the defect concentration [72]. The dielectric properties of ZnO single films as well as laminates of ZnO have shown promising results [73].

In this dissertation ZnO single films have been studied for their dielectric and structural properties by varying the defect concentration induced by the deposition parameters. The study of ZnO single films was accomplished with the aim of using ZnO as a semiconductor layer in laminate stacks of Al_2O_3/ZnO and Y_2O_3/ZnO.

Chapter 2 Experimental techniques

This chapter focusses on explaining the various experimental details of the main techniques used in the course of this thesis. A detailed introduction of the growth of films and laminates, the fabrication of micro-capacitors from the sample using lithography and the different used characterization techniques are given in the following. The aim of this chapter is to introduce readers with the various techniques and the analysis of the data, which will be useful to understand the results explained in the next chapters. Techniques being used in a less general way will be introduced rapidly in the experimental chapters.

2.1. Deposition of the thin films and laminates

Thin films are considered as an old art used by Egyptians for decorative purposes, and it is the new science still coming up with new applications i.e., microelectronics, optics and storage devices. Thin films of materials have been the research topic among the scientists since the last 30 years. The unique properties which materials show when they are almost 2-dimensional, makes thin films an intriguing approach to modify properties, with the aim to improve them or even generate new ones. There are many methods to grow the thin films, which are categorized in (i) Physical Vapor Deposition (PVD) and (ii) Chemical Vapor Deposition (CVD). In PVD techniques, the target material is evaporated, and the film synthesis takes place on the substrate surface by condensation, without any chemical reaction, while in CVD techniques, organic precursors of the film material are used, with a synthesis of the material itself on the surface of the substrate. Both of these categories contain many methods but, in this thesis, we have used Pulsed Laser Deposition (PLD), a PVD method, for the growth of thin films and laminates.

2.1.1. Pulsed Laser Deposition

Pulsed Laser Deposition (PLD) is a process carried out in a vacuum chamber, as shown in Figure 10. The PLD deposition is considered as a technique adapted to research, because of its capabilities to deposit complex structures, but only on small surface areas. A pulsed laser beam of high energy is focused onto a target of the material to be deposited. A high laser energy density can ablate the material from the target and creates a plasma plume. This forwardly directed

plume generates the material flux and carries the material to the substrate. A sufficient temperature of the substrate help these ad-atoms to condense and construct the thin film structure on the substrate. Good cationic stoichiometry transfer and the possibility to control the deposited volume in a very exact way makes PLD a perfect deposition method for the growth of complex materials and also for laminates with sub-nanometric individual layers. In the following section, the main phases of a PLD process are explained in detail: (i) interaction of laser pulses with the target material, (ii) plume formation and expansion, and (iii) film condensation and growth mechanism.

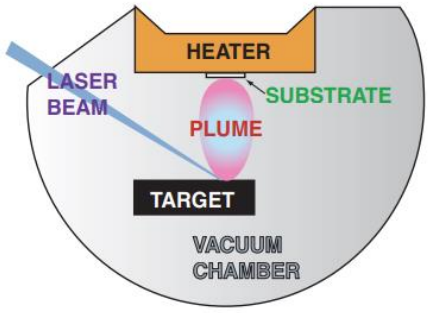

Figure 10 Schematics of a Pulsed Laser Deposition chamber

(i) Target – laser interaction

In order to remove an atom from a solid surface by a laser pulse, the energy provided to a single atom should exceed the binding energy of that atom. The energy absorbed in the target material per unit surface area depends on the laser fluence, which is a function of the laser intensity and the laser pulse duration. Based on the laser pulse duration, the interaction of laser pulses with matter can be divided into three different regimes: the femtosecond regime, the picosecond regime, and the nanosecond regime.

In the femtosecond regime, due to the very short timescale, the absorbed electromagnetic energy of a laser pulse is immediately converted to different electronic excitations such as plasmons, excitons, electron–hole pairs (in semiconductors), and unbound electrons (in metals). But the small-time scale of the pulses and the laser interaction do not allow to couple electronic

energy to the crystal lattice and no damage to the target surface takes place, rather heat energy transfer takes place within the material.

In the picosecond regime, the sufficient time for the laser interaction with matter helps the excited electrons to transfer their energy to the lattice. Hence, the emission of the particles depends on the conduction and diffusion of the absorbed energy with the material. The transfer of energy from excited electrons to the lattice starts the heating of material within the optical absorption depth of the material $\frac{1}{\alpha}$, where α is the material-dependent optical absorption coefficient. If the absorption depth of the material is larger than the thermal diffusion length, the target surface will be heated to the thickness of $\frac{1}{\alpha}$ independently on the pulse duration. In most of the ceramics, the absorption depth is larger than the diffusion length and we can remove significant amounts of material from their surface in the picosecond regime.

In nanosecond regime, the longer time of the laser pulse creates a larger molten layer of material on the surface. The boiling and melting of the material under the vacuum leads to the evaporation of macroscopic particles of the material from the surface. This evaporation of particles from the surface is termed as ablation. Figure 11 illustrates the ablation of particles from the surface schematically.

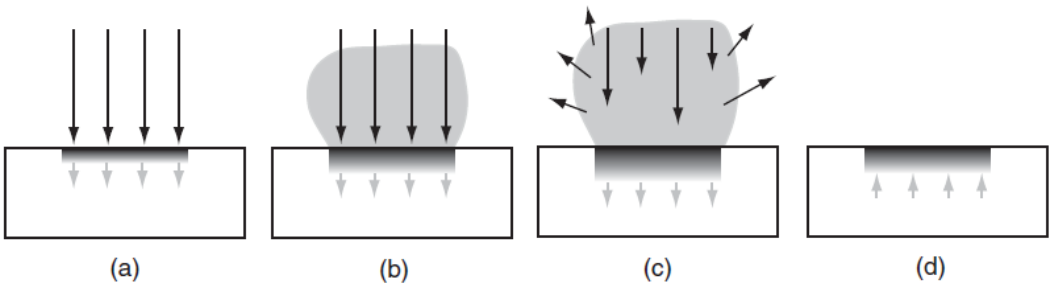

Figure 11 Schematic illustration of the ablation process in the case of nanosecond PLD. (a) Initial absorption of laser radiation (black arrows) and melting of the target material (grey arrows indicate the motion of the solid–liquid interface). (b) The melt front propagates into the solid and the evaporation of particles begins. (c) The plume absorbs the rest of the laser radiation and a fully ionized plasma is formed. (d) The melt front starts to recede after the laser pulse and the target is re-solidified.

In order to ablate any material, the laser fluence has to be higher than its ablation threshold value. We can change the laser fluence by either changing the laser energy or the spot size of the laser on the target. In this project, we deposited single films and laminates of Al_2O_3, Y_2O_3 and

ZnO. The threshold fluence of these materials have been determined by various studies [74]. We have used a KrF excimer laser with 248 nm wavelength with a pulse duration of around 20 ns and an energy of 200 mJ. With the spot size of the laser on the target of about 1 x 3 mm^2, a laser fluence of about 2 J/cm^2 is reached. This fluence is higher than the threshold value for these materials. The laser energy was optimized in preliminary studies during the growth of the single films of the different materials, and the laser energy of 200 mJ was found to give satisfying results for all materials.

(ii) Plume formation

After the ablation, the ejected material from the target is partially ionized and creates a particle cloud near the surface of the target. This particle cloud absorbs more energy from the incoming laser pulse, ionizes further and develops a fully ionized plasma. These particles, which have an anisotropic velocity distribution away from the target surface, start colliding with each other, leading to an isotropic velocity distribution at nearly 50µm from the surface of the target. This point is known as Knudsen layer. After the Knudsen layer, the plasma plume forms and starts to expand in the direction of the target normal at supersonic velocities. The generated plume consists of electrons, ions, particle clusters, macroscopic particulates and neutral atoms. The continuous recombination and fluorescence generate light and colour in the plume. Figure 12 shows the plume generated by the KrF laser with an energy of 200 mJ from the surface of a Y_2O_3 target under 0.005 mbar oxygen pressure.

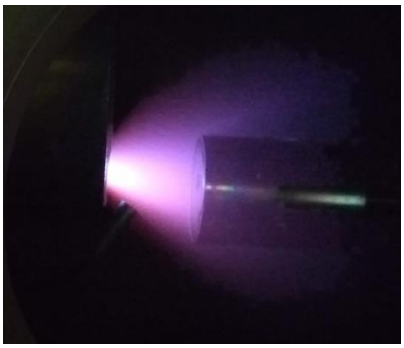

Figure 12 Plume generated form the Y_2O_3 target with an incident laser beam of 200mJ under 0.005mbar oxygen pressure. On the right, the sample heater with the substrate can be seen.

The expansion of the plume depends on the kinetic energy distribution of the different species (electrons, ions, neutral atoms etc.) present in the plume, which is controlled by the interactions between these different particles, for example the coulomb interactions between ions and electrons controls their kinetic energies, and the background pressure in the vacuum chamber. The presence of the ambient gases during the deposition can scatter, attenuate, and thermalize the plume. The pressure of the background gas compresses the plume by creating a shock front and can reduce the kinetic energies of plume constituents.

As we deposit binary oxides and their laminates in this thesis, we use O_2 as the ambient gas. The effect of the background ambient pressure on the growth and properties of single films and laminates of Al_2O_3, Y_2O_3 and ZnO have been studied extensively and will be explained in the results section of this dissertation (chapter 3).

(iii) Film condensation and growth mechanisms

As the plume propagates and reaches the substrate surface, the particles start to adhere on the substrate surface. The growth of the film on the substrate surface can be described by the following subsequent mechanisms: the adsorption and condensation of isolated atomic clusters, the nucleation and coalescence of nuclei, and the development of the film structure.

Adsorption and condensation of isolated atomic clusters

The directed plume towards the substrate allows the impingement of the atomic clusters on the substrate surface. Generally, these atoms have higher energy than the substrate temperature. On the substrate surface, the atoms can adsorb and stick permanently, can adsorb and re-evaporate or can just bounce off. The nature of the atomic adsorption depends on the equilibrium between the vapor and solid phases of these atoms. If the vapor pressure of the incoming atoms is higher than the equilibrium pressure, the atoms starts to adsorb on the surface of the substrate and condensation becomes energetically favorable.

Nucleation and growth

Figure 13 illustrates the different processes involved in the nucleation of clusters on a surface by vapor deposition of atoms. The incoming atoms arrive on bare substrates areas or on pre-

existing clusters. These ad-atoms can subsequently diffuse over the substrate or cluster surface. There are many possibilities how these atoms can react, as summarized in Figure 13.

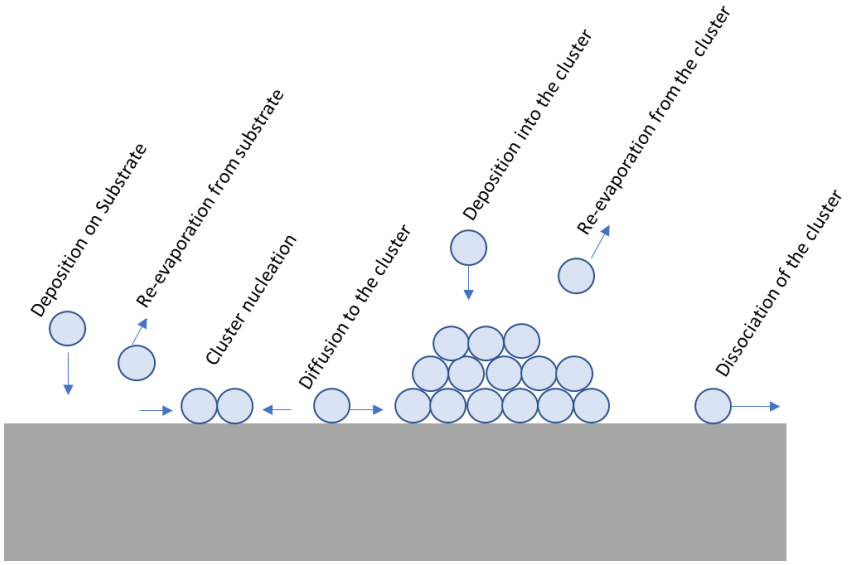

Figure 13 Schematic representation of the different processes involved when the vapor atoms reach the substrate surface

The growth of the thin film can be further divided in to three different modes based on the arrangement of the atoms on the substrate surface: (a) Three-dimensional island growth − the Volmer-Weber growth, (b) Two-dimensional full-monolayer growth − the Frank-van der Merwe growth, and (c) Two-dimensional growth of full monolayers followed by nucleation and growth of three-dimensional islands − the Stranski - Krastanov growth. Thermodynamics of the substrate and film surface energies defines the possible growth of the film. All different growth modes have been illustrated in the schematic shown in Figure 14.

(a) Three-dimensional island growth − the Volmer-Weber growth:

A three dimensional growth takes place when the incoming atom prefers to settle on a pre-existing cluster rather than on the substrate surface. The formation of a stable cluster can also be described in terms of surface energies. If the sum of the surface energies in the cluster–vapor and substrate–cluster interfaces is larger than the corresponding surface energy for the substrate–vapor interface, the film will grow three-dimensionally.

(b) Two dimensional growth - the Frank-van der Merwe growth

In this growth mode, the nucleation of the island takes place with a thickness of only one monolayer. These islands form a complete monolayer before the nucleation of a new monolayer takes place. Again, we can explain this in terms of surface energy: If the sum of the surface energies in the cluster–vapor and substrate–cluster interfaces is nearly equal to the corresponding surface energy for the substrate–vapor interface, the incoming atoms grow layer by layer on the substrate surface.

(c) Two-dimensional growth of full monolayers followed by nucleation and growth of three-dimensional islands − the Stranski - Krastanov growth

In this growth mode, after the formation of a few monolayers, islands starts to grow. When the surface energy for the substrate – vapor interface is higher than the sum of the surface energies in the cluster–vapor and substrate–cluster interfaces, a mixed growth of islands and the monolayer observed.

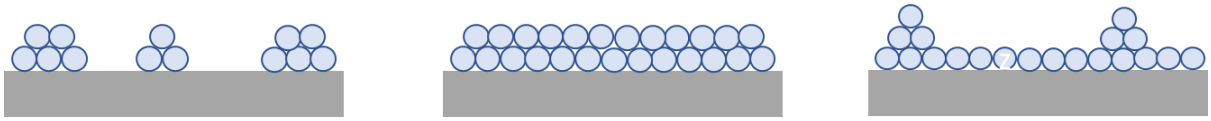

Figure 14 Schematic representation of the different growth modes of vapor atoms on the substrate surface

2.1.2. Growth of single films and laminates of Al_2O_3, Y_2O_3 and ZnO

From the above discussion regarding the pulsed laser deposition, it is clear that various parameters during the growth can affect the quality of the thin film and ultimately their properties. Therefore, we have tested for the growth of single films and laminates different parameters: temperature, pressure, laser energy and different substrate - target distances. The effect of temperature and pressure being the most important on the dielectric properties of the samples will be explained in the result chapters extensively. The laser energy and the substrate-target distance having a smaller influence, these parameters were fixed in preliminary tests, without the discussion of results here.

For all the depositions in this thesis, a commercial PLD vacuum chamber Meca 2000 coupled with an excimer KrF laser source by Coherent (wavelength 248 nm) was used. The vacuum

chamber is connected with a turbo molecular pump and a base pressure of 10^{-8} mbar could be achieved in the chamber. This chamber is also equipped with a flowmeter for gas (O_2), and the pressure of the background gas in the chamber can be controlled with the flow rate and the pump valve opening.

Dense targets of binary oxides were prepared by classical solid-state techniques and X-ray diffraction (XRD) analysis was conducted to confirm their purity. Before starting the deposition, a pre-ablation of the target surface is carried out with 250 pulses (5 Hz), in order to remove any surface contamination from the surface. For the deposition, we have used Si (001) substrates, which were sonicated in acetone for 5 minutes followed by ethanol for 5 minutes. The same cleaning method was used for all the samples prepared in this thesis to avoid any effect from different cleaning methods. However, preliminary tests on the substrate preparation showed no effect on the resulting properties, including HF-cleaning to remove the native oxide layer. The substrate temperature is maintained by the heater connected to the substrate holder with a maximum temperature limit of 1000°C. The sample is glued with silver paste on the heater.

For the deposition of the single films, the required target is irradiated with the required number of pulses. For the growth of the laminate structures, two different targets are used. Based on the required individual layer thickness in the laminate structure, the corresponding targets are irradiated alternatively. A laminate deposition program written in lab view allows to control the rotation of the target and the number of pulses on each one, as well as the total number of bilayers to be deposited. For the growth of the sub-nanometric laminates, the calibration of the growth rates is conducted using X-ray reflectivity curves of the calibration samples.

In the following list, the common steps taken for the deposition of all samples in this thesis are listed:

(i) Ultrasonic cleaning of the Si(001) substrates in acetone and ethanol for 5 minutes each

(ii) After loading the substrate, the vacuum pumps are switched on for about 2 hours until a base pressure of at least 1 x 10^{-6} mbar is reached

(iii) Heating of the substrate: A substrate temperature from 25°C to 300°C was used for different depositions with a heating rate of 20°C /min

(iv) Establishing the required O_2 pressure in the deposition chamber: The O_2 gas is let into the chamber by using a flowmeter. The pressure is controlled by the partial closing of the pump valve. Pressures ranging from vacuum (base pressure, no O_2 inlet) to 0.1 mbar.

(v) Parallel to the step (iii) and (iv), the laser is heated for about 10 minutes in order to reach a stable output energy. Afterwards, the laser energy is calibrated. For all depositions, the laser energy is fixed to 200 mJ.

(vi) Pre-ablation of the target with 250 pulses, 5 Hz. The surface of the substrate is protected from any deposition by a shutter.

(vii) Deposition of the film with the required number of pulses. The substrate – target distance is fixed to 80 mm. For the deposition of the laminates, two different targets are used with the required number of pulses on each. For laminates, the material mentioned first in the designation was also used as a first layer. For example, in an Al_2O_3/ZnO laminate, Al_2O_3 was the first material to be deposited. The top layer of the laminate is the material mentioned in the second place. Tests with symmetric laminates, i.e. where a top layer of the first material was added after the growth of all bilayers, did not show significant changes of the observed properties.

(viii) After deposition, the films were cooled down to around 40 °C with a rate of 10 °C/min in the same oxygen pressure as used during the growth.

2.2. Fabrication of the micro-capacitors

In order to study the dielectric properties of the deposited films, parallel plate micro-capacitor structures were fabricated with the doped Si substrate as the bottom electrode and silver layer as the top electrode, sandwiching the deposited film. The size of these square micro-capacitors was maintained as 250 x 250µm. Tests with different top electrode sizes and shapes were carried out and showed that the used shape and dimension lead to reliable results. Microfabrication of these capacitors was carried out using the photolithography technique followed by the deposition of silver.

The photolithography process is defined by the creation of patterns within a layer of photoresist that covers the thin film. These patterns can then be transferred into the film by etching or into a subsequently grown film by the lift-off method. The ability of this process to transfer the geometrical patterns in micrometric scales on the sample helped the evolution in the CMOS technologies. Photolithography was conducted in the CRISMAT clean room to avoid any contamination on the sample surface, which would affect quality of the fabricated structures and the reliability of the process. Following are the steps used for patterning the microstructures on thin films:

(i) Deposition of Resist

A resist is the photosensitive compound, which can change their molecular structure when exposed to the UV radiation. The photoresist S1805 was used for the lithography of the samples in this thesis. The photoresist is deposited on the sample surface using the spin coater with a rotation speed of 5000 rpm for 30 seconds, leading to a resist thickness of about 500 nm. After the deposition, the sample is heated at 100°C for 1 minute to evaporate the resist solvent.

(ii) Mask alignment and UV exposure

The resist on the sample is exposed to a broadband UV light through a flexible photo – mask. The shaded areas of the mask protect the resist from the exposure in between the electrode squares. The resist is exposed at 150 mW/cm. For convenience, the mask was aligned with the sample edge. The mask aligner is a MJB4 (SÜSS Microtec) equipped with a mid-UV filter, allowing the exposition of the resist of geometries with a minimum lateral size of down to 700nm.

(iii) Resist development

The resist was developed with an adapted developer for 15 seconds, followed by washing in distilled water. The developer removes the exposed resist, leaving a resist grid on the sample with holes of 250 X 250μm^2. The schematic in Figure 15 shows all the steps taken in the development of the desired geometry on the sample surface.

(iv) Deposition of the electrodes and lift-off step

The Ag top electrode is deposited on the sample by thermal evaporation with a typical thickness of about 200 nm. After deposition, the sample is washed in acetone. The acetone dissolves the

resist, together with the silver layer on its top. The remaining parts of the Ag film form 250 X 250 μm^2 squares on the sample, with a spacing of 100 µm, as shown in Figure 15.

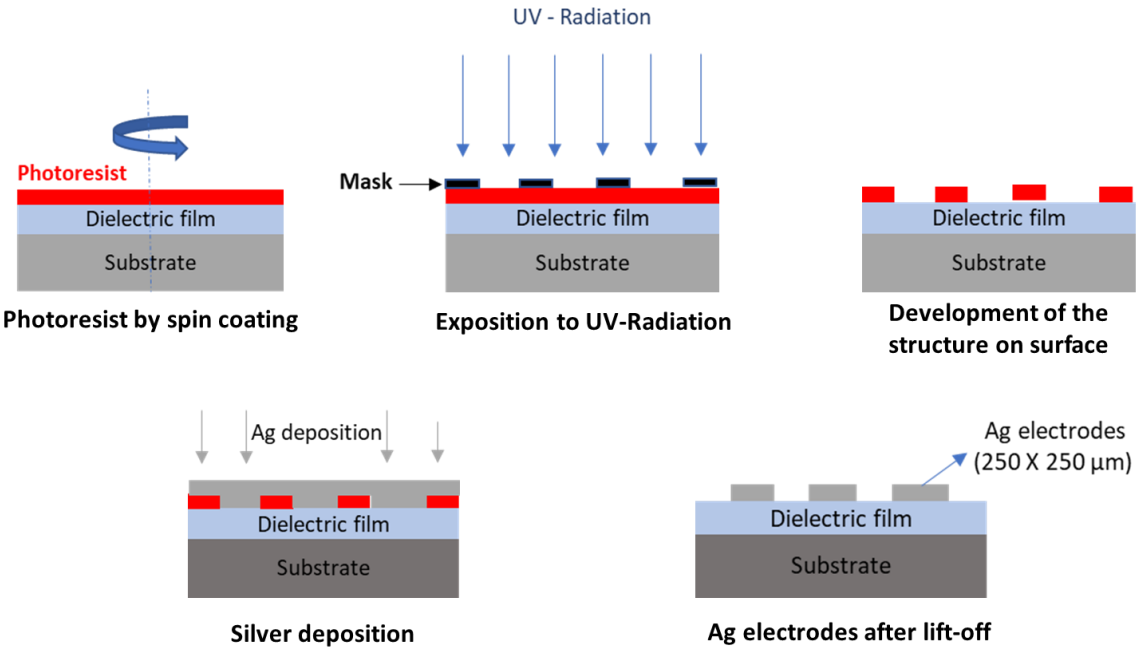

Figure 15 Schematic representation of the photolithography process

2.3. Structural Characterization

X-rays have a wavelength of the order of the atomic distances in condensed matter, and their non-destructive nature makes them a preferable tool for the analysis of atomic structures. X-ray diffraction and reflection from a sample surface have been studied extensively in the last century and it is a widely used and well-established technique for the structural analysis of thin films.

Like any electromagnetic radiation, the interaction of the X-rays with the matter are of two types: inelastic (Compton scattering) or elastic (Thomson Scattering). In Thomson scattering, the wavelength of the X-rays is conserved, and its scattered component gives details regarding the structure of the material. For the analysis of thin films, a small angle of incidence on the surface provides X-rays with a longer path in the thin film and the diffracted beam contains the information primarily from this part of the sample. Apart from the scattering, X-rays can also reflect from the surface and internal interfaces of the sample and can give details regarding the

thickness, roughness and the density of the thin film. Figure 16 shows the schematic representation of measurement set-up. The X-rays are incident on the sample at an incidence angle ω, the scattered rays form interference patterns and are collected on the detector at a function of angle 2Θ. For our samples, we have used X-ray reflectivity to calculate the thickness, roughness and the density of the film. High-angle X-Ray Diffraction was also used to confirm the amorphous nature of the films (and the purity of the targets). Anyway, as X-Ray Diffraction is not a fundamentally used technique in this thesis, I will refrain here from an introduction of the technique in order to keep the focus of this thesis on the important techniques.

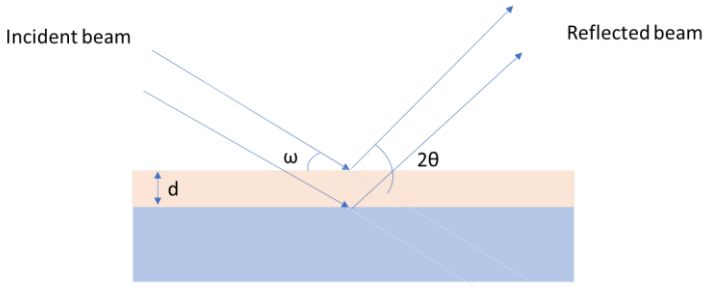

Figure 16 Schematic representation of the set-up used for the X-ray measurements

2.3.1. Principles of X-ray Reflectivity (XRR)

The schematics shown in Figure 17 show an XRR measurement performed on a single film. The X-ray reflectivity technique works on the reflection and refraction of the radiation, similar to the optical reflection and refraction. When the X-ray beam grazes the sample surface at low incident angle ω, the beam is reflected from the surface and the interface between the substrate and the thin film at an angle of 2θ, and generates interference fringes. These fringes contain details regarding the sample thickness, roughness and the density of the film. Due to the low angles of incidence, the penetration depth of the X-rays is low and the main information is obtained on the surface of the sample, i.e. in the thin film area. When the incidence angle is less than the critical angle, total external reflection occurs. Refraction is observed above the critical angle, when the X-ray beam penetrates the sample and passes from air to the thin film. Similar to optical refraction, the refractive index of the material defines the path of the X-rays in the

material and we can apply the Snell's law to get a relation between the incidence and outgoing angle of the x-rays with the refractive index of the material as

$$\frac{cos\,\omega}{cos\,\theta} = \frac{n_1}{n_0} \qquad (14)$$

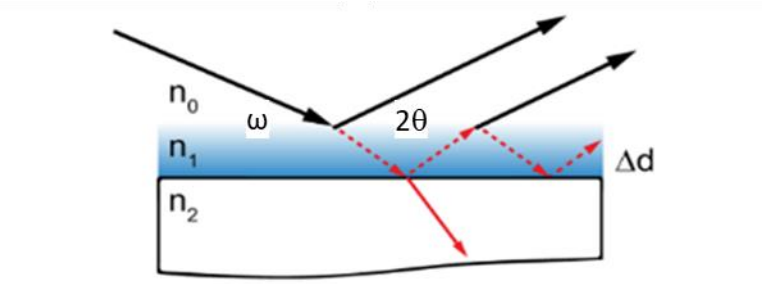

Figure 17 Refraction and reflection of X-rays from a thin film having refractive index (n_1). n_0 and n_2 represent the refractive indexes of air and substrate, respectively, and ω and 2θ are the incidence and outgoing angle of X-rays

The refractive index *n* of the X-ray in any medium is slightly less than unity. The deviation of complex refractive index of X-rays from unity is due to the dispersion and absorption by the media, expressed by the following equation:

$$n = 1 - \delta - i\beta \qquad (15)$$

where δ represents the dispersive part and β represents the absorption by the media.

In case to total internal reflection, the absorption by the media can be neglected and the refractive index can be written as $n = 1 - \delta$. Further using the Snell's law, we can relate the critical angle and the δ as $\theta_c = \sqrt{2\delta}$.

δ and β depend on the electron density ρ_e and the attenuation factor μ, with the following expressions:

$$\delta = \frac{r_e\,\lambda^2}{2\pi}\rho_e \qquad (16)$$

$$\beta = \frac{\lambda}{4\pi}\mu \qquad (17)$$

where λ is the X-ray wavelength (1.5408 Å for Cu $K_{\alpha 1}$), r_e the classical electron radius, ρ_e the electron density and μ is the attenuation coefficient.

When the X-ray beam impinges on the sample at small incidence angle, the obtained specular intensity at an angle 2θ is a function of δ and β. Using the Fresnel's coefficients [75], we can express the ratio between the intensity of reflected beam I_R and incident beam I_0 as follows:

$$\frac{I_R}{I_0} = \left| \frac{\theta - \sqrt{\theta^2 - \theta_C - 2i\beta}}{\theta + \sqrt{\theta^2 - \theta_C - 2i\beta}} \right| \quad (18)$$

Figure 18 shows the obtained intensity of X-rays as a function of the outgoing angle for a single film of Al_2O_3. We can get various details about the thickness of the film (from the fringe width), about the roughness of the film and the interface roughness from slope of the curve and about the density and the chemical composition of the film from the critical angle, as detailed below.

Thickness determination

In XRR measurements, fringes form due to the constructive interference of the X-ray beam, when the path difference between the reflected beam from the surface and the refracted beam from an internal interface (i.e. the substrate/film interface or interfaces between different layers) is equal to the integral multiple of the X-ray wavelength (Figure 17). Therefore, the path difference Δl depends on the thickness of the film:

$$\Delta l = 2\, d\sqrt{n^2 - cos^2\,\theta} \quad (19)$$

where d is the thickness of the film and n is the refractive index of the film. By rearranging this equation and considering the condition for constructive interference ($\Delta l = N\lambda$, with N being an integer), we can obtain the following equation:

$$sin^2\,\theta_M = \frac{\lambda^2}{4d^2} N^2 - \delta^2 - 2\delta \quad (20)$$

with θ_M being the angle of the maxima of the different fringes. Hence by plotting the $sin^2\,\theta_M$ for the fringes against the order number (N = 1, 2, 3, 4…), we will get a straight line and the slope of the line gives the thickness of the film.

In this thesis, we have used a Bruker D8 diffractometer for the XRR analysis, equipped with a monochromator to single out the Cu $K_{\alpha 1}$ wavelength. Before collecting the data, a thorough

alignment of the sample height and the incident angle ω was performed to obtain reliable data. A θ - 2θ scan was performed in the range of 0 - 6° and the intensity profile was collected on the detector as a function of the angle 2θ. The angle θ_m at the maximum intensity of every fringe is extracted and the $\sin^2\theta_m$ is calculated as in equation (20). As the order number of the fringe (N) is not well defined, $\sin^2\theta_m$ was plotted for different values of N varying from 1 to 5. A linear fit is obtained for all the data as shown in Figure 18. The best linear fit is defining the correct value of the N and hence the slope b of this fit is used to determine the thickness of the film as:

$$d = \frac{\lambda}{2\sqrt{b}} \qquad (21)$$

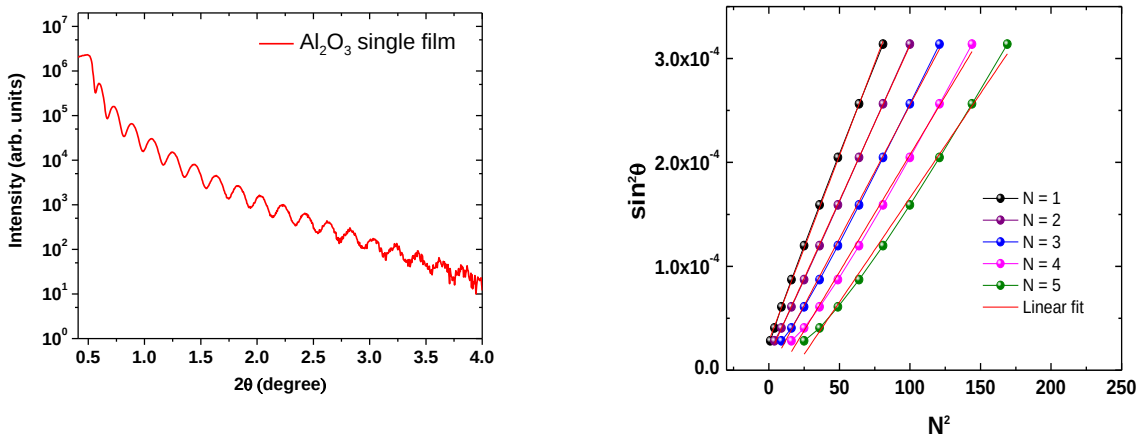

Figure 18 (a) XRR measurement of Al_2O_3 thin film, and (b) $\sin^2\theta$ as a function of N^2 (considering N = 1,2,3,4 and 5) and the linear fits. In the shown example, N = 2 is chosen as the correct linear dependence.

Determination of density and the chemical composition

The measurement of the critical angle of the X-rays contains the details regarding the electronic density and the chemical composition of the films. As explained in the previous section the critical angle is related to the dispersive part (δ) as:

$$\theta_c = \sqrt{2\delta} \qquad (22)$$

δ itself is related to the electron density of the material, so by fitting the XRR curve, we can determine δ and hence the value of the electron density. For the materials with known

stoichiometry, the mass density can be related to the electronic density using the following formula:

$$\rho_e = N\rho_m \frac{\Sigma_i x_i (z_i + f_i')}{\Sigma_i x_i M_i} \qquad (23)$$

Where ρ_e is the electron density, *N* the Avogadro number, f_i' the real part of the atomic form factor, M_i the molar mass of element i and Z_i its atomic number, and ρ_m the mass density. However, for materials with unknown stoichiometry, the value of mass density cannot be extracted explicitly [76].

By fitting the data using the GenX software [77], we were able to fit the complex scattering length, which is the sum of the product of the number of atoms with their atomic form factor (f) for all the elements present. For example, the complex scattering length of Al_xO_y is $((\mathrm{x} \cdot \mathrm{f}'_{\mathrm{Al}} + \mathrm{y} \cdot \mathrm{f}'_0) - \mathrm{i}(\mathrm{x} \cdot \mathrm{f}''_{\mathrm{Al}} + \mathrm{y}\mathrm{f}''_0))$, where $\mathrm{f}'_{\mathrm{Al}}$ and f'_{o} are the real part and $\mathrm{f}''_{\mathrm{Al}}$ and $\mathrm{f}''_{\mathrm{O}}$ the imaginary part of the atomic form factor for Al and O. The values of the atomic form factors can be obtained from the Henke table [78]. Hence by fitting the scattering length, we can get the values of x and y, i.e. the chemical composition [79].

As we are fitting the electron density to find the values of mass density and also for stoichiometry, we cannot get the value of one explicitly without knowing the other. In case of crystalline films, by considering the ideal stoichiometry, we can fit the values of the density, but in case of amorphous films, the stoichiometry can differ from ideal and the determination of density becomes unclear. In this thesis, we will interpret the critical angle in terms of density and stoichiometry, where a reliable analysis is possible.

Roughness of the film

The roughness of the film surface and the substrate/film interface reduces the Fresnel's intensity in specular direction, influencing the slope of the XRR curve. A steep slope indicates a high value of the roughness and small slope corresponds to a small value of the roughness. For example, Figure 37 in Chapter 3 shows the difference in XRR of Y_2O_3 single films curves because of the roughness of the surface. In this thesis, we obtained the values of the roughness by fitting with the GenX software.

2.3.2. XRR analysis of laminate structures

As explained in the previous section, the XRR technique is a useful tool to understand single films. In this section, a detailed explanation of the laminate structure XRR analysis is presented. XRR was used to determine the total thickness of the laminates and also to calibrate the exact individual layer thicknesses.

In the laminate structures, the periodic arrangement of the two different materials with their different electron densities gives rise to the formation of an interference pattern. Hence, the fringes in the XRR curves arise from the total thickness of the laminate structure, as well as the bilayer thickness. In principle, even the individual layers may generate fringes, but in the present case of sub-nanometric or nanometric individual layers, the fringe periodicity is too high as to observe the related fringes experimentally. Figure 19 shows a typical laminate XRR curve of an Al_2O_3/ZnO laminate having an individual layer thickness of 1 nm for both materials and a total thickness of 30 nm. An artificial periodicity arises from the stacked bilayers and a Bragg peak can be observed at $2\theta = 4.2°$. If we use the Bragg law [80] for this peak and calculate the spacing (bilayer thickness), it gives the value of the bilayer thickness i.e. 2nm. Hence, XRR can be used to differentiate between a laminate with a layered structure and a solid solution of the two materials due to strong interdiffusion, leading to a single film behavior.

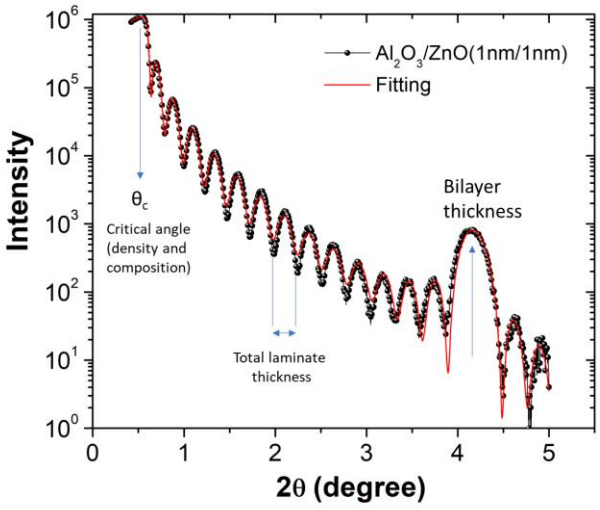

Figure 19 XRR measurements on Al_2O_3/ZnO (1nm/1nm) laminate sample

The total thickness of the laminate is directly proportional to the inverse of the period of the short oscillations present in the XRR curve. The smaller the oscillation period, the thicker is the laminate. Here in Figure 19, the total thickness of the laminate is found to be 29 nm, both by the N^2 method explained in the previous section and also by fitting the data using GenX.

For sub-nanometric laminates, the deposition rate of each material is the most critical parameter to control because the individual layer thickness can be affected even by a single laser pulse, having a strong impact on the dielectric properties of the laminate structure. Hence, to reach the necessary reliability, the calibration of the growth rate is performed before the deposition of each series of the laminate samples. Here, the method will be described with the example of Al_2O_3/ZnO laminates, but the same method was also used for the other laminates.

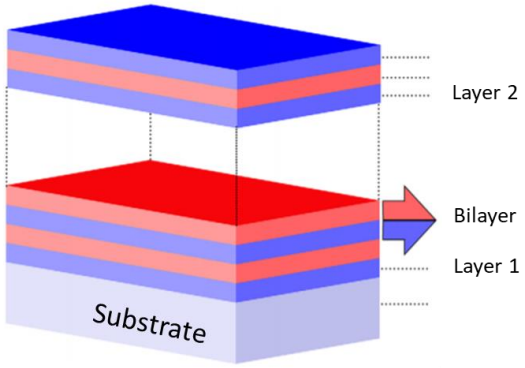

Figure 20 Laminate structure of 2 materials where the bilayer thickness is the sum of individual layer thickness of layer 1 and layer 2

Figure 20 shows the laminate structure with the two different materials, where the thickness of the bilayer is the sum of the thicknesses of one individual layer of each material. If we multiply the bilayer thickness with the total number of repetitions of the bilayer, we can get the total thickness of the laminate structure. The bilayer thickness b can also be expressed as a function of the growth rates of the individual materials and the number of pulses used for the deposition as:

$$b = Ax + By$$

where A and B are the number of pulses on each target, x and y are their deposition rates (nm/pulse) respectively.

For the calibration, three different laminate samples were prepared under the same deposition parameters, but using different numbers of laser pulses on the Al_2O_3 and ZnO target, i.e. Al_2O_3/ ZnO (1000/1000) x 4, (1000/100) x 10 and (100/1000) x 6. Here, the notation Al_2O_3/ ZnO (1000/1000) x 4 represents a laminate structure with 1000 pulses on Al_2O_3, 1000 pulses on ZnO and this bilayer being repeated 4 times. The number of repetitions were adapted in order to obtain similar total thicknesses.

Figure 21 shows the XRR measurements performed on all three calibration samples. From these measurements, the bilayer thickness (b) can be obtained experimentally by extracting the total thickness of the laminate, divided by the number of repetitions. On the other hand, for each calibration sample we can express the bilayer thickness as a linear equation, x and y being the deposition rates of Al_2O_3 and ZnO, respectively:

$$y = \frac{b}{B} - \frac{A}{B}x$$

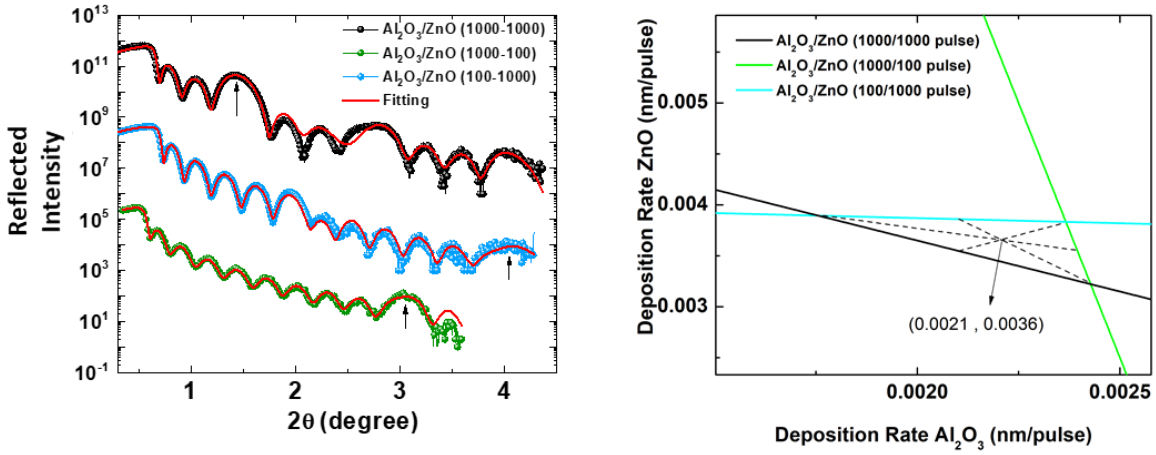

Figure 21 XRR reflectivity curves for calibration samples, the black arrow indicates the position of the Bragg peak related to the bilayer periodicity in each sample

With this equation, we can represent the deposition rate of ZnO (y) as a function of deposition rate of Al_2O_3 (x). The graphical representation of this equation for each calibration laminate is represented in Figure 21, where the intersection point of two laminates represents the mutual solution of the equation, and therefore a possible value of the growth rates. In a perfect system, two laminates are enough for the calculation of the growth rates, but considering possible errors

and uncertainties, it is better to use three calibration samples. Their three lines form a triangle and the centroid of this triangle gives the growth rates of the Al_2O_3 and ZnO. For further confirmation, the XRR data was also fitted with the GenX software and the individual layer thicknesses were calculated, and results of both analyses were compared.

2.4. Impedance spectroscopy

Impedance spectroscopy is a powerful method of characterizing many of the electrical properties of materials and their interfaces with electronically conducting electrodes. We can investigate the dynamics of charges in the bulk or interfacial regions of any kind of material: ionic conductors, electronic semiconductors, mixed electronic–ionic conductors and insulators (dielectrics). In this thesis, we have used this technique extensively for the understanding of the electrical properties of dielectric thin films and laminates. As explained in section 1.2, when an external field is applied on a dielectric material, an intrinsic electric field generates within the material to oppose the external field, which changes the polarization dynamics of the material. As no insulator is perfect and they show a conduction component also, their charge resistance is defined as their complex impedance (Z*)

$$Z^* = \frac{R}{1 + i\omega RC} \qquad (24)$$

where R is the resistance (represents the charge dissipation through the dielectric) of the material and C is the capacitance (represents the charge storing component of the material), and i is equal to $\sqrt{-1}$.

Impedance spectroscopy is the technique, which measures the impedance of a material as a function of the frequency with an applied ac voltage. In heterogeneous dielectrics, where two different types of materials are in contact with each other and form interfaces, impedance spectroscopy is a useful tool to understand the charge transfer processes, resistivity and capacitance of the individual and interface layers, and also the diffusion and possible chemical reactions at the interface.

2.4.1. Principles of Impedance spectroscopy

When a monochromatic voltage, $v_t = v_0 \, sin(\omega t)$ is applied on a capacitor, a resulting time variant current $I_t = I_0 \, sin(\omega t + \theta)$ flows through it, where θ is the phase difference between applied voltage and the resulting current. The voltage and current relation can be established similar to Ohm's law for dc current, and the ratio of the voltage and current represents the complex impedance Z* of the capacitor cell:

$$Z^*(\omega) = \frac{v_0 \, sin(\omega t)}{I_0 \, sin(\omega t + \theta)}$$

This impedance is the hindrance of the charge carrier movements and hence we can determine many intrinsic properties of the materials i.e. ac conductivity, dielectric constant, also band structure elements and non-stoichiometry, as detailed below.

Complex plane representation of impedance

The complex impedance can be expressed as the vector sum of the real and imaginary components and may be plotted in the plane with either rectangular or polar coordinates as shown in Figure 22:

$$Z^* = Z'(\omega) + i \, Z''(\omega) = \frac{v_0 \, sin(\omega t)}{I_0 \, sin(\omega t + \theta)}$$

where Z' is the real part and the Z'' is the imaginary component. Using the Euler's relation, the above equation can be expressed as

$$Z^* = \frac{v_0 e^{i\omega t}}{I_0 e^{(i\omega t - i\theta)}} = Z_0(cos\,\theta + i \, sin\,\theta)$$

So, the real and imaginary components can be expressed as:

$$Z' = Z_0 \, cos\,\theta \text{ and } Z'' = Z_0 \, sin\,\theta$$

From Figure 22, the phase difference can be calculated as

$$\theta = tan^{-1}\left(\frac{Z''}{Z'}\right)$$

From the above relation, the applied time-variant voltage and the obtained current can be converted into a time-independent impedance. The representation of the experimental data in the complex plane helps in understanding the intrinsic properties of the materials.

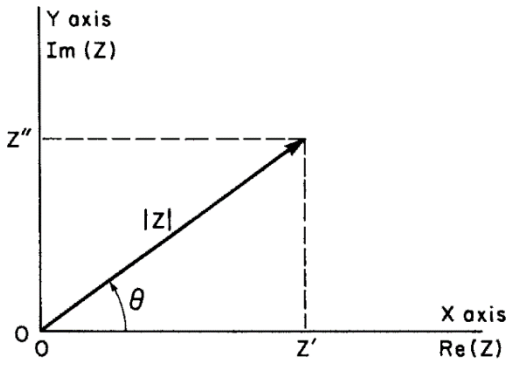

Figure 22 The complex impedance plotted as a planar vector using rectangular and polar coordinates

Basic quantities and their interpretation

The basic quantities, which are interrelated to the complex impedance, are called the immittances: admittance (Y*), modulus (M*) and the dielectric permittivity (ε*). All these quantities can be expressed in the complex plane as:

$$Y^* = Y'(\omega) + i\,Y''(\omega)$$

$$M^* = M'(\omega) + i\,M''(\omega)$$

$$\varepsilon^* = \varepsilon'(\omega) - i\,\varepsilon''(\omega)$$

where the quantities marked by a prime and a double prime are the real and imaginary components, respectively. All these quantities are interrelated, the admittance of the circuit is a complex form of its conductance and is equal to the reciprocal of its complex impedance as:

$$Y^* = (Z^*)^{-1}$$

The modulus function is related to the complex impedance as follows:

$$M^* = i\omega C_0 Z^* \qquad (25)$$

where ω is the angular frequency, $C_0 = \frac{\varepsilon_0 A}{l}$ is the capacitance of the empty capacitor cell having an electrode area A and the distance between electrodes l. ε_0 is the vacuum permittivity. The complex permittivity of the materials is the reciprocal of the complex modulus function:

$$\varepsilon^* = (M^*)^{-1}$$

All these immittance quantities help in describing the contributions of the intrinsic properties of the material in dissipation and storage of charges, but also to make the link to the experimentally observed quantities. The real and imaginary part of the complex permittivity can be used to calculate the loss tangent tan δ by:

$$\tan\delta = \frac{\varepsilon''}{\varepsilon'}$$

This quantity is experimentally important, as the mainly used expression to evaluate the dielectric losses of the dielectric material. Another experimentally important expression is the ac conductivity allowing for the determination of the charge conduction in the capacitor cell. We can express the ac conductivity in terms of the real permittivity and the tanδ as :

$$\sigma = 2\pi f \varepsilon_0 \varepsilon' \tan\delta$$

2.4.2. Laboratory experiment set up

In this thesis, we have used an Agilent 4284A precision LCR meter for impedance analysis. The workstation fitted with two metallic probes with sharp tips is connected to the LCR meter. For the measurement, the probes are connected to the top and bottom electrode of the samples, in our experimental setup the top electrode is the Ag contact created by lithography, and the bottom electrode is the doped Si substrate. A sinusoidal voltage signal with an amplitude of 50 mV is applied on the target electrodes. The ac response from the sample is then measured by the the LCR meter at the same frequency as the applied voltage. A program has been used to calculate the capacitance, the dielectric losses tan δ, the complex impedance Z* and the complex modulus M* from the LCR meter measurement. Measurements have been acquired in the frequency range of 20 Hz – 1 MHz, and were carried out at room temperature in general. Figure 23 shows the experimental setup used for acquiring the impedance spectroscopy data.

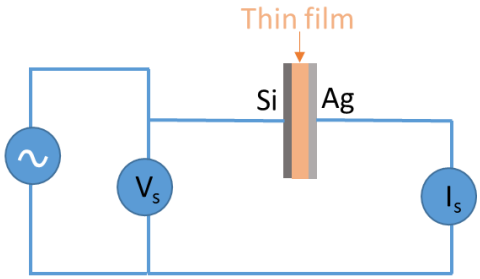

Figure 23 Schematic representation of the electrical set-up used for the impedance analysis

2.4.3. Simulations of the dielectric properties

Experimentally obtained impedance data for a given sample was analyzed by using a mathematical model based on an equivalent circuit, representing the intrinsic properties of the material. For example, the dielectric material between two parallel electrodes as shown in Figure 24 can be understood by a parallel circuit of a resistance (R) and a capacitance (C), and the complex impedance of the circuit is expressed by equation (24) on page 54.

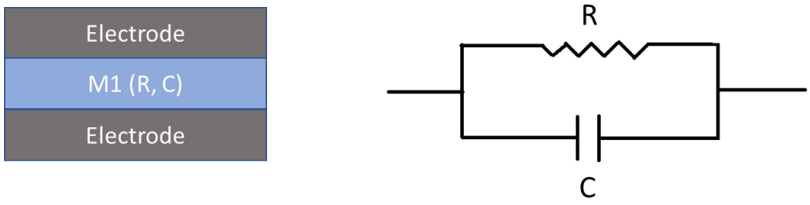

Figure 24 Schematic of a dielectric layer and its equivalent circuit

Similarly, for any more complex capacitor system, the impedance of the material can be simulated by a more complex equivalent circuit. In the case of an inhomogeneous dielectric, a RC-loop is introduced for the different physical components of the dielectric, i.e. for example the different individual layers and the interface layers in a laminate. By fitting the experimentally obtained data with simulations based on the equivalent circuit, one can get the values of the resistivity and the dielectric constant of the different components. The fundamental relation between a dielectric material and the equivalent circuit is based on stimulus voltage, resulting

current and conduction of the free charges through them. Hence, the equivalent circuits are adapted as a fast data analysis tool in the impedance spectroscopy.

In this dissertation the laminate structures are modelled with the three different models based on different assumptions. The schematic of the laminate structure is shown in Figure 25. The individual layer thicknesses of constituent's layer are in sub- nanometric range and the total thickness of laminate is 30 nm. The three models used to fit the experimental data are: (i) Solid solution model, (ii) Series capacitance model and the (iii) Maxwell-Wagner model.

Solid solution model

As the thickness of the individual layers are in the sub-nanometric range, we assumed in this model, that a solid solution of two different material is formed instead of a periodic layered structure. This model will be used to determine the dielectric properties for laminates with a interface roughness exceeding the individual layer thickness. In this case, the total nominal content of each constituent was calculated based on the deposition rate and the number of pulses used for the deposition. For example, consider a laminate structure of two constituents materials A and B, where A is having a thickness of x and B has a thickness of y nm, respectively. We can represent this laminate as A/B (x/y nm). The nominal content of material A (A_n) and B (B_n) can be represented as:

$$A_n = \frac{x}{x+y} \qquad \text{and} \qquad B_n = \frac{y}{x+y}$$

Further, the rule of mixture was applied in order to calculate the dielectric constant of the laminate. For example, if the dielectric constant of A is k_A and B is k_B, the dielectric constant of the solid solution can be represented as:

$$k_{ss} = A_n k_A + B_n k_B \qquad (26)$$

Series capacitance model

In this model we have assumed that the constituent layers remain as individual entities forming a periodic stacked structure, with no charge accumulation at the interface. The total capacitance of the laminate structure (C_L) can then be calculated as the series sum of the individual capacitances of the individual layers (C_A and C_B) as:

$$\frac{1}{C_L} = n_b * (\frac{1}{C_A} + \frac{1}{C_B}) \qquad (27)$$

Where n_b is the number of bilayers in the laminate structure.

For the calculation of the capacitance of the individual layers (Al_2O_3, Y_2O_3 and ZnO), the dielectric constant values obtained from the dielectric study of single films of these materials were used. From equation (27), the apparent dielectric constant can be calculated using the parallel plate capacitor expression (equation (1) on page 13).

Maxwell – Wagner model

In case of the presence of the Maxwell – Wagner (MW) effect in the laminate structures, the accumulation of charges at the interface of the insulator and semiconductor layers gives rise to a space charge polarization and a high dielectric constant can be obtained, higher than the constituents of laminate. Figure 25 shows the example of a laminate structure of Al_2O_3/ZnO with the bottom electrode doped Si (001) and the top electrode Ag. The equivalent circuit of the laminate can be constructed using R-C elements for each layer and the interface between them, as shown also in the Figure 25.

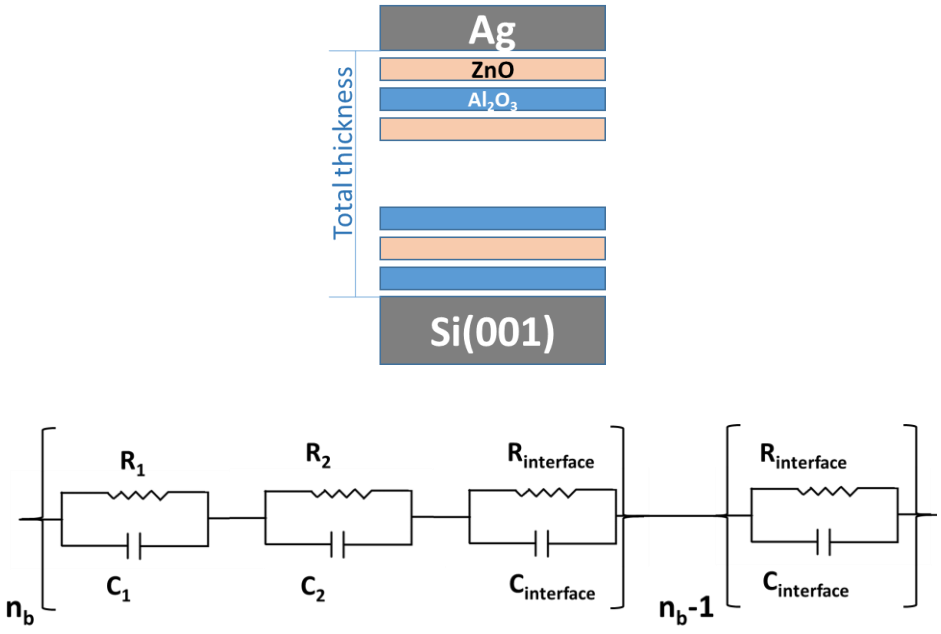

Figure 25 Schematic of the laminate structure and its equivalent circuit following the MW model, where R represents the resistance, C represents the capacitance and n_b represents the number of bilayers

Each individual layer can be represented as a RC circuit where the resistance and the capacitance are related to their charge storing and charge dissipating properties. The total complex impedance of the laminate structure can be written as:

$$Z^* = n_b \cdot \left(\frac{R_1}{1 + i\omega R_1 C_1} + \frac{R_2}{1 + i\omega R_2 C_2} + \frac{R_i}{1 + i\omega R_i C_i}\right) + (n_b - 1) \cdot \left(\frac{R_i}{1 + i\omega R_i C_i}\right) \qquad (28)$$

where n_b represents the number of bilayers in the laminate structure. For each bilayer, two interfaces are present, except for the top-most layer. We can deduce the real and imaginary components of the impedance from equation (28) as:

$$Z' = n_b \cdot \left(\frac{R_1}{1 + (\omega R_1 C_1)^2} + \frac{R_2}{1 + (\omega R_2 C_L)^2} + \frac{R_i}{1 + (wR_i l_i)^2}\right) + (n_b - 1) \cdot \left(\frac{R_i}{1 + (\omega R_i C_i)^2}\right) \qquad (29)$$

$$Z'' = n_b \cdot \left(R_1\left(\frac{\omega R_1 C_1}{1 + (\omega R_1 C_1)^2}\right) + R_2\left(\frac{\omega R_2 C_2}{1 + (\omega R_2 C_2)^2}\right) + R_i\left(\frac{\omega R_i C_i}{1 + (\omega R_i C_i)^2}\right)\right) + (n_b - 1).R_i\left(\frac{\omega R_i C_i}{1 + (\omega R_i C_i)^2}\right)$$

Similarly, we can also get the complex and imaginary part of the electrical modulus using equation (25) as shown by Sinclair and West [81].

The experimental data of the four quantities (Z'', Z', M'' and M') were fitted with the above model, using the thickness, the resistance and capacitance of the individual layers and of the interface as fitting parameters. From the thus extracted resistance and the capacitance values, the resistivity and the dielectric constant of the individual layers and the interface was calculated. The sum of the thicknesses of the constituents was fixed to the experimentally determined bilayer thickness. The fitting was carried out with a self-written MatLab program, allowing to fit the four quantities simultaneously.

The charge density at the interface was calculated using the capacitance of the interface layer and the voltage drop at the interface as:

$$q_i = C_i V_i$$

Where C_i and V_i are the capacitance and voltage drop at the interface. The voltage drop at interface was calculated using the interface resistance (R_i) and the current flowing through the circuit $i = \frac{Z^*}{V}$.

Chapter 3 Growth and properties of single films

As explained in chapter 1, the objective of this thesis is to develop insulator/semiconductor laminate structures of binary oxides with an enhanced dielectric constant creating the Maxwell-Wagner effect at the interface. The physics of these laminates would be challenging to understand if the constituent materials would not have been studied in single films. With this study of the single films of constituent materials, we will establish the effect of deposition parameters on their dielectric properties, and the relation between the properties of the laminates and those of their constituents.

This chapter contains the details about the structural and electrical properties of the PLD grown Al_2O_3, Y_2O_3 and ZnO single films. As the deposition parameters play a vital role in defining the properties of the films, a detailed optimization of deposition temperature and pressure was carried out.

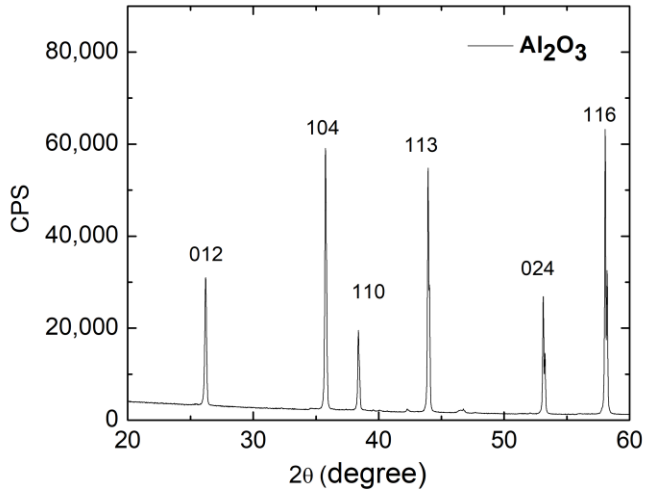

Figure 26 XRD pattern of the Al_2O_3 target

3.1. Al_2O_3 single films

Al_2O_3 thin films were deposited on n-doped Si (001) using the procedure as described in section 2.1.2. As Al_2O_3 has a high thermodynamic stability with Si and a large bandgap, it will be used as an insulator layer in the laminates, after the growth optimization to achieve the desired properties. This part presents the study of the dielectric properties of the Al_2O_3 single films

deposited at a different temperature and pressure. Throughout this section, the thin film material will be referred to by Al_2O_3 for clarity instead of AlO_x, although the stoichiometry of the films is not determined to correspond to the bulk material.

Before starting the deposition, a high-density target of Al_2O_3 was prepared by standard pressing and sintering, and X-ray diffraction (XRD) was conducted to confirm its purity. Figure 26 shows the conventional θ - 2θ scan of the Al_2O_3 target with a monochromatic beam of Cu $K\alpha_1$ (1.5408 Å). The obtained XRD pattern coincides well with the ICDD data of Al_2O_3 and confirms the polycrystalline nature with the absence of any other impurity phase.

3.1.1. Effect of the deposition temperature

In order to evaluate the effect of the deposition temperature, various films were prepared by fixing the deposition pressure to 0.005 mbar and varying the substrate temperature ranging from room temperature to 300 °C. The number of pulses was fixed to 5000. Figure 27 (a) shows the XRR reflectivity curves of Al_2O_3 thin films deposited at different substrate temperatures (RT, 100°C, 200°C and 300°C). All the samples show a high number of oscillations and a constant decrease in the intensity envelop. The amorphous nature of the films was observed by the absence of diffraction peaks in a θ - 2θ scan for all deposition temperatures. The analysis of the XRR curve was carried out as explained in section 2.3.1. Figure 27 (b) shows the evolution of the thickness, roughness, and the density of films as a function of the substrate temperature. The thicknesses of these films were found to be ≅ 40 nm, with a comparable value for the different deposition temperatures, indicating a stable growth rate. The sample grown at 300 °C shows a slightly enhanced roughness, explaining the steeper fall of the intensity envelope in the XRR measurements. The density of the films was found to be independent on the growth temperature and to be approximately about 85-90 % density of bulk Al_2O_3 (Figure 27 (b)).

The dielectric properties of the films are summarized in Figure 28. The dielectric constants are determined to be in the range of about 9, which is consistent with the observations in crystalline materials and other thin films, even in the amorphous phase [55]. Therefore, the films show a typical behavior of amorphous films. The dielectric losses are below 0.01, indicating the high quality of the films and the absence of defect charges. The resulting *ac* conductivity (Figure

28 (b)) does not show a low-frequency plateau, again a sign of the lack of mobile charges, with values going down to 10^{-10} S/cm at low frequency.

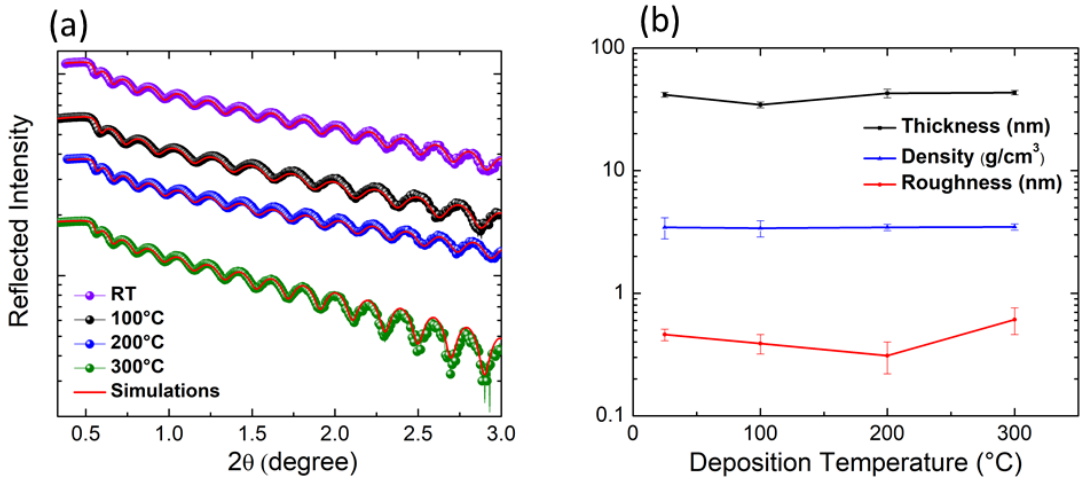

Figure 27 XRR spectra of amorphous Al_2O_3 thin films grown at different deposition temperatures (a), calculated values of thickness, roughness, and density from XRR simulation (b)

All films at different growth temperatures show comparable dielectric properties, and the roughness is only enhanced for the films grown at 300°C. Thus, a stable level of disorder is established in these samples, being topological in nature, as we do not observe the introduction of charges or indications of charge trapping in the films. These properties correspond to what is observed in the literature, indicating the representative nature of these films.

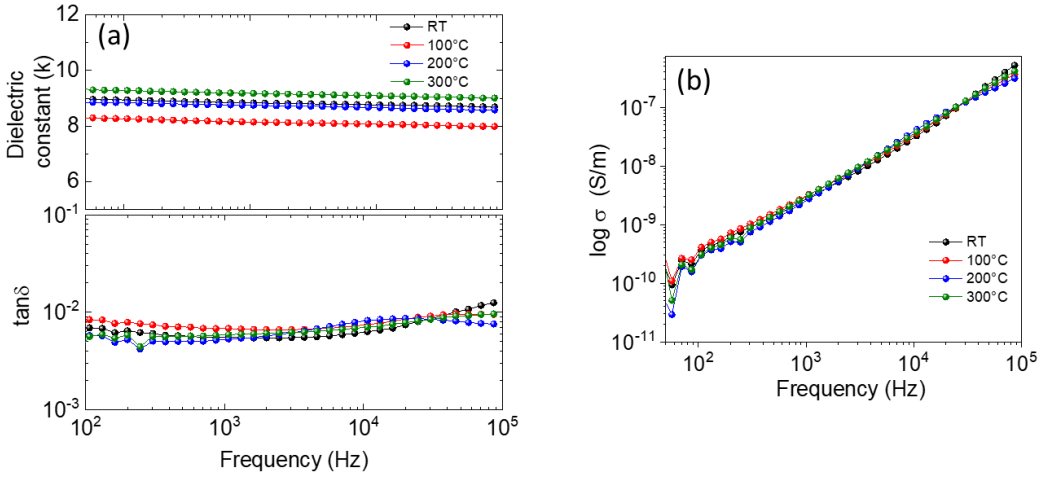

Figure 28 (a) Dielectric constant (top panel) and dielectric losses (bottom panel) of amorphous Al_2O_3 thin films grown at different deposition temperatures. (b) ac conductivity of the same films, calculated from the data in (a)

For the laminate structures and to study the deposition pressure effect, we will use a growth temperature of 100°C, selected due to the following reasons: (a) bulk like dielectric properties, (b) low deposition temperature is always preferable for amorphous films and for industrial applications, and (c) a low film roughness with respect to the 300°C sample leading to a low topological disorder in the film.

3.1.2. Effect of the deposition pressure

In PLD, the pressure in the vacuum chamber affects the growth mechanism of the adatoms on the substrate. A high background pressure in the chamber leads to an increased number of collisions with the ablated particles from the target, which reduces the energy of the ablated particles and hence the film nucleation and growth will be affected. Other than the growth mechanism, the deposition pressure can also affect the stoichiometry of the thin film. For the deposition of the Al_2O_3 single films, an optimal oxygen pressure helps to control the oxidation of Al, leading to optimal Al/O ratios. This part shows the effect of the deposition pressure on the dielectric properties of the Al_2O_3 films. In order to evaluate the impact of the deposition pressure, various films were prepared by fixing the deposition temperature to 100 °C and varying the deposition oxygen pressure (vacuum, 0.005mbar, 0.01mbar, 0.05mbar and 0.1mbar). Figure 29 shows the XRR spectra of the Al_2O_3 thin films deposited at different oxygen pressures.

As the deposition oxygen pressure increases from vacuum to 0.01 mbar, the thickness of the film decreases. At higher pressures, a slight increase in the thickness was observed for films deposited at 0.05mbar and 0.1mbar pressure. Also, the substantial angular decrease of the intensity envelope of the oscillations for 0.05 mbar and 0.1 mbar shows an increase of the roughness of the film. Thus, the high deposition pressure influences the structure of the films. The topographical deterioration for the high deposition pressures is related to the energy loss of the plume species, due to the enhanced scattering while travelling to the sample surface. When adsorbing to the sample surface, the species have lower energies at higher deposition pressures, explaining the less homogeneous surface. Figure 29 (b) shows the effect of deposition pressure on the density and roughness. High deposition pressure leads to a lower density and higher roughness of the films. However, the variations stay small: for the roughness values, it increases

from a value of about 0.6 to 0.7 nm at low pressure to a value of about 1 nm at the highest pressure.

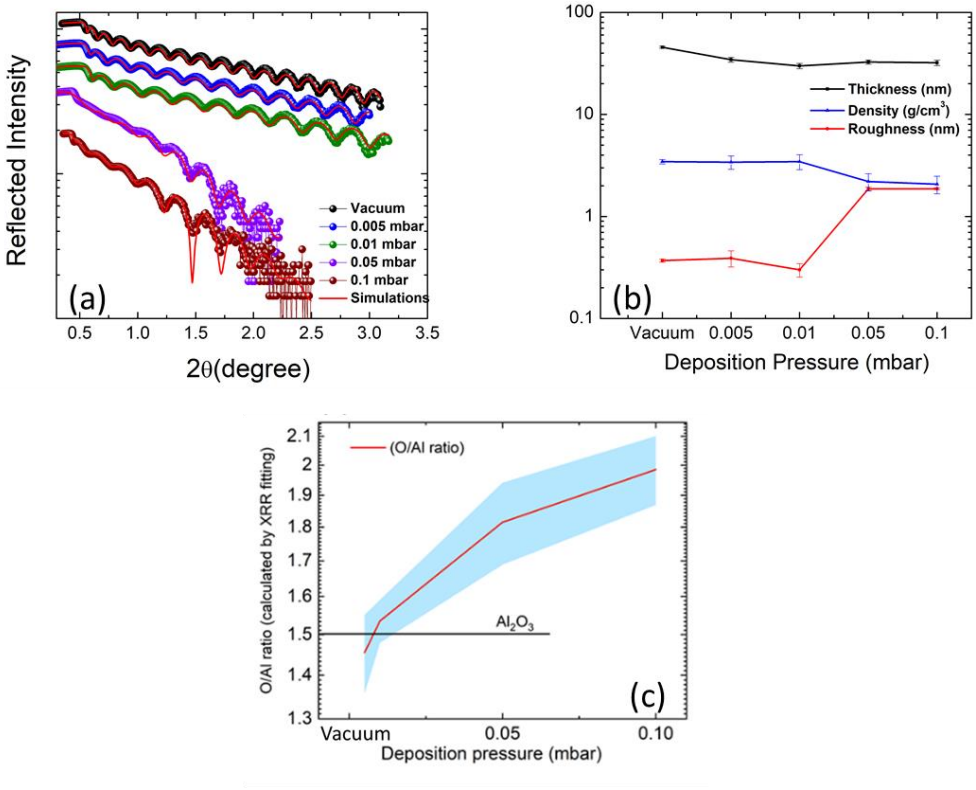

Figure 29 (a) XRR spectra of amorphous Al_2O_3 thin films grown in different oxygen pressure, (b) film thickness of the films vs deposition pressure, (c) O/Al ratio calculated by XRR fitting data (the blue shaded area indicate the error bar on the obtained values).

As to the oxidation of the Al_2O_3 films, favored by the oxygen incorporation into the film at high deposition pressures, it is not possible to quantify exactly. The reliable determination of the oxygen content of a thin film is only possible using Rutherford Backscattering, where the analysis is complicated by the small thickness of the films, and the presence of a thin SiO_x layer at the interface with the Si substrate. Therefore, we are not able to determine exactly the stronger incorporation of oxygen into the film under high pressures, but the XRR analysis can be used to get an indication of the O/Al ratio as the function of the deposition pressure (Figure 29(c)). Appendix 1 shows the method by which the O/Al ratio was calculated. With this method, we cannot make a conclusion on the exact values of the O/Al ratio, but we can visualize the increasing oxygen content in the films with the deposition pressure. For films grown in vacuum

and 0.005 mbar, the determined ratio is comparable to the stoichiometric value for Al_2O_3 (black line in Figure 29 (c)). When increasing the deposition pressure, the O/Al ratio increases as expected, although the obtained values would indicate a phase of AlO_2, which is not reasonable regarding the resulting nominal Al^{4+} oxidation state. However, the possible presence of oxygen pairs in amorphous alumina has been experimentally demonstrated [82] and the comparable formation energies of oxygen interstitials compared to other possible defects on oxygen rich environments have been determined theoretically [83]. Therefore, such a high O/Al ratio may become reasonable in the case of interstitial oxygen pairs, although the decreasing density of the films at high deposition pressures may lead to an overestimation of the O/Al ratio for these samples. Anyway, the XRR analysis confirms the good oxidation of the films already in vacuum and very low oxygen deposition pressures.

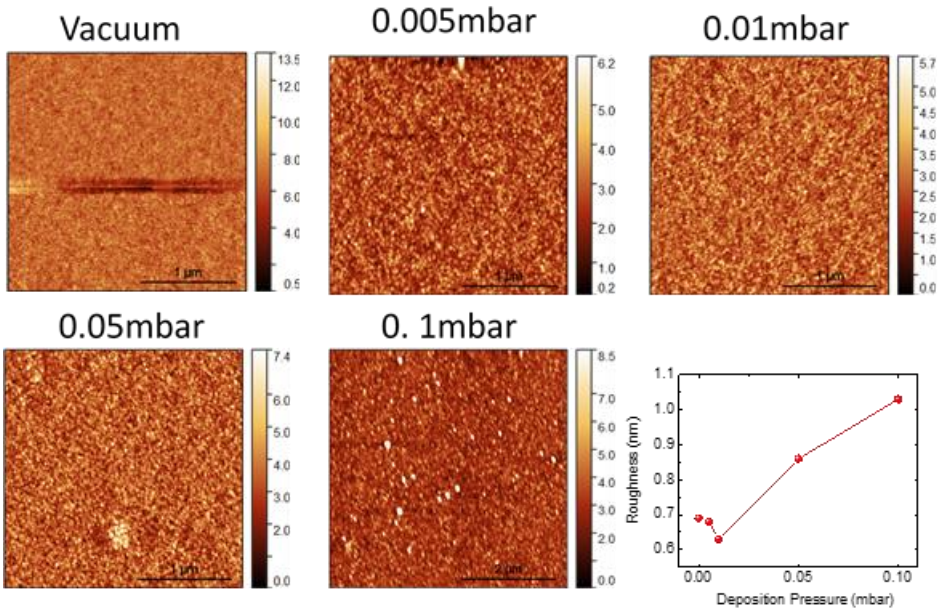

Figure 30 AFM images of amorphous Al_2O3 thin films grown in different oxygen pressure. The figure in the right bottom corner indicates the RMS roughness extracted from the AFM images as a function of the deposition pressure.

AFM analysis was also conducted on the same samples to confirm the roughness values and understand the morphology of the films. Figure 30 shows the morphology determined by Atomic Force Microscopy (AFM) of the different samples. The AFM extracted RMS roughness values increase from a value of about 0.7 nm to 1 nm, as was observed also by XRR. This increase stays small as compared to the film thickness, and the topography indicates the outgrowth of small

domains at high oxygen pressure. No shapes indicating possible voids or pinholes are observed, allowing for a reliable dielectric analysis of these samples.

Concerning the dielectric properties of the amorphous Al_2O_3 films deposited under different oxygen pressures, an overview is given in Figure 31. For the films deposited under a pressure ≤ 0.01 mbar, the properties are comparable to the typical properties of amorphous Al_2O_3 thin films: a dielectric constant of about 9 and dielectric losses below 0.01. It is especially remarkable here that the film deposited under vacuum shows the same properties. The PLD process is a reducing process due to the volatility of oxygen in the ablation process, which is why generally a small background pressure of oxygen is used to ensure few oxygen vacancies and to avoid the introduction of charges in the system. Evidently, even the samples deposited under vacuum (at a pressure of about 7 x 10^{-7} mbar) show the typical properties, underlining the robustness of the dielectric properties concerning a possible sub-stoichiometry of oxygen.

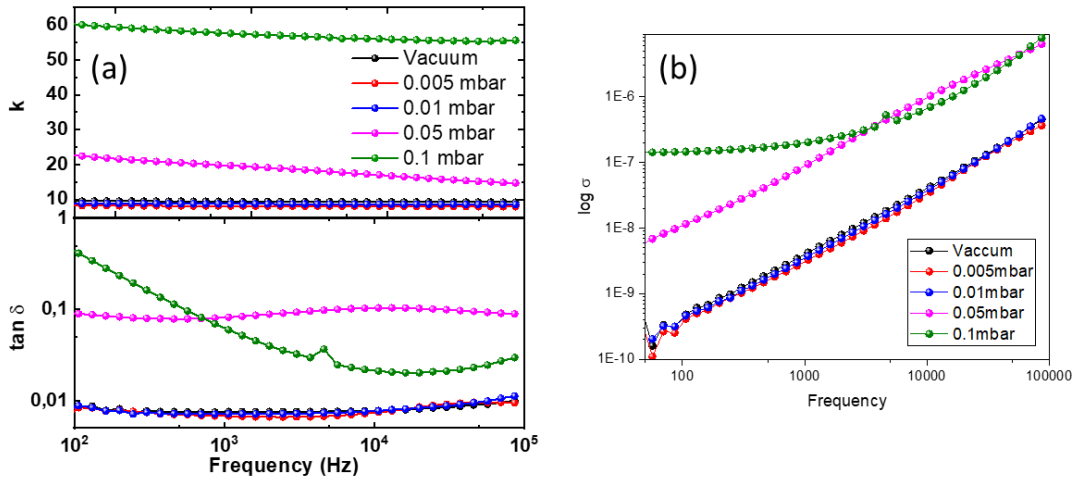

Figure 31 (a) Dielectric constant (top panel) and dielectric losses (bottom panel) of amorphous Al_2O_3 thin films grown at different deposition pressures. (b) ac conductivity of the same films, calculated from the data in (a)

The samples grown at deposition pressures above 0.01 mbar show a gradual enhancement of the dielectric constant, with a concomitant increase of the dielectric losses, especially at low frequency. The developing plateau in the ac conductivity (Figure 31 (b)) clearly indicates the presence of mobile charge carriers at the origin of the increasing dielectric constant, probably due to space charge relaxation at the dielectric/electrode interfaces. The enhancement of the

dielectric constant cannot be attributed to a possibly thicker interfacial SiO_x layer, as due to its smaller intrinsic dielectric constant, a decrease of the observed dielectric constant of the stack would be the effect. Also, the changes of the structure of the films, i.e., density and surface roughness, are rather small and cannot motivate such strong modification of the dielectric properties. Rather, the strong enhancement of the mobile charge density in the films point to the introduction of strong donors in the films, i.e., a chemical modification due to the film stoichiometry.

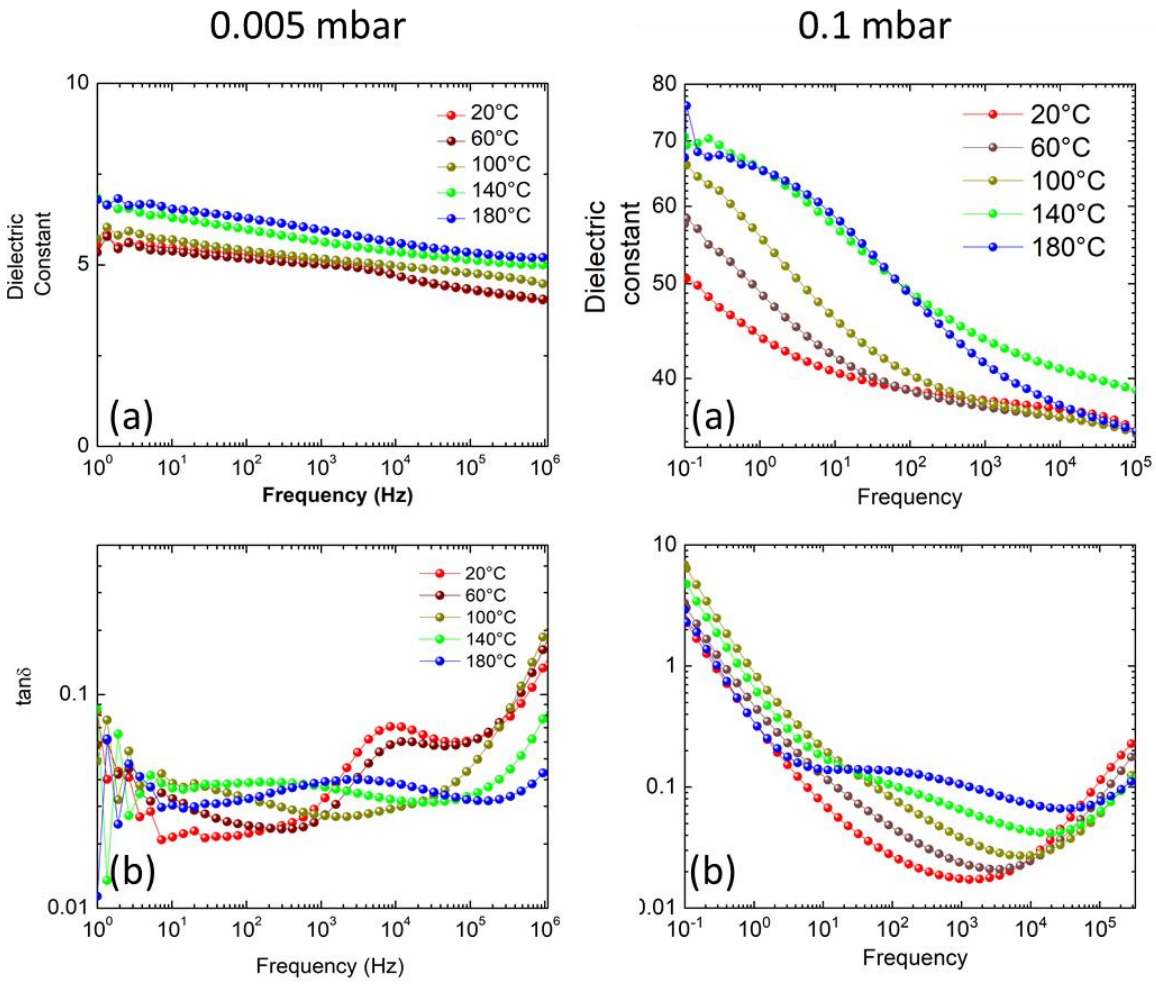

Figure 32 (a) Dielectric constant and (b) tanδ of Al_2O_3 films deposited at 0.005 mbar (left) and 0.1 mbar (right) oxygen pressure

In order to pin down more clearly the characteristics of the charge carriers being at the origin of the dielectric properties of the films deposited under high oxygen pressures, we have carried out temperature – dependent dielectric spectroscopy on samples made in two selected

deposition pressures (0.005 mbar for representative optimal films and 0.1 mbar for the high pressure films). An overview of the temperature dependence of the dielectric constant and the dielectric loss of samples are shown in Figure 32. The dielectric properties of the 0.1 mbar sample are strongly temperature dependent as compared to 0.005 mbar sample (Figure 32 (a)). The dielectric constant was found to increase with temperature for both samples, however the effect is more prominent for the sample deposited under 0.1 mbar oxygen pressure (Figure 33). This increase in dielectric constant is attributed to the space charge polarization produced by the increasing number of free carriers because of the temperature increase. At low frequency, the charge carriers get blocked at the electrodes, which leads to a space charge layer resulting in an increase in polarization and the dielectric constant [55,84,85]. The decrease in the dielectric constant with frequency can be understood because of the reduced movement of the charge carriers under high frequencies. The strong dependence of the dielectric constant in the 0.1 mbar sample shows the availability of more high mobile charge carriers, which may be related to the chemical modifications arising due to stoichiometric changes in the film.

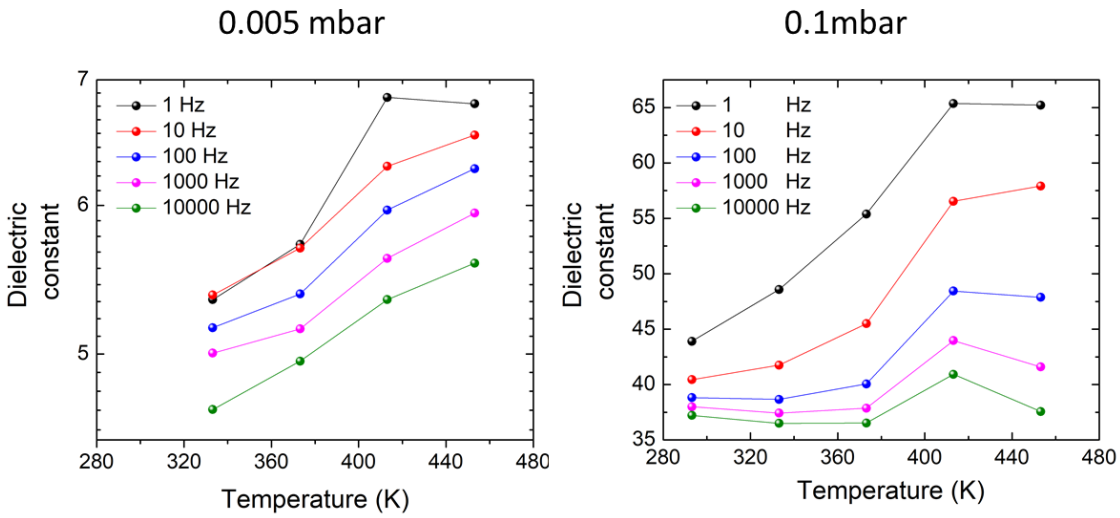

Figure 33 Temperature dependent dielectric constant of Al_2O_3 films deposited at 0.005 mbar and 0.1 mbar

In order to understand the conduction mechanism, the temperature dependent ac conductivity of these samples is plotted as shown in Figure 34. For the 0.005 mbar sample, the conductivity is not highly sensitive to the temperature and follows the power law

$$\sigma = A\omega^s \qquad (30)$$

The value of *s* is calculated from the slope of the log(σ) vs log(ω), which was found to be in the range of 0.9 to 1. *s* is decreasing slightly with temperature before stabilizing at high temperature (inset Figure 34). This behavior is related to electron hopping conduction in the amorphous films due to the presence of localized states in the forbidden gap[55 86 87]. Many studies have shown this behavior in amorphous films.

The activation energy was calculated from the slope of log(σ) vs $^1/_T$ using the Arrhenius equation for conductivity ($\sigma = \sigma_0 e^{\left(\frac{-E_a}{k_B T}\right)}$), where E_a is activation energy and K_B is the Boltzmann constant (Figure 35). The activation energy was found to be 0.072 eV at 10 Hz and 0.078 eV at 100 Hz and with increase in the frequency was found to decrease to 0.022 eV at 1000 Hz. This decrease in the activation energy with frequency is also related to the hopping type of conduction [87]. The value of the activation energy itself seems to be very small compared to the value of 1.5 eV given in the available literature on amorphous Al_2O_3 [88]. However, a theoretical paper of G. Blaise [89] predicts activation energies below 0.1 eV in the case of extremely low disorder. Although the activation energy is low, the low density of states leads to a negligible electronic conduction, as observed in the ac conductivity of the 0.005 mbar film.

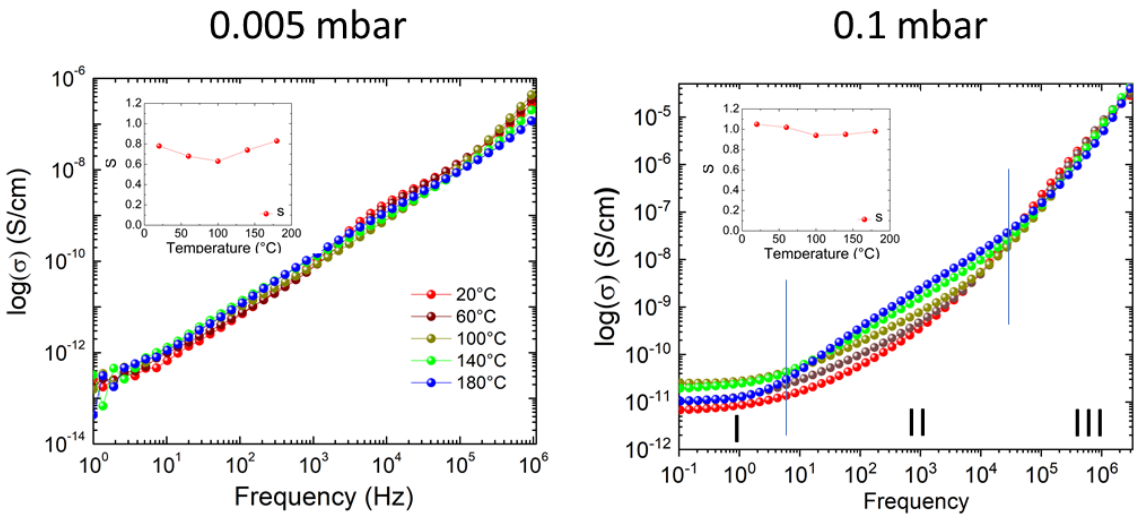

Figure 34 Temperature dependent conductivity of the 0.005 mbar (left) and 0.1 mbar (right) films. The insets show the obtained s values, for the 0.1 mbar samples, the values from region II are shown

The 0.1 mbar sample shows a more complex temperature and frequency dependence, with three different regions. Such a complex frequency and temperature dependence confirms the

more complex situation observed also for the dielectric constant and the dielectric losses in the high-pressure films.

Region I in Figure 34 shows a dc conductivity plateau, which is frequency independent but temperature dependent, indicating the presence of free charge carriers in the film. Their density increases with the temperature and results in high dc conductivity. The activation energy was found to be 0.098 eV at 10Hz (Figure 35). This value, slightly higher but comparable to the values found in the 0.5 mbar sample, indicate that the conduction charges have a comparable origin. The observed macroscopic conduction indicates a higher density of these defect charges in the 0.1 mbar film.

In **Region II** (Figure 34), the conductivity is increasing with frequency and temperature. Here, the activation energy increases to approximately 1.4 eV at 100 and 1000 Hz. Again, equation (30) was used to describe the data. The obtained *s* values are situated around 1, as shown in the inset of Figure 34.

Region III in Figure 34 is the temperature-independent part, and the conductivity is increasing with frequency following $\sigma = A\omega^s$ where the value of s is between 1.8 to 2 at all temperatures. This kind of behavior is characteristic for a finite resistance at the electrode interface of the film, dominating the results at high frequencies [90].

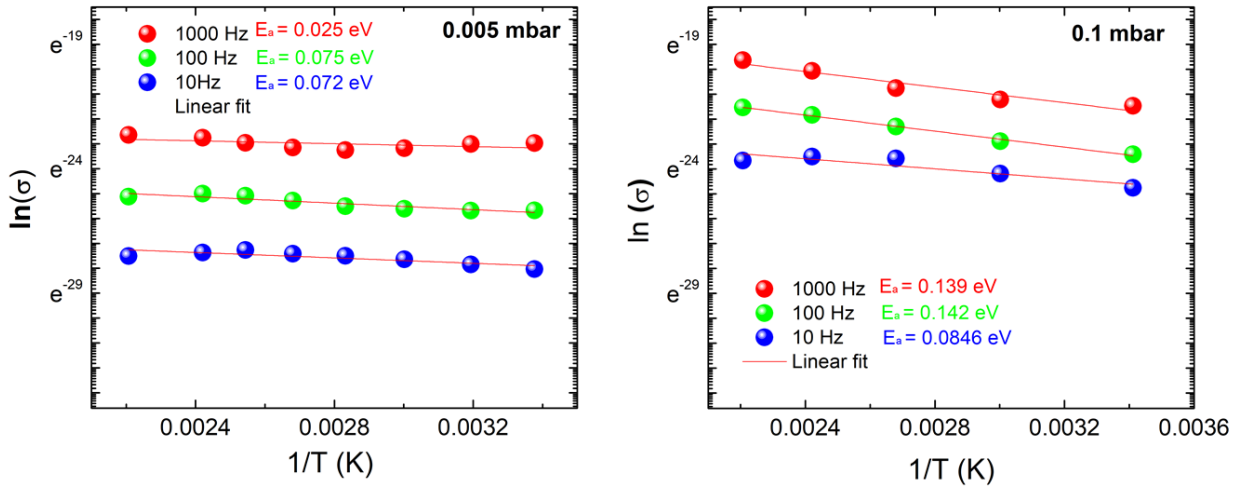

Figure 35 Activation energy for 0.005 and 0.1 mbar samples at 10, 100 and 1000Hz

In the 0.005 mbar sample, which is comparable to optimal amorphous Al_2O_3 films available in the literature, the low losses and the absence of a frequency-independent plateau in the ac conductivity at low frequencies indicate a small defect density. In the case of the 0.1mbar sample, an increase of the O/Al ratio above 1.5 indicates the introduction of excess oxygen, with resulting chemical defects. These chemical defects could be interstitial oxygen [83], which acts as a fixed charge center and adds up an extra energy level situated at 1eV above the valence band [91 92]. The energetic positioning of these bands could account for the charges with an activation energy of about 1.4 eV observed only in the 0.1 mbar sample.

Coming back to the initial motivation of the single film growth, i.e. the optimization of the deposition parameters for the laminate growth, a pressure of 0.005mbar was preferred because of the low defect densities and the absence of dc conductivity.

3.2. Y_2O_3 single films

Y_2O_3 thin films were deposited on n-doped Si (001) by PLD, as described in section 2.1.2. Before starting the deposition, high-density targets of Y_2O_3 were prepared by standard pressing and sintering, and XRD analysis was conducted to confirm their purity. Figure 36 shows the conventional θ - 2θ scan of the Y_2O_3 target with a monochromatic beam of Cu $K\alpha_1$.

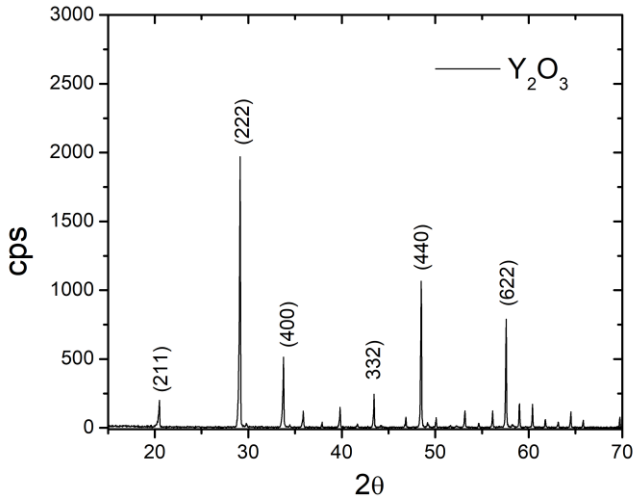

Figure 36 XRD pattern of Y_2O_3 target

The obtained XRD pattern coincides well with the ICDD data of Y_2O_3 and confirms the polycrystalline nature with the absence of any other impurity phase. Detailed optimization of deposition parameters (temperature and pressure) was performed in order to obtain the required properties of the films.

3.2.1. Effect of the deposition temperature

The amorphous character of the films was established by XRD. A typical XRD pattern of the Y_2O_3 thin film deposited at different temperature (100 °C, 200 °C and 300 °C) shows no reflection from crystalline phases, which is due to the absence of the long-range order in the films. Therefore, all the samples are amorphous in nature.

XRR measurements were carried out on the films to determine their density, thickness and roughness by the analysis of the oscillation period, critical angle and the angle dependence of the exponential envelop of the intensity [93]. Figure 37 shows the XRR curves with the fit results for Y_2O_3 thin films deposited at different temperatures. The fitted profiles match well with the experimental data if a layer of SiO_x at the interface of film and substrate is introduced. The formation of the SiO_x layer on Si substrate is a well-known fact [94], and cannot be avoided due to the oxygen exposition of the substrate in the early stages of the film growth. Its presence and thickness (limited to some nanometers) will be taken into account in the analysis of the dielectric data.

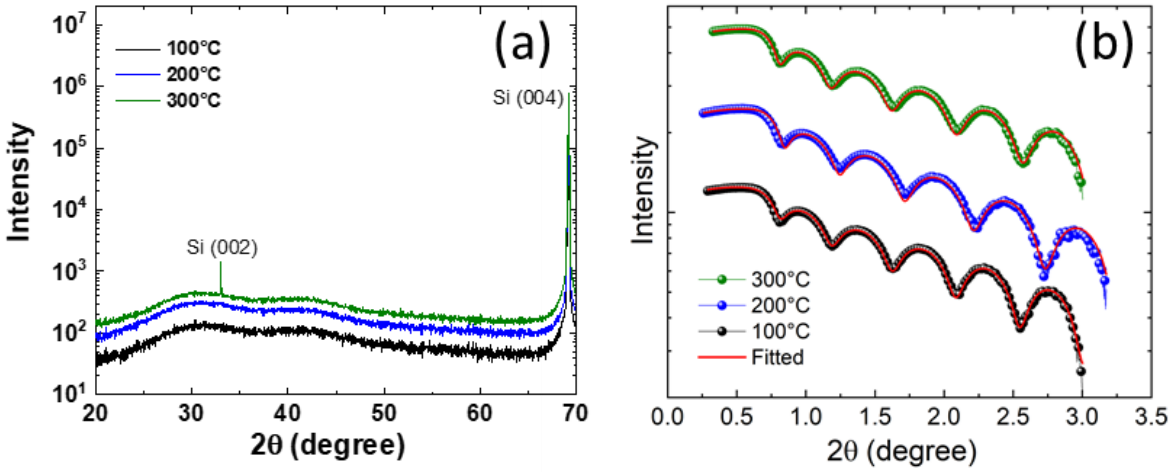

Figure 37 XRD and XRR pattern of Y_2O_3 films deposited at different deposition temperature

The deposition temperature was found to have a limited effect on the thickness, i.e. the growth rate of Y_2O_3 films (the fit results are summarized in Table 1). The extracted thicknesses of the films are ≈ 17nm. The roughness of the films is between 0.5 and 0.6 nm, and decreases for the film grown at 300°C, illustrating the change in the atomic arrangement due to the enhanced energy of the adsorbed species.

Deposition parameters	Thickness (nm)	Roughness (nm)	Density (g/cm^3)
100°C	17.8 ± 0.3	0.61 ± 0.05	4.52 ± 0.005 (≈90%)
200°C	16.8 ± 0.4	0.62 ± 0.09	4.67 ± 0.009 (≈93%)
300°C	17.8 ± 0.3	0.55 ± 0.01	4.74 ± 0.001 (≈94%)
0.005 mbar	17.8 ± 0.3	0.61 ± 0.05	-
0.01 mbar	17.7 ± 0.45	0.59 ± 0.12	-
0.05 mbar	18.4 ± 1.3	0.51 ± 0.22	-
0.1 mbar	21.7 ± 2.3	2.9 ± 0.6	-

Table 1 Thickness, roughness, and density of Y_2O_3 thin films as a function of the deposition temperature and deposition pressure

The density of the films can be extracted from XRR, as described in section 2.3.1. In Figure 37(b), θ_c is observed to be roughly stable through different deposition temperatures, and as a compositional change of these films is not expected because of the fixed deposition oxygen pressure, θ_c can be used to evaluate the film density. The fit results show a density of above 90% of the bulk value of 5.03 g/cm^2 [95], with an enhancement of the density with the deposition temperature. The enhanced energy of the adsorbed species at high temperatures leads to a closer packing of the films, and hence the density increases with the deposition temperature.

The deposition temperature dependence of the dielectric properties were studied using impedance spectroscopy. Figure 38 (a) shows the dielectric constant of Y_2O_3 films deposited at 0.005 mbar pressure as a function of substrate temperature and frequency. As the substrate temperature increases, the dielectric constant of the films decreases. The inversely proportional relation of dielectric constant and substrate temperature of Y_2O_3 thin films is in accordance with the results of other studies [96 97]. Films deposited at low temperatures are amorphous with a lower packing density, and therefore higher defect densities [57]. These defects can act as charge trap centers and increase the space charge polarization in the films, explaining the high dielectric constant at 100 °C. At higher deposition temperature, the packing density is enhanced, as shown

by the XRR results (Table 1), leading therefore to a reduction of defect density accompanied by the reduction of space charge polarization and hence a reduction of the dielectric constant.

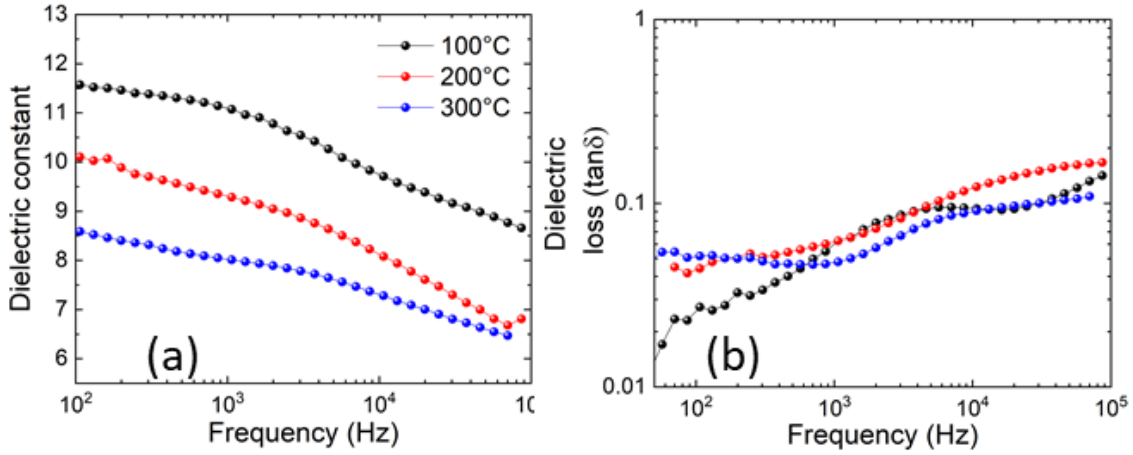

Figure 38 Dielectric properties of the Y_2O_3 films deposited at 0.005mbar pressure as a function of substrate temperature and frequency

As to the dielectric losses, they are situated for all samples of the temperature series below 0.1, which is an acceptable level. Regarding the ac conductivity (Figure 39), calculated from the dielectric data [55], no low frequency plateau related to dc conductivity is observed, again indicating a highly insulating behavior. It is interesting to note, that although the evolution of the dielectric constant indicates a higher defect level in the low temperature films, the dielectric losses and the ac conductivity do not show an important evolution, indicating that these defect charges are deeply trapped in the Y_2O_3 film, and do not contribute to a possible conduction in the films.

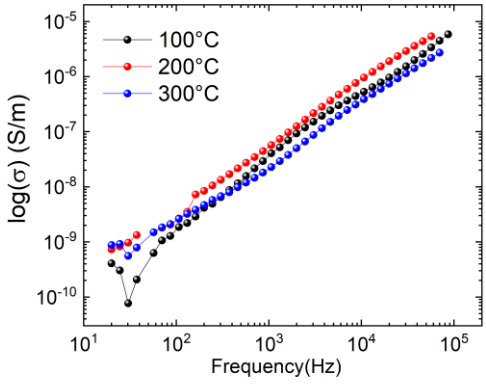

Figure 39 Conductivity of Y_2O_3 films deposited at different temperatures

For the laminate structures and to study the deposition pressure effect, we will use a growth temperature of 100°C because of the higher dielectric constant and the low losses. Again, the use of a low temperature is preferable for materials for the use in complex electronic devices.

3.2.2. Effect of the deposition pressure

In order to evaluate the impact of the deposition pressure on the dielectric properties, various films were prepared by fixing the deposition temperature to 100 °C and varying the deposition oxygen pressure (vacuum, 0.005mbar, 0.01mbar, 0.05mbar and 0.1mbar). Figure 40 shows the XRR spectra of the Y_2O_3 thin films deposited at different oxygen pressures.

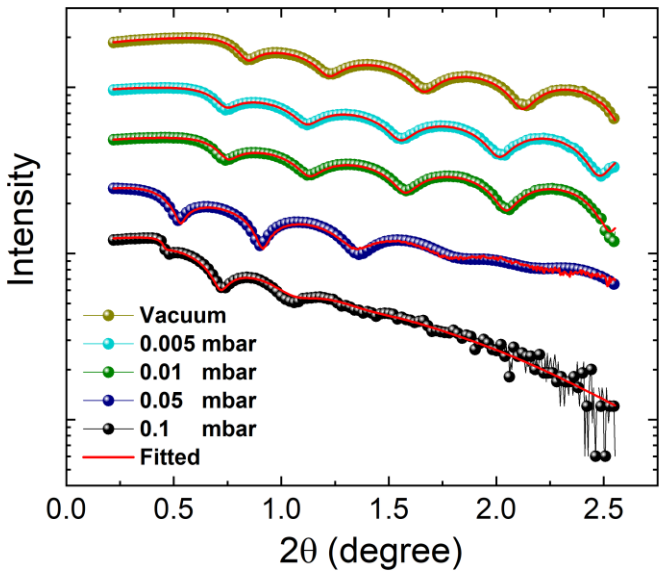

Figure 40 XRR curves of the Y_2O_3 films deposited at different oxygen pressures

The growth of the films was found to be strongly influenced by the oxygen deposition pressure. As the oxygen pressure increases, the XRR oscillations die out at lower angles, indicating a lower quality of the films. At 0.1 mbar and 0.05 mbar oxygen pressure, oscillations are not visible above 1.5 ° and 2.5 °, respectively, while at lower pressures (0.005 mbar and 0.01 mbar), well-defined oscillations up to high 2θ values suggest a smooth film growth. Table 1 (page 76) summarizes the thickness and roughness values of the Y_2O_3 thin films extracted from the XRR fits as a function of deposition pressure. The roughness increases strongly for the sample

deposited under 0.1 mbar as expected from the overall aspect of the experimental data. The high-pressure samples (0.1 mbar and 0.05 mbar) show a higher error of the fit results because of the low number of oscillations present, but the thickness seems to increase. This is possibly an effect of the better availability of oxygen from the deposition atmosphere, allowing for a higher deposition rate than in the case of low pressures.

The critical angle θ_c varies strongly (Figure 40). Here, both the density and the film composition may evolve: At high background pressure during the growth, a higher number of collisions reduce the energy of the plume species before they reach the substrate surface. The low energy of the adsorbed species favors the possible formation of voids, decreasing the film density, and the increase of the roughness, as is observed in the fit results. On the other hand, the high background pressure may also change the film composition, where more oxygen atoms may be incorporated. The increasing film thickness with higher deposition pressure is probably a sign of such a process. Therefore, the interpretation of θ_c is not straightforward in this case, and the detailed analysis of the oxygen composition of the films is extremely difficult due to the lack of adapted techniques.

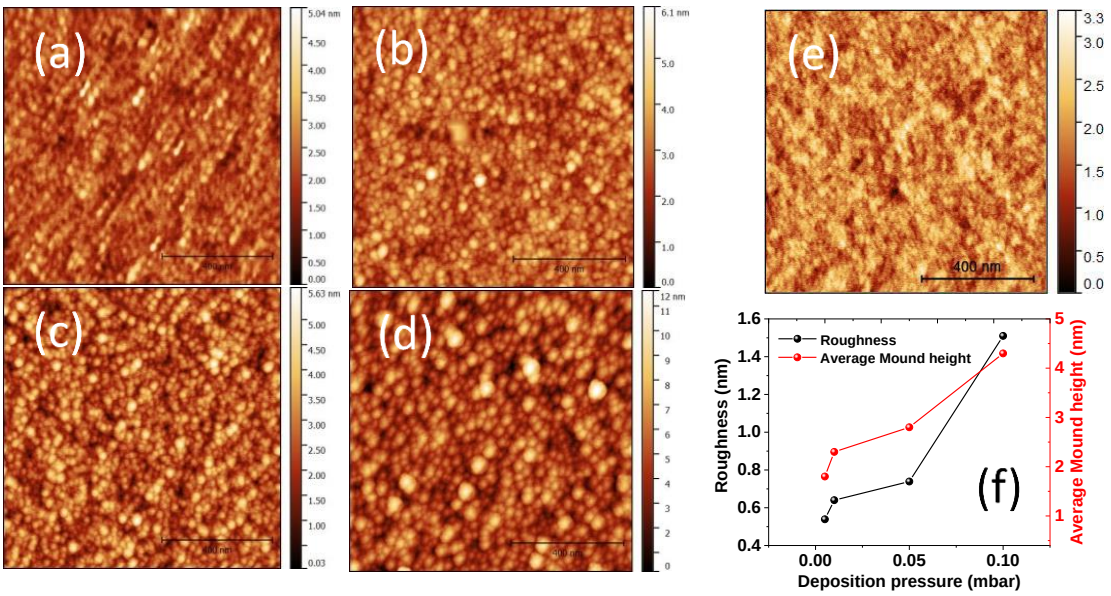

Figure 41 AFM images of Y_2O_3 thin films deposited at (a) 0.005 mbar, (b) 0.01 mbar, (c) 0.05mbar and (d) 0.1 mbar O_2 pressure. (e) AFM image of Y_2O_3 film deposited at 300°C and 0.005 mbar pressure, (f) Evolution of roughness and mound size as a function of deposition pressure

Thus, based on the XRR data, we are not able to conclude clearly on the density changes with deposition pressure, and therefore the most important indicator of the film quality is not accessible. An AFM study of the surface of the films deposited at different pressures (Figure 41) allows to extract the RMS roughness and confirms the overall quality loss at high deposition pressures, as observed in the XRR data. The roughness increases strongly due to the formation of mounds, reaching a height of 5 nm, corresponding to roughly 30% of the film thickness (Table 1).

Figure 42 shows the influence of deposition pressure on the dielectric constant and dielectric losses of Y_2O_3 thin films. As the deposition pressure increases, the dielectric constant decreases and the low frequency dielectric losses increase. This observed behavior, with better dielectric properties for samples deposited under low oxygen pressure, is somehow surprising. The O/Y ratio in Y_2O_3 is expected to enhance for higher oxygen pressures by compensating the lack of oxygen due to the reducing character of the ablation process. The thickness evolution (Table 1) indicates a limited growth at low deposition pressure, which may be related to the lack of oxygen. At higher deposition pressures, the growth rate increases, indicating a better oxidation of the films. Concerning the dielectric constant, the observed decrease with the deposition pressure may be explained in the same way as for the temperature dependence: The oxygen sub-stoichiometry at low pressures can lead to an increase of trapped charges in the Y_2O_3 films that, on the application of an *ac* electric field, act as pseudo-dipoles and enhance the dielectric constant. When the deposition pressure increases, the oxygen vacancies and the trapped charge density decrease, which can explain the observed reduction in the dielectric constant of the film.

However, this mechanism cannot account for the signs of enhanced mobile charge carriers at high deposition pressures, as the increase of the low frequency dielectric losses and the ac conductivity (Figure 42). In crystalline Y_2O_3 films, oxygen deficiency introduces a change in the density of states and reduces the energy bandgap [98]. It has also been reported that post-annealing under oxygen of thin Y_2O_3 films can reduce the leakage current density by improving the stoichiometry of Y_2O_3 [99, 96]. Thus, in crystalline films, a good oxygen stoichiometry leads to lower dielectric losses, which is not the observed evolution in this study on amorphous films.

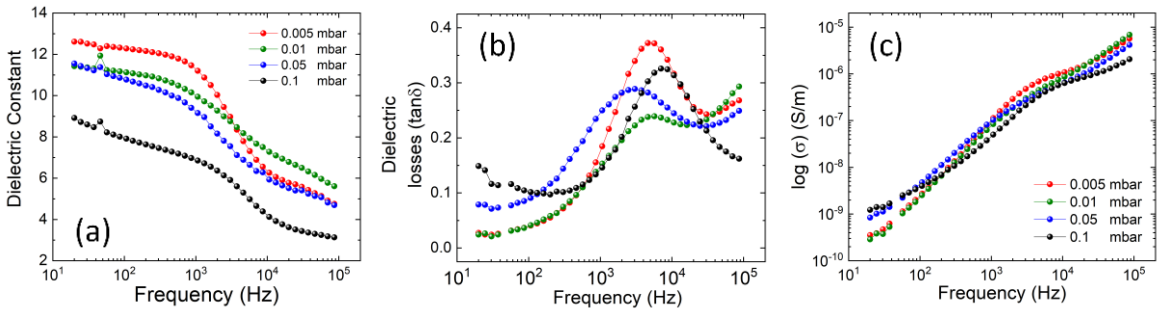

Figure 42 Dielectric constant (a), dielectric losses (b), and ac-conductivity (c) as a function of frequency for samples deposited under different deposition pressures

However, the increase of the oxygen pressure leads also to an enhanced roughness and the formation of mounds (Figure 41) in the films. Rough dielectrics and therefore rough top electrodes are known to enhance free charge carriers in the film, and therefore losses and the leakage current [97]. This mechanism is kicking in for the film at 0.05 mbar, where an enhancement of the low frequency dielectric losses is observed. When the pressure further increases to 0.1 mbar, the losses increase even further, in good agreement with the increase of the roughness of the films.

The strong influence of the roughness can also be observed in the leakage current density with the applied field strength (Figure 43). At zero bias, a current density of approx. 10^{-8} A/cm^2 is reached for all samples. The field strength, at which an abrupt increase in current density is observed, is considered as the breakdown field. As the deposition pressure increases, the breakdown occurs at lower field strength. The observed changes of the structure and the morphology for the pressure series, especially the increase in void density and depth at high deposition pressure, will also have a strong influence on the breakdown field [100]. The voids create a low ohmic path through the film due to the locally reduced film thickness, and therefore reduce the breakdown strength. Hence, the film deposited at 0.1 mbar pressure shows the lowest breakdown strength, and film deposited at 0.005 mbar pressure shows a high breakdown strength (Figure 43 (b)), due to its high growth quality.

Therefore, care must be taken in the development of high quality, amorphous Y_2O_3 dielectrics on the oxygen atmosphere. Generally regarded as a good lever to ensure the complete oxidation

of thin films, and therefore to achieve satisfying dielectric properties, the use of a high deposition pressure decreases however the energy of the adsorbed species on the surface of the sample. For crystalline films, i.e. using a high deposition temperature or a high-temperature annealing, this lack of energy is compensated by the thermal energy, but for amorphous films, being deposited at much lower temperatures, it leads to the formation of an important roughness and voids, which may in extreme cases lead to the formation of pinholes. The dielectric properties are deteriorated by this enhancement of the roughness, winning the trade-off with the increased oxidation.

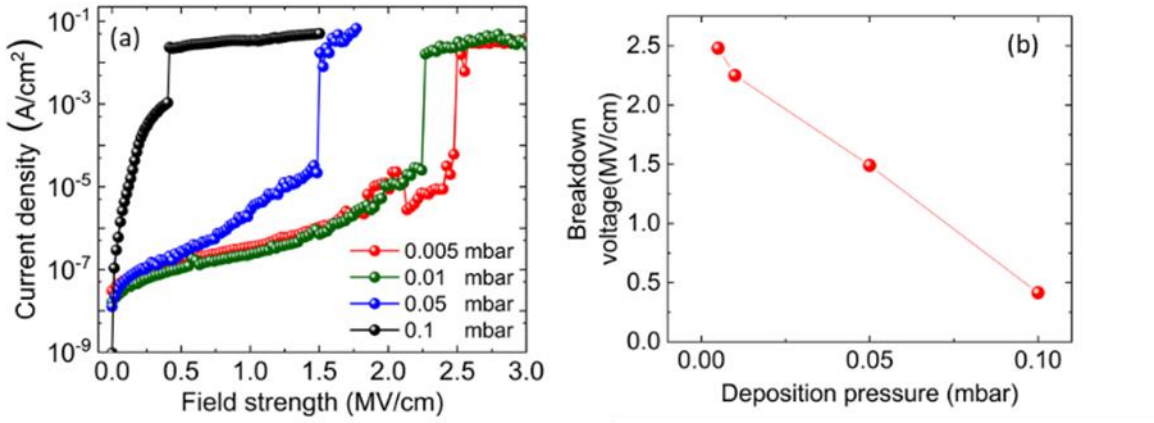

Figure 43 (a) I-V characteristics of Y2O3 thin films deposited at different oxygen pressures, (b) breakdown strength of Y2O3 films as a function of deposition pressure

Based on the study of single films of the insulators (Al_2O_3 and Y_2O_3), we conclude that the best deposition parameters for the dielectric films with limited topological and chemical defects are: deposition temperature – 100 °C, oxygen deposition pressure - 0.005 mbar, laser energy – 200 mJ and the substrate target distance should be 80 mm. With these deposition parameters, the obtained properties of these films are almost similar to their bulk values, which ensures the presence of limited defects in the films. For the deposition of the laminates, we have used these parameters in order to have bulk like insulating properties of these materials.

3.3. ZnO single films

Zinc oxide (ZnO) is a n-type semiconductor which has attracted research interest for the applications in electronics. The ability of ZnO to accommodate free charges makes it a perfect

semiconductor to be used in laminates for provoking a high Maxwell – Wagner effect. Hence, in order to optimize the deposition parameters, single films of ZnO were deposited and were characterized for their electrical and structural properties.

ZnO thin films were deposited on n-doped Si (001) by Pulsed laser deposition (PLD) technique as described in the experimental chapter. As it has been observed in the Al_2O_3 and Y_2O_3 thin films, the deposition parameters can affect largely the morphology and the electrical properties of the thin films, hence, the optimization of the deposition parameters becomes an essential task for achieving the desired properties in ZnO films as well. As ZnO is known for its tunable electrical properties, the deposition parameters become even more critical for the electrical properties of ZnO.

Before starting the deposition, a high-density target of ZnO was prepared by standard pressing and sintering, and X-ray diffraction (XRD) analysis was conducted to confirm its purity. Figure 44 shows the conventional θ - 2θ scan of the ZnO target with a monochromatic beam of Cu $K\alpha_1$. The obtained XRD pattern coincides well with the ICDD data of ZnO and confirms the polycrystalline nature with the absence of any other impurity phase.

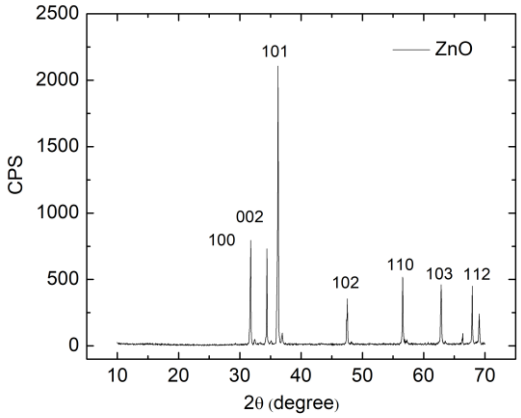

Figure 44 XRD pattern of ZnO Pallet

3.3.1. Effect of the deposition temperature

In order to evaluate the effect of the deposition temperature, ZnO films were prepared by fixing the deposition pressure to 0.005 mbar and varying the substrate temperature ranging from 100 °C to 300 °C. A sample at room temperature was also prepared but was not stable under

ambient conditions. Structural analysis was carried out using XRD measurements at high angle and XRR. The XRR measurements were analyzed by fitting the experimental data, allowing to deduce the thickness, the roughness and the density of films.

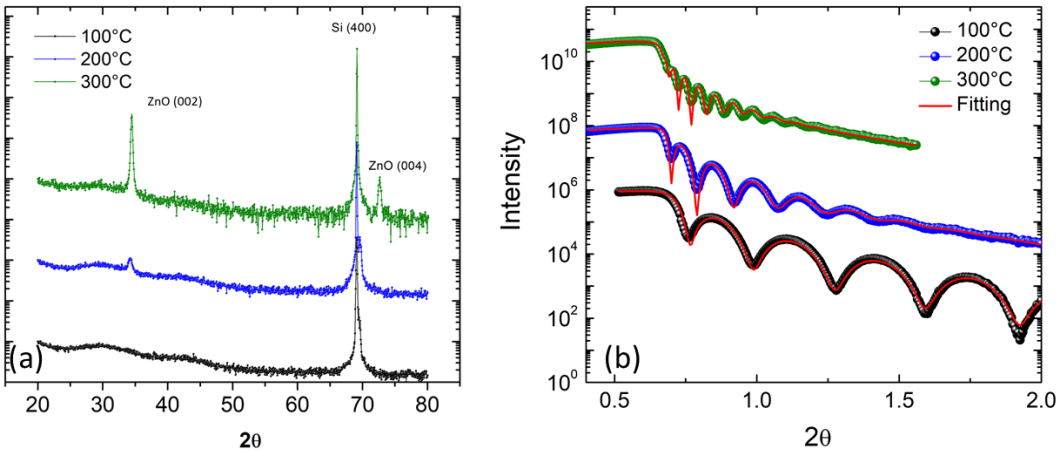

Figure 45 (a) XRD and (b) XRR pattern of the ZnO thin films deposited at different substrate temperatures

The XRD scan of the ZnO films is shown in Figure 45. In the films deposited at 200 °C and 300 °C, other peaks than the substrate Si (004) peaks are visible. It shows that the films deposited at these temperatures have developed a crystalline structure, while the film deposited at 100 °C is found to be amorphous in nature. High substrate temperatures (>250°C [101]) facilitates the long range ordering in ZnO, and at 300°C, single crystalline films with the same orientation as the substrates were obtained. At 200 °C, the intensity of the ZnO (002) peak is smaller, and no ZnO (004) peak is observed, so at this temperature, the crystallization of ZnO has just started, and a certain volume of the film is still amorphous. As in this thesis, we are focusing on amorphous films to avoid the charge movement through the grain boundaries, we have therefore used a substrate temperature of 100°C for the growth of the laminates.

Deposition temperature	Thickness (nm)	Roughness (nm)
100°C	24.5 ±.75	0.8 ± 0.15
200°C	42.2 ± 1.3	2.2 ± 0.7
300°C	90.2 ± 1.5	4.2 ± 1.4

Table 2 Thickness and roughness of ZnO films as a function of substrate temperature

Figure 45 (b) shows the XRR reflectivity curves of ZnO thin films deposited at the different substrate temperatures. All the samples show a high number of oscillations and a constant decrease in the intensity envelop. The analysis of the XRR curve was carried out as explained in the chapter 2 using the GenX software. The thickness of the film was found to be increasing strongly with the substrate temperature (Table 2), although the number of the laser pulses was kept constant. Therefore, the substrate temperature provides the required energy to the adatoms to diffuse on the substrate and helps in the formation of crystalline ZnO. However, the growth at high temperature (200 and 300°C) will also increase the grain size [102] , and it could lead to the high observed roughness values for the film deposited at 200 and 300°C (Table 2). This increase in the roughness causes the disappearing fringes in the intensity envelop of XRR pattern at low incidence angles for 200°C and 300°C. The density of all the films were found to be 85 – 90 % of the bulk density of ZnO.

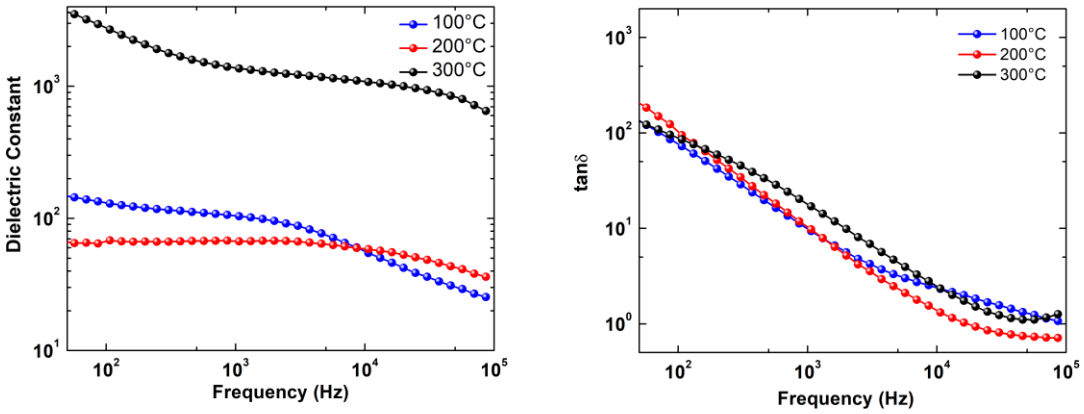

Figure 46 Dielectric constant and tanδ for the ZnO films deposited at different temperatures

Figure 46 shows the dielectric properties of the ZnO films as a function of deposition temperature and the frequency. The ZnO film deposited at 300°C temperature shows an exceptionally high dielectric constant as compared to the films deposited at 100°C and 200°C, which clearly indicates the effect of crystallinity on the dielectric properties. It has been reported before by R. Ondo-Ndong et al. that the dielectric constant of ZnO films (prepared by sputtering) increases with the substrate temperature [103]. But also the values of the dielectric constant for the 100°C and 200°C samples are more than an order of magnitude higher than the bulk dielectric

constant of ZnO. This is because of the oxygen vacancies in ZnO arising due to the low oxygen pressure during deposition, which will be discussed in the next section in detail.

3.3.2. Effect of the deposition pressure

In order to evaluate the impact of the oxygen deposition pressure on the dielectric properties, various films were prepared by fixing the deposition temperature to 100 °C and varying the deposition oxygen pressure (vacuum, 0.005 mbar, 0.01 mbar, 0.05 mbar and 0.1 mbar).

Figure 47 shows the XRR spectra of the ZnO thin films deposited at different oxygen pressures. The reduction in the fringe width of the films with the deposition pressure shows that the thickness and hence the deposition rate of ZnO decreases with the increase of the deposition pressure (Table 3). A ZnO film were also deposited at 0.1 mbar but no fringe was observed in the XRR pattern. This indicates either an extremely low thickness or an important roughness, so we excluded it from the study. The decrease of the deposition rate with the pressure may indicate the loss of energy of ejected atoms from the target because of high number of collisions with the background oxygen. However, a decrease in roughness of the films with the deposition temperature is also observed, indicating again a tendency to roughness if the energy of the adsorbed species on the substrate is high. In this regard, low oxygen pressures are comparable to high deposition temperatures.

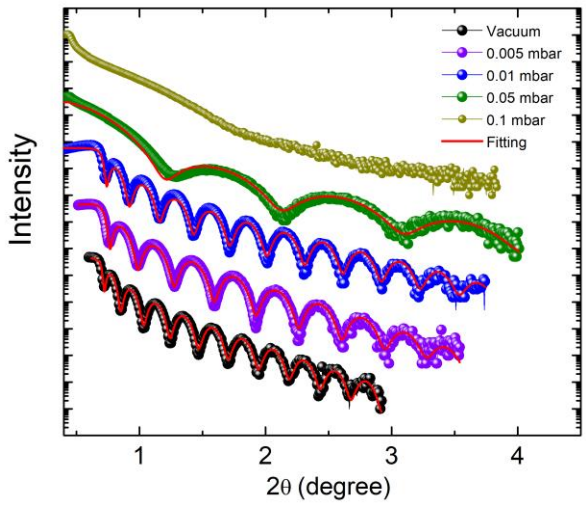

Figure 47 XRR of ZnO films as a function of deposition pressure

Deposition temperature	Thickness (nm)	Roughness XRR (nm)	Roughness AFM (nm)
Vacuum	32.8± 0.7	0.8 ± 0.2	1
0.005mbar	24.5 ± 0.7	0.8 ± 0.15	0.73
0.01 mbar	27.5 ± 0.4	0.6 ± 0.13	0.54
0.05 mbar	9 ± 1.5	0.4 ± 0.14	0.49

Table 3 Thickness and roughness of ZnO films as a function of deposition pressure

Figure 48 shows the morphology of the ZnO films as a function of the deposition pressure. The evolution of roughness with the deposition pressure, obtained from AFM imaging and XRR fitting, are matching well. The small difference could be due to the fact that in AFM imaging, the roughness values are obtained only on a small film area (250µm x 250µm), while in XRR the roughness values are obtained from the whole sample.

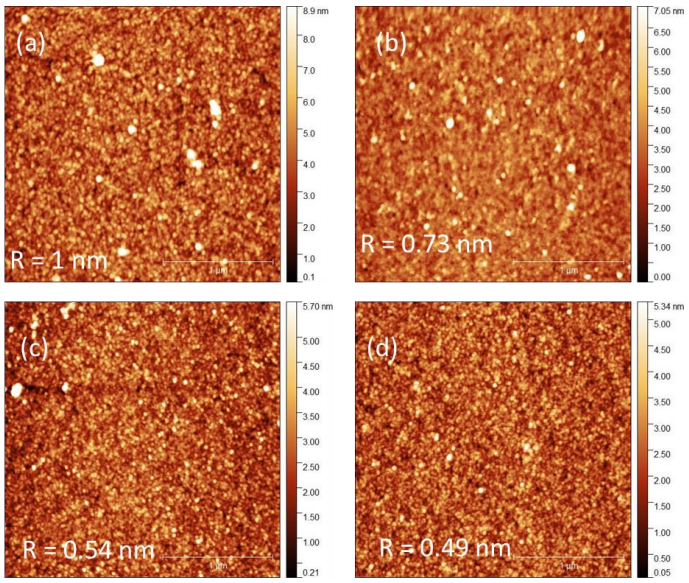

Figure 48 AFM images of ZnO thin films deposited at (a) vacuum, (b) 0.005 mbar, (c) 0.01 mbar and (d) 0.05 mbar O_2 pressure.

Figure 49 shows the influence of deposition pressure on the dielectric constant and dielectric losses of ZnO thin films. As the deposition pressure increases, both quantities decrease. This behavior can be understood well with the native defects in the ZnO thin films [104]. It is a well-reported fact, that ZnO may introduce native point defects like O vacancies, depending on the partial pressure during deposition. In this study, the film deposited at vacuum (no oxygen in chamber) showed a conducting character (data not shown here), which is because of a high

number of oxygen vacancies in the film. The oxygen vacancies add donor levels in the band gap and trap the electrons, participating in the conduction [105]. When the deposition pressure increases from vacuum to 0.05 mbar, a gradual decrease in oxygen vacancies is expected, which reduces the trapped charge density. In the dielectric studies, when an ac electric field is applied, these trapped charges enhance the macroscopic polarization in the film and a high dielectric constant is obtained at 0.005mbar deposition pressure (Figure 49(a)). A gradual decrease in the dielectric constant is observed with the deposition pressure because of the reduction in oxygen vacancies. The reduction in the trapped charges with the deposition pressure can also be seen in tanδ values of the films (Figure 49 (b)), where a reduction in losses is observed as the deposition pressure increases from 0.005mbar to 0.05 mbar.

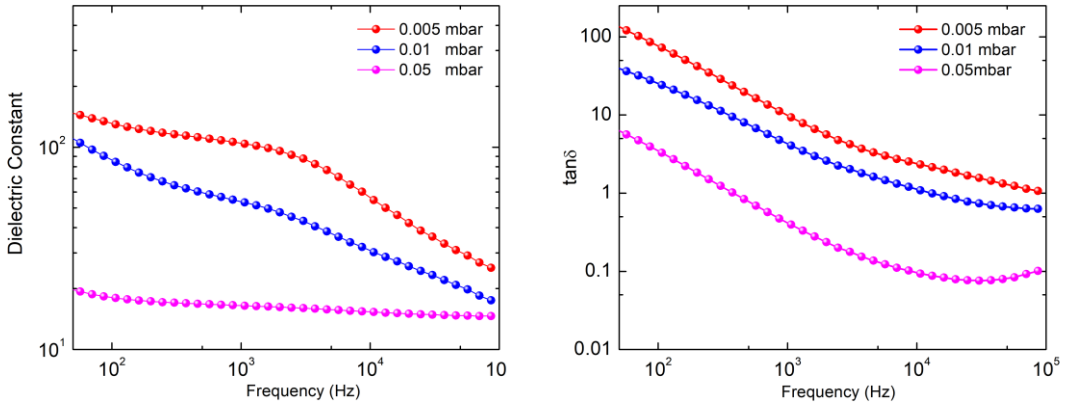

Figure 49 Dielectric constant (a), dielectric losses (b), and ac-conductivity (c) as a function of frequency for samples deposited under different deposition pressures

Chapter 4 Sub-nanometric laminates of binary oxides

The optimization of the single films of the three chosen binary oxides, Al_2O_3, Y_2O_3 and ZnO, has provided us with the necessary preliminary knowledge on the properties of the constituent materials in order to generate the Maxwell-Wagner (MW) effect in sub-nanometric laminates. Although the properties of the materials are strongly dependent on the deposition conditions, we have identified the adapted conditions to obtain insulating Al_2O_3 and Y_2O_3 films, which will therefore be used as the insulating layers in the MW laminates, and charge-doped ZnO, which will be used as a charge donor layer in the laminate. In this chapter, I will present the results on three types of sub-nanometric laminates: first, Y_2O_3/Al_2O_3, without any semiconducting layer. In this system, we do not expect a MW effect, but it will serve as a control system. Second, Al_2O_3/ZnO, and third, Y_2O_3/ZnO. In these latter laminates, we do expect a MW effect, and the use of two different insulating layers will allow comparing the results and choosing the optimal system.

4.1. Al_2O_3/Y_2O_3 laminates

Al_2O_3/Y_2O_3 laminate structures have been grown and analyzed in order to understand the dielectric behavior of laminates of two insulators. As the possibility of having charges in these two materials are negligible, the probability of finding the MW effect is also negligible, but the study of these laminates will give us an insight of the laminate development and the reference compared to the introduction of semiconductor layers in this kind of laminates. In this section, a detailed overview of the properties of Al_2O_3/Y_2O_3 sub-nanometric laminates is presented.

As we know, laminates can have more interesting properties than their constituent materials. Nanolaminates of Al_2O_3/Y_2O_3 have been studied for optical waveguide applications [106]. Some studies have shown the influence of the bilayers on optical properties of Al_2O_3/Y_2O_3 nanolaminates deposited by thermal atomic deposition [107]. It was reported that the optical band gap of the laminates can be modulated by changing the Y_2O_3 thickness in the laminate structure. Lin et al have presented that the laminate structure of amorphous Al_2O_3/Y_2O_3 on GaAs (001) can have a dielectric constant similar to that of pure Y_2O_3 and does not follow the Vegard's law, which would predict a linear change with composition [108]. However, a low trap charge

density at the interface of the substrate makes Y_2O_3 interesting for the low leakage applications. Study of bulk Y_2O_3 doped Al_2O_3 showed no remarkable changes in the dielectric properties except the increase in the dielectric losses due to the formation of secondary phase $Al_5Y_3O_{12}$. In this study, we have tried to understand the effect of individual layer thickness of Y_2O_3 and Al_2O_3 on the dielectric properties of the laminates.

The deposition of the laminates was carried out by PLD as described in section 2.1.2. A deposition temperature of 100°C and an oxygen pressure of 0.005mbar were selected for the deposition of the laminates based on the single film study of Al_2O_3 and Y_2O_3, as shown in the previous chapter. The deposition rates for both materials were calibrated by the laminate calibration procedure (section 2.3.2) and were found to be 0.003nm/pulse and 0.004nm/pulse for Al_2O_3 and Y_2O_3, respectively. In total, a series of 9 samples were prepared with various individual layer thickness combinations for Al_2O_3 and Y_2O_3 (as shown in Figure 50 (a)). For all laminates, a constant total thickness of 30 nm was maintained by adapting the number of bilayers. Figure 50(b) shows the schematic representation of the laminate structure.

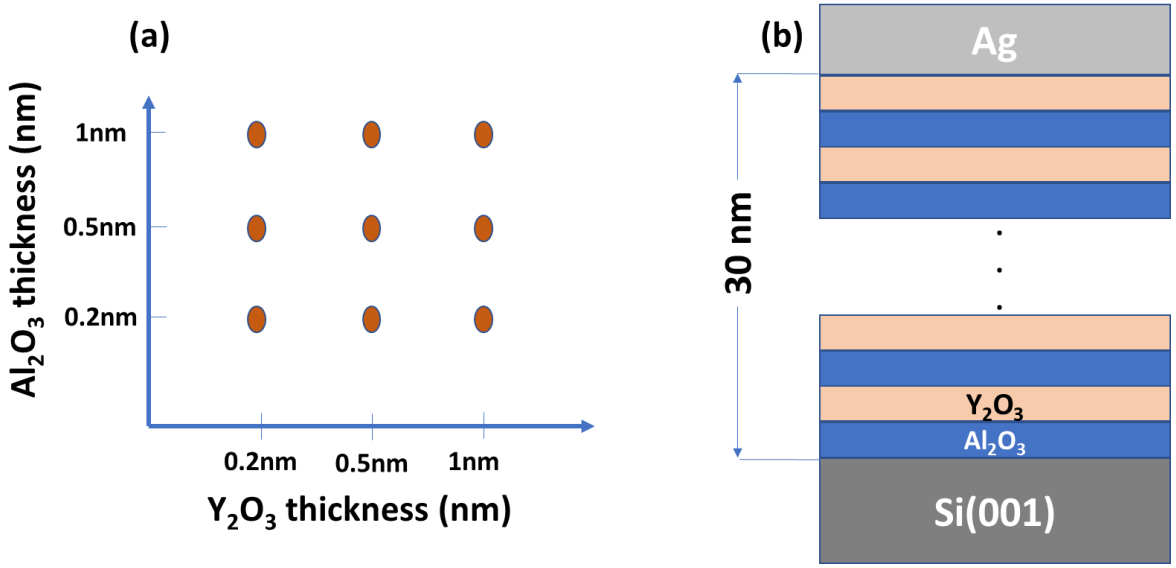

Figure 50 (a) 9 samples with different thickness combinations for the individual layer thickness, (b) schematic representation of the laminate structure with keeping total thickness 30 nm

4.1.1. Structural properties

Figure 51 shows the XRR pattern for the Al_2O_3/Y_2O_3 laminates with different individual layer thickness. The XRR analysis of each laminate confirms the good agreement with the deposition rates, and for all laminates, an individual layer thickness with an error of less than 5 % was obtained. Out of the 9 prepared samples, we are showing the results of three selected samples, because of the presence of the bilayer peak representing the high quality of the artificial periodicity of the laminate structures. As the intensity envelop in the XRR dies out at large angle ($2\theta > 6.5°$ in our case), the bilayer peak for the laminates having a bilayer thickness less than 1.5 nm are not visible due to its high angular position. Figure 51 (a) shows the pattern obtained for Al_2O_3/Y_2O_3 (1/1 nm) laminate with total 15 bilayers. The total thickness was found to be 30.7 nm with a Bragg peak at 4.12° (red arrow in Figure 51 (a)). Similarly, Figure 51(b) and (c) shows the laminates Al_2O_3/Y_2O_3 (1/0.5 nm) and Al_2O_3/Y_2O_3 (0.5/1 nm). These laminates have the same bilayer thickness of 1.5 nm, even though the individual layer thicknesses are different for the two constituent materials, hence they both have the Bragg peak coinciding at 5.87°. These results confirm that the laminate structure is formed even when the individual layer thicknesses are in sub-nanometric ranges.

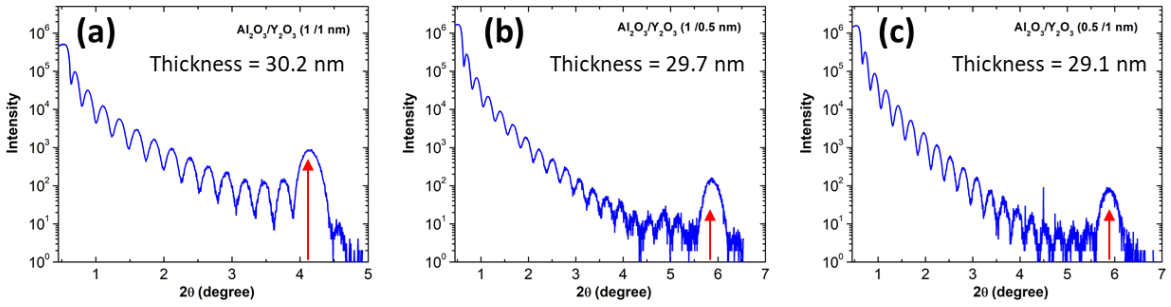

Figure 51 XRR pattern of (a) Al_2O_3/Y_2O_3 (1/1 nm) (b) Al_2O_3/Y_2O_3 (1/0.5 nm) and (c) Al_2O_3/Y_2O_3 (0.5/1 nm) with total nominal thickness of 30 nm

4.1.2. Dielectric properties

For each sample, the apparent dielectric constant and the losses are measured as a function of the frequency in the range of 10^2 to 10^5 Hz. In Figure 52, the dielectric properties of the Al_2O_3/Y_2O_3 laminates for different individual layer thickness configurations (0.2, 0.5 and 1 nm)

are drawn, the dielectric data is arranged as samples are represented in Figure 52(a). In horizontal direction, the thickness of Y_2O_3 layer is increasing while in vertical direction, the thickness of Al_2O_3 layer is increasing. With this series of samples, it is possible to identify the effect of (i) the Al_2O_3 layer thickness at constant Y_2O_3 thickness (ii) the Y_2O_3 layer thickness at constant Al_2O_3 thickness, and (iii) the total bilayer thickness (diagonal from bottom left to top right). Note that, increasing the total bilayer thickness by keeping the total laminate thickness constant corresponds to a decrease of the number of interfaces in the laminate. However, the dielectric properties of these laminates are comparable to what was observed in the single films, and especially, they do not show an enhancement of the dielectric constant due to the MW effect.

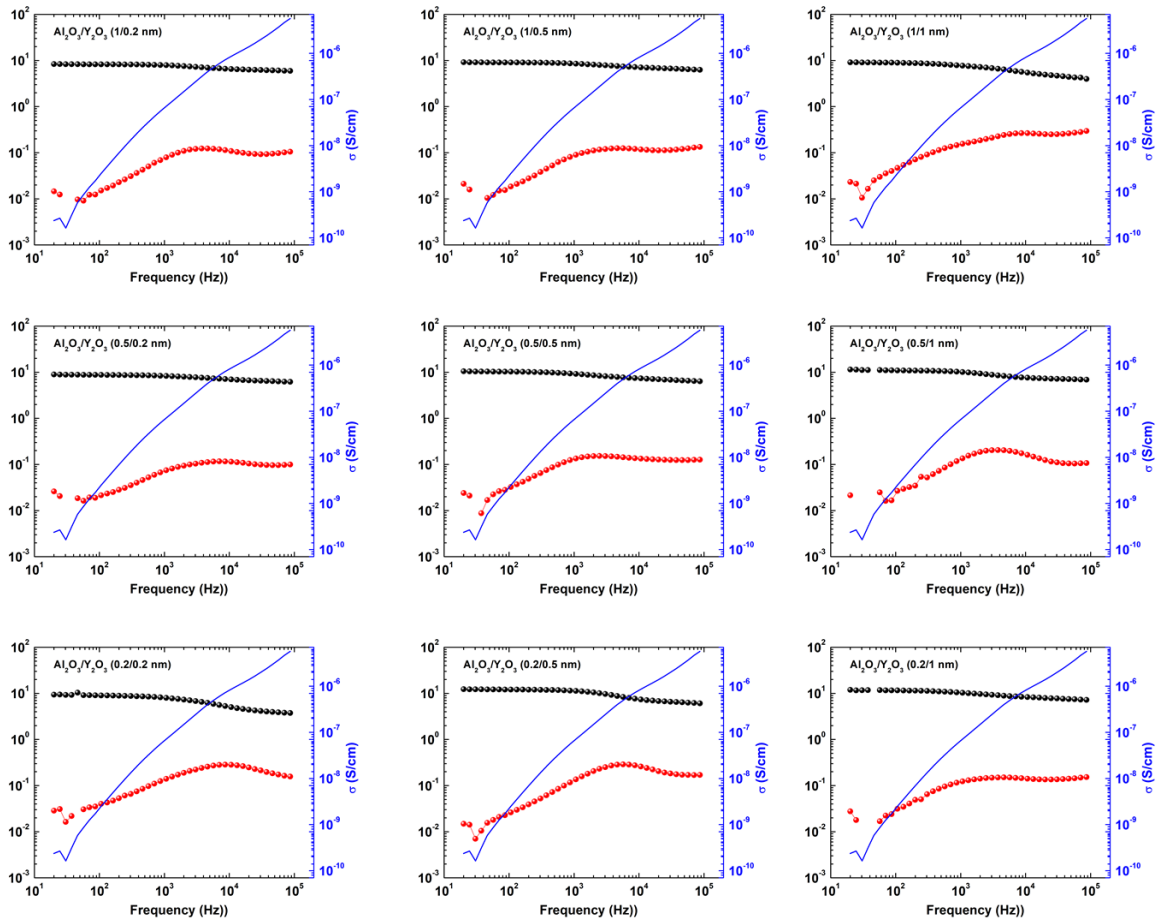

Figure 52 Dielectric properties of Al_2O_3/Y_2O_3 laminates. The black dots indicate the dielectric constant and the red dots the dielectric losses (both on the left axis). The blue line indicates the ac conductivity (right axis). In the vertical direction, the individual thickness of the Al_2O_3 layers increases, in the horizontal direction that of the Y_2O_3 layers, taking the values of 0.2, 0.5 and 1 nm.

For a more detailed analysis:

(i) With the increase in the Y_2O_3 thickness at constant Al_2O_3 thickness in the laminate, the dielectric constant was found to increase. This can be understood from the series capacitance model (section 2.4.3). As the nominal thickness of the Y_2O_3 (relative thickness in the laminate) increases, the dielectric constant of the laminate increases correspondingly because of the higher dielectric constant of Y_2O_3. All samples were found to be following the series capacitance model (Figure 53). However, a slight increase in the tanδ was also observed as the nominal content of Y_2O_3 in the laminate increased.

(ii) With the increase in the Al_2O_3 thickness at constant Y_2O_3 thickness in the laminate the dielectric constant was found to decrease, again because of the low dielectric constant of Al_2O_3.

(iii) The effect of the bilayer thickness on the optical properties of nanolaminates showed an increase in their optical band gap with the decrease in the bilayer thickness from bilayer thickness 20 to 1nm [109]. We also observe such a decrease in tan δ when the bilayer thickness decreased from 2 nm in Al_2O_3/Y_2O_3 (1/1 nm) to 1 nm in Al_2O_3/Y_2O_3 (0.5/0.5 nm). However, when the bilayer thickness reaches 0.4 nm in Al_2O_3/Y_2O_3 (0.2/0.2 nm), again an increase in the tan δ was observed. This could be related to the presence of more defect-induced localized states in the band gap in case of such ultra-thin bilayers.

The ac conductivities of all the samples showed no low frequency plateau, which indicates that absence of free charge carriers. The ac conductivities values at 200 Hz were found to be in the range of 10^{-9} S/cm, which shows that these laminates could be useful for gate dielectric applications.

This study of Al_2O_3/Y_2O_3 sub-nanometric laminates shows that laminate structures can be obtained in the sub-nanometric range with an optimal control of the individual layer thickness of the constituent materials. The dielectric properties showed that in order to have a MW effect at the internal interfaces of the laminates, a sufficient charge density is required in one of the

constituent layers, so that these charges can accumulated and can enhance the interfacial polarization on application of alternating electric field. This study shows that a semi-conducting layer has to be introduced in the laminates to obtain the MW effect, but also that the growth method, the electrode nature or other aspects of our sample treatment does not induce an enhanced dielectric constant independently of any free charges in the laminate or a MW effect.

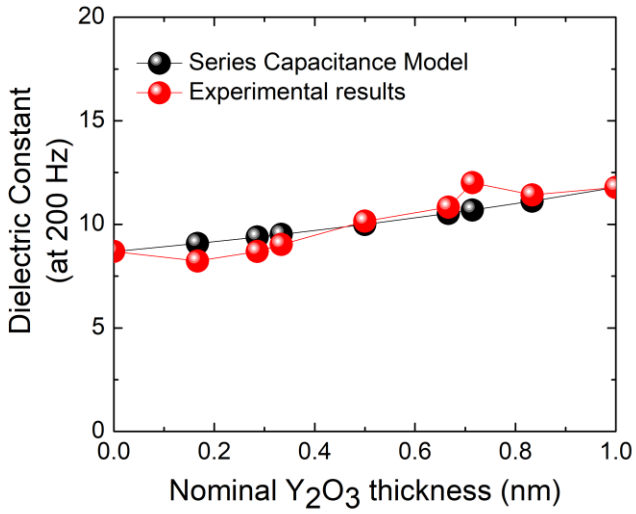

Figure 53 Experimental data with the series capacitance model

4.2. Al_2O_3/ZnO laminates

After characterizing the dielectric properties of the single films of the Al_2O_3 and ZnO individually, growth conditions were selected to grow their laminates. Based on this optimization, a deposition temperature of 100 °C and an oxygen pressure of 0.005 mbar were selected to develop the amorphous Al_2O_3/ZnO sub-nanometric laminates, as standard conditions. The first 4 parts of this section are dedicated to their structural properties (section 4.2.1), to their dielectric properties (section 4.2.2) and the simulation (section 4.2.3), as well as to a high-temperature study of the dielectric properties (section 4.2.4). However, as the deposition pressure has a very strong influence on the properties of both constituents, we have chosen also to vary the

deposition pressure in order to investigate the role of the properties of the individual layers in the last part (section 4.2.5).

4.2.1. Structural properties of laminates grown under standard conditions

To obtain a reliable thickness for the laminates, the deposition rates were calibrated as described in the chapter 2 (section 2.3.2). The XRR results of the calibration samples were already presented in Figure 21 in that section in order to illustrate the calibration process, but are presented again here in Figure 54 (a) for clarity. The bilayer Bragg peak, visible for each calibration laminate and indicated by an arrow in Figure 54 (a), demonstrates the presence of the artificial periodic arrangement of the Al_2O_3 and ZnO layers throughout the laminate. The bilayer peak in Al_2O_3/ZnO (1000/100) laminate represents the bilayer of 2.9 nm (2.5 nm Al_2O_3 and 0.4 nm ZnO), indicating that even for individual layers in the sub-nanometric range (< 0.5 nm), the periodicity of the laminate has been maintained. The deposition rate of ZnO and Al_2O_3 from the calibration laminates were calculated to be 0.003 nm/pulse and 0.002 nm/pulse, respectively.

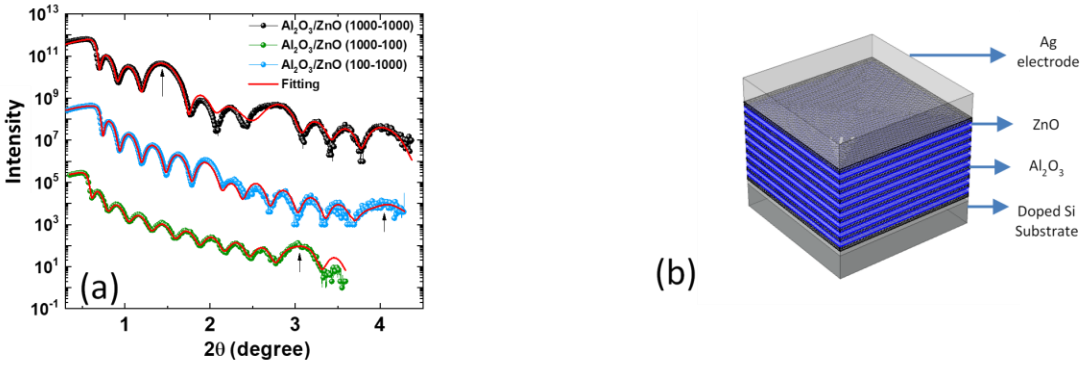

Figure 54 (a) XRR reflectivity curves for calibration samples, the black arrow indicates the position of the Bragg peak related to the bilayer periodicity in each sample. (b) Schematics of the laminate structure of Al_2O_3 and ZnO with top electrode (Ag) and the bottom electrode being the Si substrate

In total, a series of 9 samples were prepared with various individual layer thickness combinations for Al_2O_3 and ZnO, with the same thickness values as in the case of Al_2O_3/Y_2O_3 laminates (Figure 50 (a)). For all laminates, a constant total thickness of 30 nm was maintained by adapting the number of bilayers. Figure 54 (b) shows the schematic representation of the laminate structure.

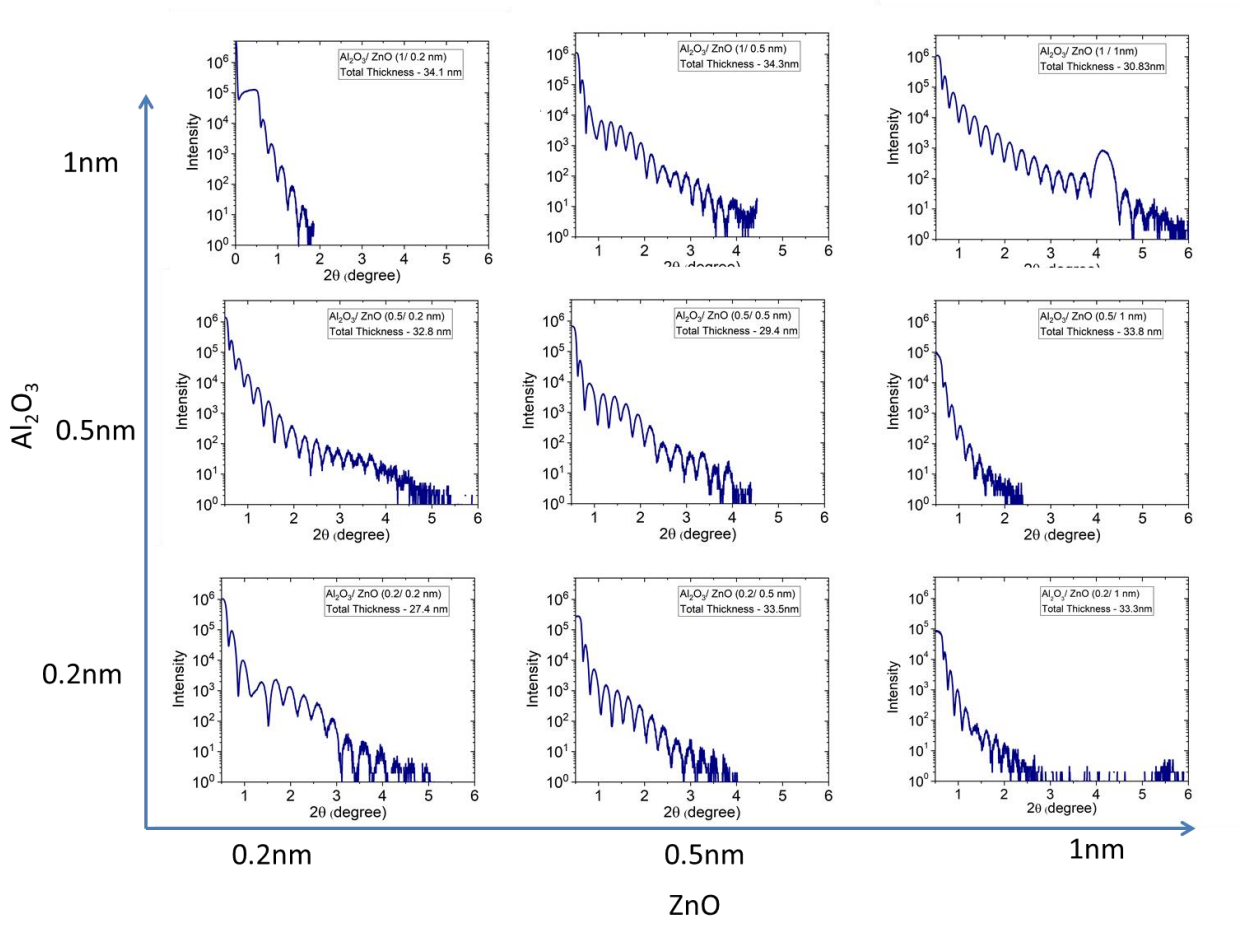

Figure 55 XRR spectra of Al_2O_3/ZnO laminates deposited at 0.005mbar oxygen pressure.

Figure 55 shows the XRR results on the sample series. Again, the data is arranged changing the Al_2O_3 individual layer thickness in the vertical direction and that of the ZnO in the horizontal direction. The XRR analysis of each laminate confirms the good agreement with the experimentally determined deposition rates, and for all laminates, an individual layer thickness with an error of less than 10 % was obtained. For the Al_2O_3/ZnO (1/1 nm) laminate, the presence of the Bragg peak at 4.12° shows the artificial periodicity in the laminate with bilayer thickness of 2nm and total thickness was found to be 30.83 nm. It can be noted, that also in the Al_2O_3/ZnO (0.2/1 nm) laminate, a weak peak can be observed at around 5.5°. Although the peak has a too low intensity to be analyzed further, its presence shows that even for individual layer thicknesses of 0.2 nm, an artificial periodicity is obtained. Therefore, even layers as thin as 0.2 nm layers retain their individual character.

4.2.2. Dielectric properties of laminates grown under standard conditions

For each sample, the apparent dielectric constant and the losses are measured as a function of the frequency (from 10^2 to 10^5 Hz). In Figure 56, the dielectric properties of the Al_2O_3/ZnO laminates for different individual layer thickness configurations (0.2, 0.5 and 1 nm) are drawn.

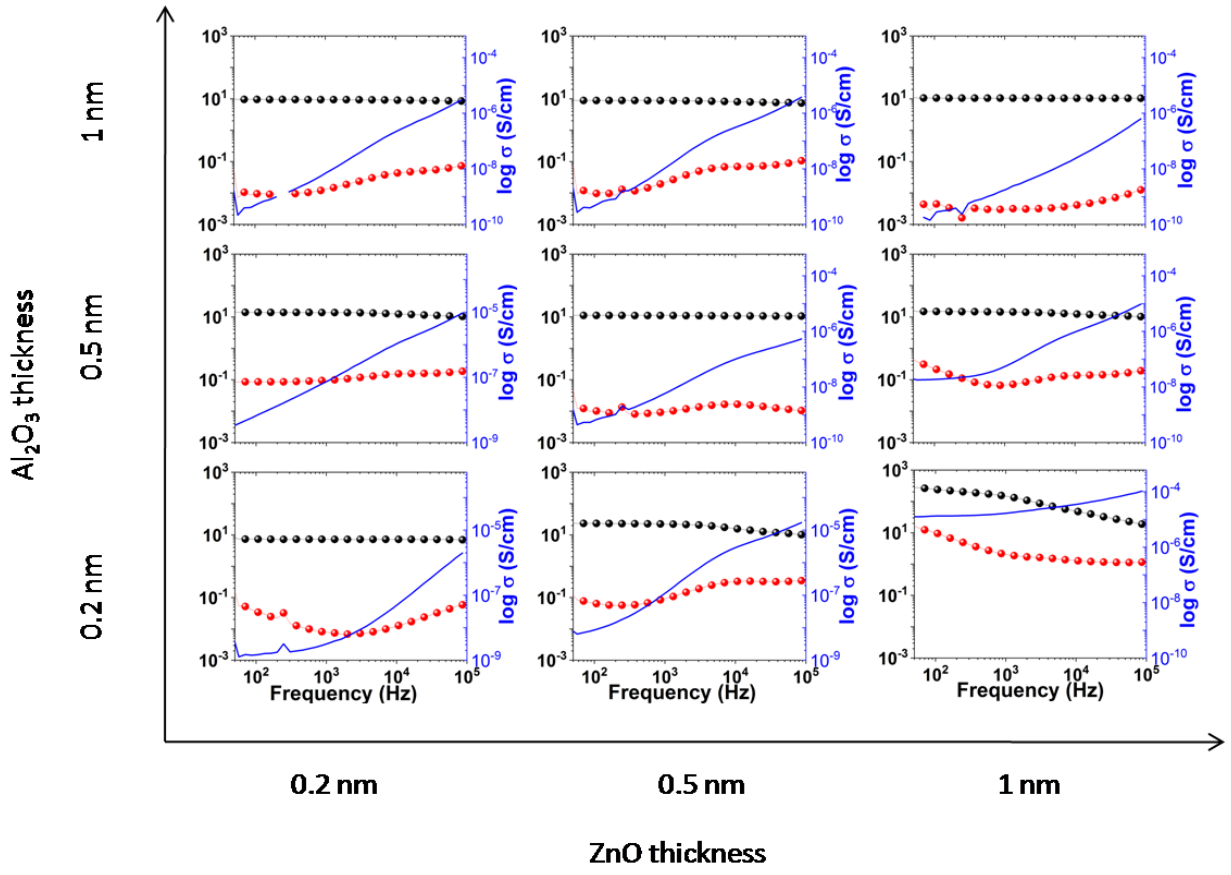

Figure 56 Dielectric properties of Al_2O_3/ZnO laminates with various sublayer thicknesses maintaining the total thickness of 30 nm. In every graph, the black dots represent the dielectric constant and the red dots the dielectric losses (both left y-axis), the blue line shows the ac conductivity (right y-axis).

First, we consider low Al_2O_3 layer thickness. When the thickness of the ZnO layers increases from 0.2 to 1 nm with a constant Al_2O_3 layer thickness of 0.2nm, the dielectric constant of the laminate increases and reaches a maximum value of 211 at 200 Hz in the Al_2O_3/ZnO (0.2/1 nm) configuration. In order to understand the effect involved, the results of these laminates at 200 Hz were compared with the expected dielectric constant of the two models without MW effect (section 2.4.3): (i) the solid solution model of Al_2O_3 and ZnO with the nominal content of ZnO using the relative individual layer thicknesses, and (ii) the series capacitance model. For the

different models, the dielectric constants of Al_2O_3 of 9.8 and ZnO of 110 were determined from the single film dielectric data at 200 Hz (sections 3.1.1 and 3.3.1, respectively). Figure 57 shows the comparison of the experimental data of the laminates with the results of these two models, as a function of the nominal ZnO content, i.e. the ratio of the total thickness of the ZnO individual layers and the total thickness of the laminate. It can be observed that the experimental dielectric constant of the laminates does not follow the solid solution model, confirming the layered structure of all laminates, and especially of the ones with the smallest individual layer thickness, Al_2O_3/ZnO (0.2/0.2 nm). Even for such small values, the layered structure is maintained electrically. For only a small interdiffusion at the interfaces, a dielectric constant corresponding to the solid solution Al_2O_3 – ZnO of 50% would be expected, i.e. 59 (Figure 57).

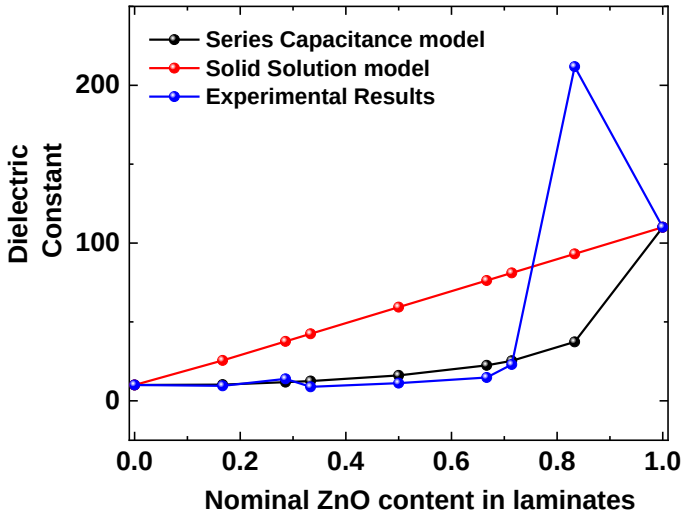

Figure 57 Dielectric constant of Al_2O_3/ZnO laminates as a function of nominal ZnO content, with a comparison of the experimental data with series capacitance and solid solution model at 200Hz

The experimental data follows rather the series capacitance model, except for the Al_2O_3/ZnO (0.2/1 nm). Therefore, the Maxwell-Wagner effect becomes important only for this last laminate, while the other ones behave as expected from the capacitance of the individual layers. For the Al_2O_3/ZnO (0.2/1 nm) laminate, the two models predict a dielectric constant of 93 and 41, respectively, while the experimentally obtained value is 211. This difference indicates the presence of MW effect enhancing the dielectric constant of the laminate. At low frequencies, the

effect is most prominent, with a relaxation peak in the dielectric losses at moderate frequencies. In the higher frequency range (approximately 10^5 Hz), the dielectric constant decreases to a value corresponding to the solid solution of the laminate composition, as expected in the picture of a space charge polarization (section 1.2.3).

When regarding more in detail the series with different ZnO thickness and a constant Al_2O_3 thickness of 0.2 nm, it can be observed that the ac conductivity (blue curves in Figure 56) increases through this series with increasing ZnO thickness. A comparable behavior can be observed also in the ZnO thickness series for an Al_2O_3 thickness of 0.5 nm. This enhancement in the ac conductivity can be understood based on a thickness dependent charge density in ZnO, with a very low charge density for films with a thickness of 0.2 nm and a charge density becoming important enough for a sizeable MW effect at 1 nm. The case of 0.5 nm of ZnO seems to be intermediate, as to be judged from the developing low frequency ac conductivity plateau, but which is not yet established in the measured frequency range.

More generally, in the range of the nominal ZnO content between 0.3 and 0.7 (Figure 57), the laminates show a slightly smaller value of the dielectric constant as predicted from the series model, as for example also the laminate Al_2O_3/ZnO (0.2/0.5nm). Such a decrease of the dielectric constant could be a sign of the break-down of the simple series capacitance model, and therefore the introduction of a third element other than the Al_2O_3 and ZnO layer, i.e. the interface becomes probably electrically active. This would be expected in the case of a MW effect with a low amount of accumulated charges at the interface due to the small ZnO layer thickness. The relaxation frequency of the Al_2O_3/ZnO (0.2/0.5 nm) sample is in the range of 10^4 Hz, which is higher than the relaxation frequency observed in Al_2O_3/ZnO (0.2/1 nm) in the range of 10^3 Hz. This difference in relaxation frequency could be related to the thickness of the ZnO layer, as the distance between the interfaces decreases (given by the ZnO thickness), increasing the relaxation time and decreasing therefore the relaxation frequency [15].

Furthermore, we can observe that, when the thickness of Al_2O_3 increases from 0.2 to 1 and ZnO thickness remains constant at 1 nm, a gradual decrease in the dielectric losses is observed. This behavior indicates that a thicker layer of Al_2O_3 is able to insulate the mobile charges present in ZnO layer. Laminates with Al_2O_3 thickness of 0.5 and 1 nm (for all measured ZnO thicknesses),

show a dielectric constant of about 10. Although the nominal composition of the laminates (i.e. the ratio of the total thickness of the layers of each individual material and the total thickness of the laminate) changes, the apparent dielectric constant stays roughly constant. This is to be expected in the framework of the series capacitance constituted by each individual layer of the laminate (see Figure 57). Due to the relatively low dielectric constant of the Al_2O_3 layer in comparison to that of the ZnO layer, the Al_2O_3 layers with constant thickness govern the series capacitance of the laminate, explaining the experimental observation of a stable laminate dielectric constant.

Moreover, regarding the number of interfaces in the laminates, i.e., the diagonal of Figure 56 (Al_2O_3/ZnO 1/1, 0.5/0.5, 0.2/0.2nm), the apparent dielectric constant stays constant. Thus, we can conclude that MW relaxation is absent at least in the measured frequency range in these laminates, in fact, the apparent dielectric constant being dominated by the Al_2O_3 layers. The losses decrease for thicker individual layers, which can be explained by the increase of the Al_2O_3 layer thickness.

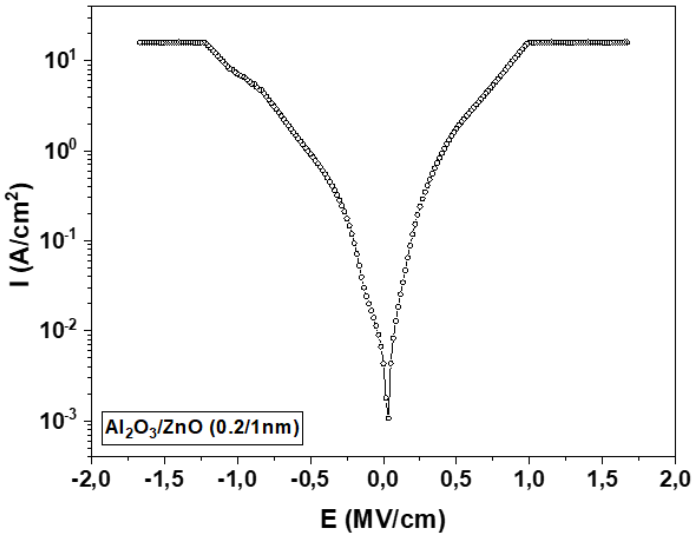

Figure 58 Current-voltage characteristics of an Al_2O_3/ZnO (0.2/1 nm) laminate

We have also measured the current-voltage characteristics of some selected laminates of the series. Figure 58 shows the measurement of an Al_2O_3/ZnO (0.2/1 nm) laminate. The observed leakage current is rather high, due to the relatively poor charge confinement power of the very thin Al_2O_3 individual layers and the high charge density in the ZnO layers. No breakdown was observed, even at higher electric fields,

probably due to the good charge conduction through the laminate. This finding is confirmed also by the high ac conductivity observed in this laminate.

4.2.3. Equivalent circuit analysis of laminates grown under standard conditions

For a better understanding of the influence of each individual layer on the macroscopic dielectric properties, the complex impedance of the equivalent circuit composed of three parallel RC circuits connected in series was simulated. As described in section 2.4.3, one RC circuit for each element of the laminate, the Al_2O_3 layer, the ZnO layer and the interface, was used. By fitting the simulation data to the experimentally obtained data, the values of the resistivity and the dielectric constant of each individual layer are obtained, using the thickness of each constituent from the fitting. In order to get more insight into the changes in the dielectric properties observed for the different laminates, the Al_2O_3/ZnO (0.2/1 nm) and Al_2O_3/ZnO (0.2/0.5 nm) laminates were analyzed further by the full simulations of the experimental results with the model developed in chapter 2. Figure 59 shows the comparison of the experimental data and the simulation results of the dielectric constant and dielectric losses. The comparison of these two laminates is interesting, because the first one shows the Maxwell-Wagner effect, while the second one does not. Table 4 shows the various parameters obtained from the fitting results.

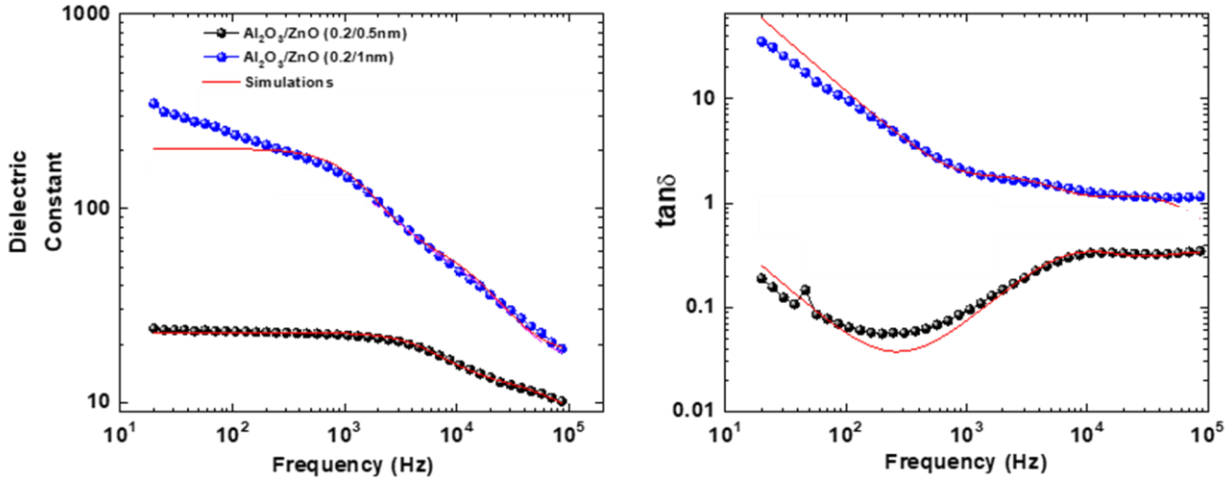

Figure 59 *Dielectric constant and dielectric losses of Al_2O_3/ZnO (0.2/1 nm) and (0.2/0.5 nm) laminates with experimental data and simulation data.*

		Al_2O_3	ZnO	Interface
Al_2O_3/ZnO (0.2/1 nm)	Resistivity Ω - m	1.9 X 10^5	1.5 X 10^4	2.5 X 10^5
	Dielectric Constant	14	14.81	110
	Thickness (nm)	0.17	0.98	0.15
Al_2O_3/ZnO (0.2/0.5 nm)	Resistivity Ω - m	1.06 X 10^9	7.4 X 10^4	1.6 X 10^7
	Dielectric Constant	8.05	12.88	19
	Thickness (nm)	0.18	0.45	0.10

Table 4 Fit parameters (dielectric constant and resistivity of the individual components) of the Al_2O_3 and ZnO individual layers and the interface, for the simulations shown in Figure 59

From the fit results, it is evident that when the thickness of the ZnO layer increases from 0.5 to 1 nm, an abrupt increase in the dielectric constant of the interface is observed, probably due to the accumulation of the charges at this interface from the MW effect. However, the dielectric constant of the ZnO and Al_2O_3 individual layers are similar to their bulk values. The resistivity of the interface and the Al_2O_3 layer reduces for a ZnO thickness of 1 nm, indicating that the thin Al_2O_3 layer is not sufficiently thick to confine the high charge density in 1 nm ZnO. Hence, we observe high dielectric losses in the Al_2O_3/ZnO (0.2/1 nm) laminate. At the same time, the resistivity of the ZnO layer from 0.5 to 1 nm decreases, indicating a higher charge density and a higher mobility of the charges in a 1 nm thick ZnO layer.

The charge density at the interface was calculated by analyzing the capacitance of the interface and the voltage drop at the interface from the equivalent circuit, as detailed in chapter 2. It was found that the charge density at the interface was 1.49x10^{12} and 1.08x10^{12} cm^{-3} at 200 Hz, respectively for the Al_2O_3/ZnO (0.2/1 nm) and Al_2O_3/ZnO (0.2/0.5 nm) laminate. The higher charge density at the interface of Al_2O_3/ZnO (0.2/1 nm) may explain the presence of the MW effect and also the high losses through the laminate structure.

From this analysis, we can identify tentatively the necessary ingredients to obtain a MW effect in the measured frequency range in the sub-nanometric laminates. The charge density of the ZnO seems to be a critical aspect, and a certain thickness seems to be necessary to establish the MW effect in the measured frequency range. Another accompanying effect is the change of the resistance of the different electrically individual constituents. The resistance of the laminate

constituents showing the MW effect are smaller than in the laminate without MW effect for low ZnO thicknesses. This dependence on the ZnO thickness is not easy to be understood and will be discussed in the end of this chapter.

4.2.4. High temperature analysis of laminates grown under standard conditions

In order to gain more insight into the conduction mechanisms and the energetic aspects of the laminates, Al_2O_3/ZnO (0.2/0.5 nm) and Al_2O_3/ZnO (0.2/1 nm) laminates were analyzed as a function of temperature and frequency.

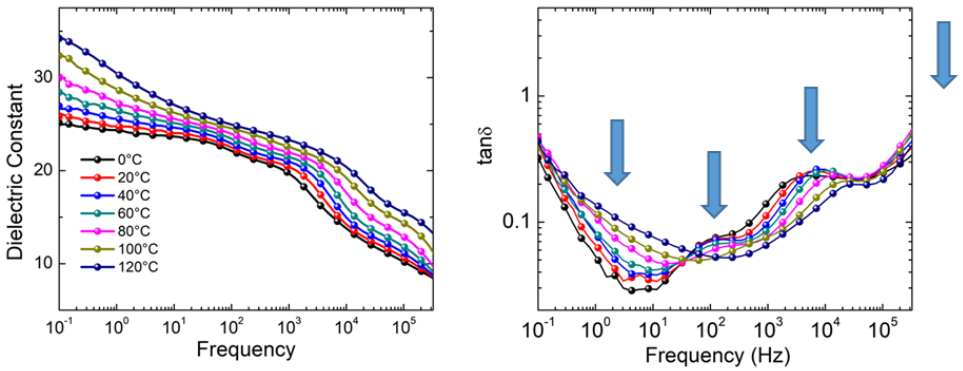

Figure 60 Dielectric constant and tanδ of Al_2O_3/ZnO (0.2/0.5 nm) laminate as a function of frequency and temperature

Al_2O_3/ZnO (0.2/0.5 nm) laminate

Figure 60 shows the temperature dependent dielectric constant and tanδ for the Al_2O_3/ZnO (0.2/0.5 nm) laminate. These measurements were acquired using the Novocontrol BDS 20 at G2Elab in Grenoble. The measured frequency range starts at lower frequencies (0.1 - 10^6 Hz) compared to the measurements shown previously. An up-rise in the dielectric constant is observed with the increase in the temperature throughout the measured frequency range. At low frequencies (< 10 Hz), the rise in the dielectric constant is more pronounced with the temperature. Tanδ of the laminates shows the presence of many relaxations (around 10^0 Hz, 10^2 Hz and 10^4 Hz; another relaxation is probably present out of the measured range, related to the electrode parasitic capacitance), as indicated by the arrows in Figure 60 (b). The relaxation at around 1 Hz is extremely badly defined, and its existence is only visible by the enhancement of the signal at high temperatures, as well as by a related increase of the dielectric constant. Therefore, a simple series capacitance model of this laminate does not hold, as in that case, only

two relaxations related to the individual ZnO and Al_2O_3 layers should be present. Rather, the increase of the dielectric constant at low frequencies and at high temperatures indicates another relaxation, especially with regards to the ac conductivity (Figure 61). The ac conductivity of this laminate is rather small, without the development of a clear dc conductivity plateau at low frequencies. Therefore, the enhancement of the dielectric constant at low frequencies and high temperatures is not related to an enhancement of mobile charge carriers, but probably rather to the presence of a MW effect at a frequency below the measured frequency range.

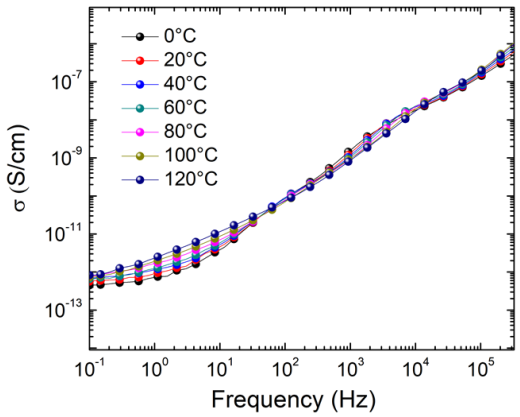

Figure 61 ac conductivity of Al_2O_3/ZnO (0.2/0.5 nm) laminate

In order to better understand the relaxations in the laminate, the complex electric modulus was calculated as explained in equation (25) in section 2.4.1. The imaginary component of the electric modulus can be expressed in terms of the dielectric constant (k) and tanδ as:

$$M'' = \frac{tan\,\delta}{k(1 + tan\,\delta)} \qquad (31)$$

Due to the presence of k and tanδ in the denominator of equation (31), M'' allows a more comprehensive analysis of the electrical relaxation processes in samples where tanδ is high. However, in case of Al_2O_3/ZnO (0.2/0.5 nm) laminate, tanδ is less than 1 hence the relaxations observed in tanδ and M'' are similar, which also indicates the low mobility of free charges. Similar to what is observed in tanδ, three relaxations are visible in the measured frequency range, and another one is present above the measured frequency range. It is probably related to the MW effect being present at lower frequencies, out of the measured frequency range. Again, the

relaxation present at a frequency higher than 10^6 Hz, could be an instrumental effect arising due to the parasitic impedance. The two other relaxations, indicated by RI and RII in Figure 62, are present at 10^2 and 10^4 Hz, respectively. These relaxations are well defined, and their temperature shift can be used to determine the temperature dependence of the respective relaxation. From the simulation results (Table 4), based on the resistance and capacitance values obtained for ZnO layer and Al_2O_3 layer, it can be deduced that the RI peak is related to the Al_2O_3 layers while RII is related to the ZnO layers.

Activation energies for each relaxation were calculated from the temperature dependent frequency of the maximum of their respective peaks in M'' (Figure 62 (b)). The activation energy related to the individual ZnO layers (RII) is found to be 0.13 eV and for the Al_2O_3 layers, it was found to be 0.09 eV. Such low activation energies indicate that the electrons are the major polarization charges in the laminates. Comparable activation energies in Al_2O_3/ZnO laminates have been also observed by Jin Li et.al. [110]. However, the activation energies related to ZnO layer (RII) are smaller than the values estimated by Anderson, Janotti et.al. [111], which could be due to the changes in bandgap of thin and amorphous ZnO, leading to the changes in the Fermi level in laminates. The activation energies related to the Al_2O_3 layer (RI) are similar to the activation energies observed in the single films of Al_2O_3 (as shown in chapter 3). Such a similarity is remarkable seen the extremely low thickness of the Al_2O_3 layers in the laminates.

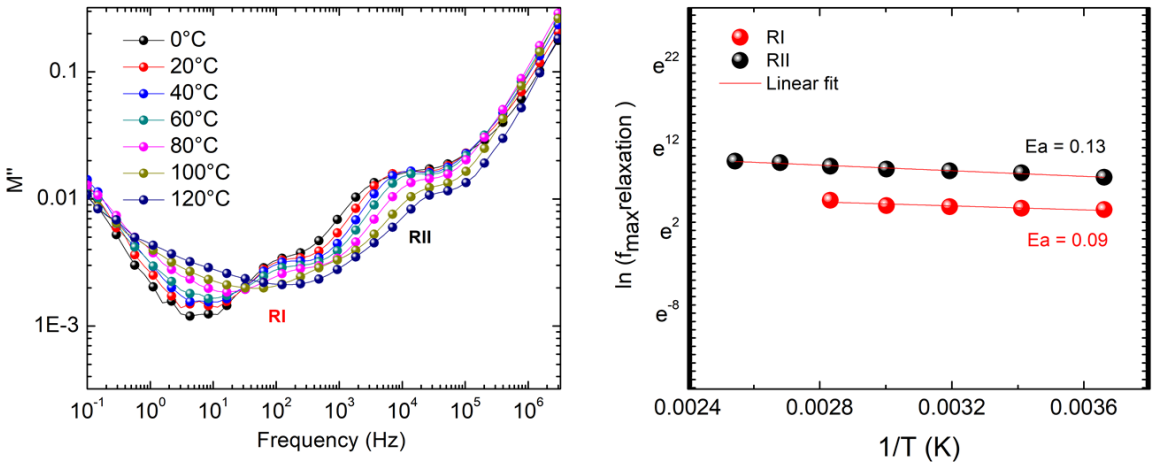

Figure 62 M'' and the activation energies of various relaxations present in Al_2O_3/ZnO (0.2 / 0.5 nm) laminate.

Al_2O_3/ZnO (0.2/1 nm) laminate

Similar to the Al_2O_3/ZnO (0.2/0.5 nm), the Al_2O_3/ZnO (0.2/1 nm) laminate was also analyzed with high temperature impedance spectroscopy. The initial measurements were not successful due to a contact problem with the probe, but by an annealing of the sample at 200°C under nitrogen atmosphere, the electrical contact was established. As the temperature may have some influence on the structure of the laminates (crystallization of ZnO, for example), the following data has to be taken with care. However, the observed properties seem to be consistent with the initially observed MW effect, so we will analyze them here.

An important up-rise in the dielectric constant is observed with the increase in the temperature at low frequency range. The forming plateau could be related to the polarization developed due to the accumulated charges at the interface of Al_2O_3 and ZnO and shows the presence of the MW effect in the Al_2O_3/ZnO laminate. Unlike for the Al_2O_3/ZnO (0.2/0.5 nm), the low frequency tanδ is also increasing with the temperature, indicating that the laminate is less resistive, so the charges are participating in polarization as well as in the conduction, as the temperature increases. Only one relaxation peak is clearly visible in tanδ at around 10^4 Hz and it moves towards higher frequencies as the temperature increases. Another relaxation can be vaguely discerned between 10^2 and 10^3 Hz, but is not clearly visible due to the high conduction of free charges at low frequency.

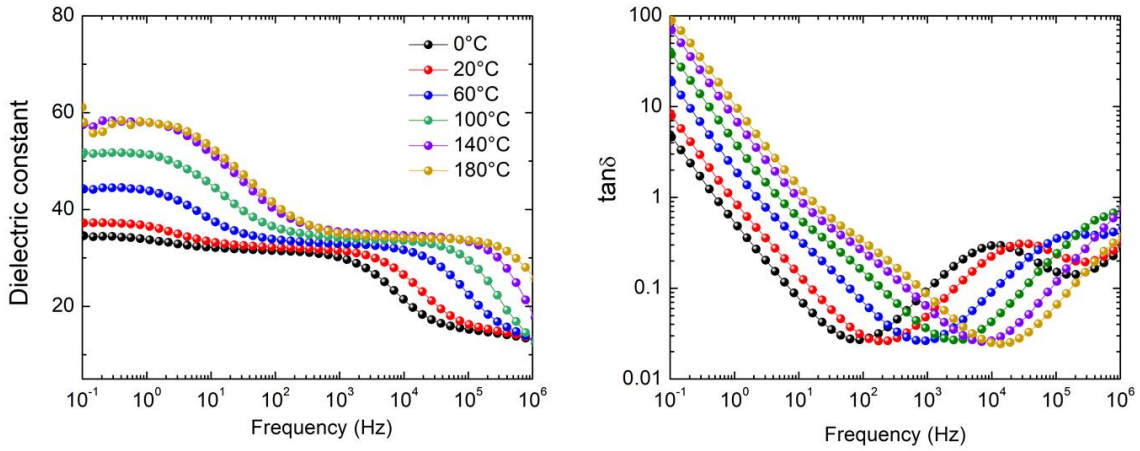

Figure 63 Dielectric constant and tanδ of Al_2O_3/ZnO (0.2/0.5 nm) laminate as a function of frequency and temperature

As discussed earlier, M'' gives a more comprehensive description of the relaxation processes for large tanδ. The relaxation peaks, which were hidden in the tanδ curve, can be clearly observed in M'' (Figure 64). At room temperature, two symmetric relaxation peaks are visible (RI and RII). However, as the temperature increases, the RI peak becomes asymmetric. This asymmetric shape is a result of the superposition of two peaks at room temperature, with different temperature dependencies of the peak position. Taking into account the fit parameters of the room temperature dielectric properties of the Al_2O_3/ZnO (0.2/1 nm) laminate (Table 4), the peak related to the interface and the Al_2O_3 layers confound due to the very similar resistivity. As the M" peak position is governed by the resistance of the related component of the laminate, this also explains the development of the MW effect in the measured frequency range.

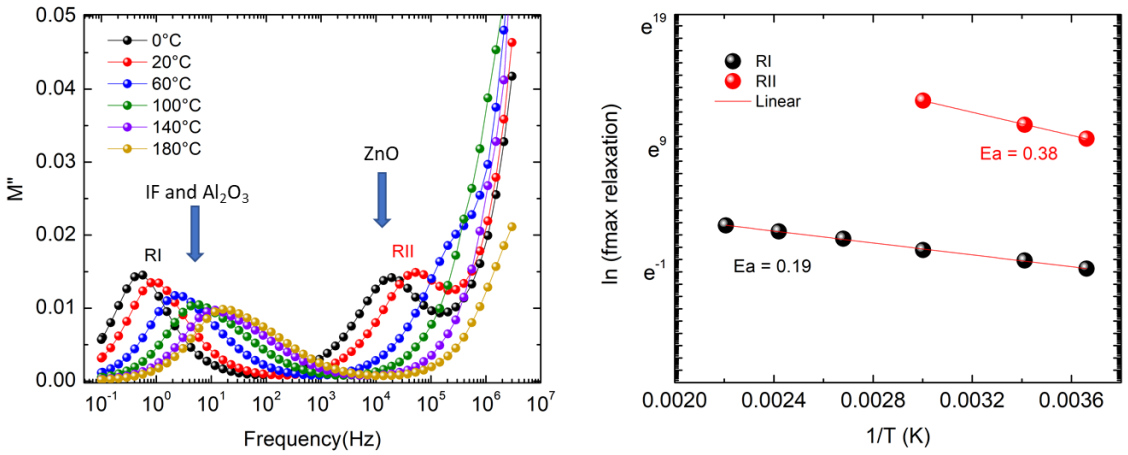

Figure 64 M" of Al_2O_3/ZnO (0.2/1 nm) and the determination of the activation energy from the RI and RII peak positions

The asymmetric shape of the RI peak at high temperature can then be interpreted to be constituted of the Al_2O_3 peak and the interface peak at slightly higher frequency. This attribution is principally based on the higher dielectric constant of the interface component, leading to a smaller M" peak amplitude. RII can again be attributed to the ZnO layers. The calculated activation energies from RI and RII peaks shows higher values as compared to Al_2O_3/ZnO (0.2/0.5 nm) laminate, but unfortunately these values cannot be compared directly because of the additional annealing step used for the creation of the electrical contact. The high frequency shoulder of the RI peak related to the interface component was not analyzed due to the badly

defined peak shape. However, the different temperature evolution indicates a slightly higher activation energy.

Figure 65 shows the ac conductivity of Al_2O_3/ZnO (0.2/1 nm) as a function of temperature and frequency. A low frequency and temperature dependent plateau are observed in ac conductivity at all measured temperatures, which is related to the dc conduction through the laminate. High dc conduction through Al_2O_3/ZnO (0.2/1 nm) laminate is related to the low interface resistance and high mobile charge density in ZnO layer, as determined in the previous sub-chapter. The activation energy calculated from the conductivity value of the dc plateau is comparable to the activation energy determined by the RI peak position, about 0.2 eV. This coincidence of the temperature dependence clearly indicates that the Al_2O_3 layer is the limiting component of the dc conduction in the laminate.

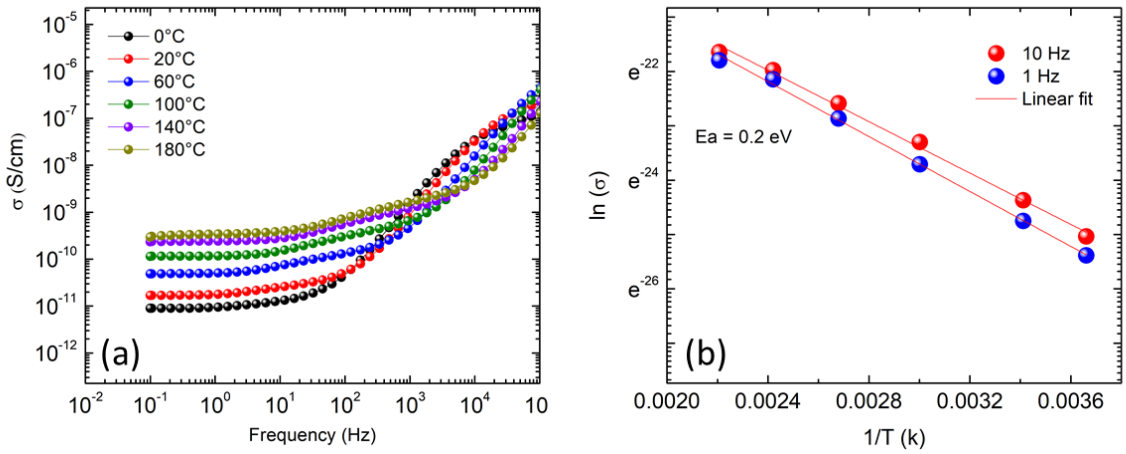

Figure 65 ac conductivity Al_2O_3/ZnO (0.2/1 nm) laminate and the calculated activation energies at 1 and 10Hz

4.2.5. Effect of deposition pressure

As observed in the previous section that the dielectric properties of the sub-nanometric laminates are dependent on the thickness the individual layer thicknesses of the constituents. The change in resistive nature of the interface with the individual layer thickness was affecting the MW effect in the laminates. The dielectric properties of ZnO single films showed a high dependence on the deposition pressure (section 3.3.2), as the density of oxygen vacancies in ZnO

layer increases when deposited under low oxygen pressure. To understand the effect of the deposition pressure on Al_2O_3/ZnO laminates, a series of 9 samples were prepared at vacuum (no oxygen inserted in chamber) and 0.05 mbar, with the same individual layer thicknesses as for the 0.005 mbar pressure series. All the other deposition parameters were kept the same. The following section shows the structural and the dielectric behavior of Al_2O_3/ZnO laminates deposited at vacuum and 0.05 mbar oxygen pressure.

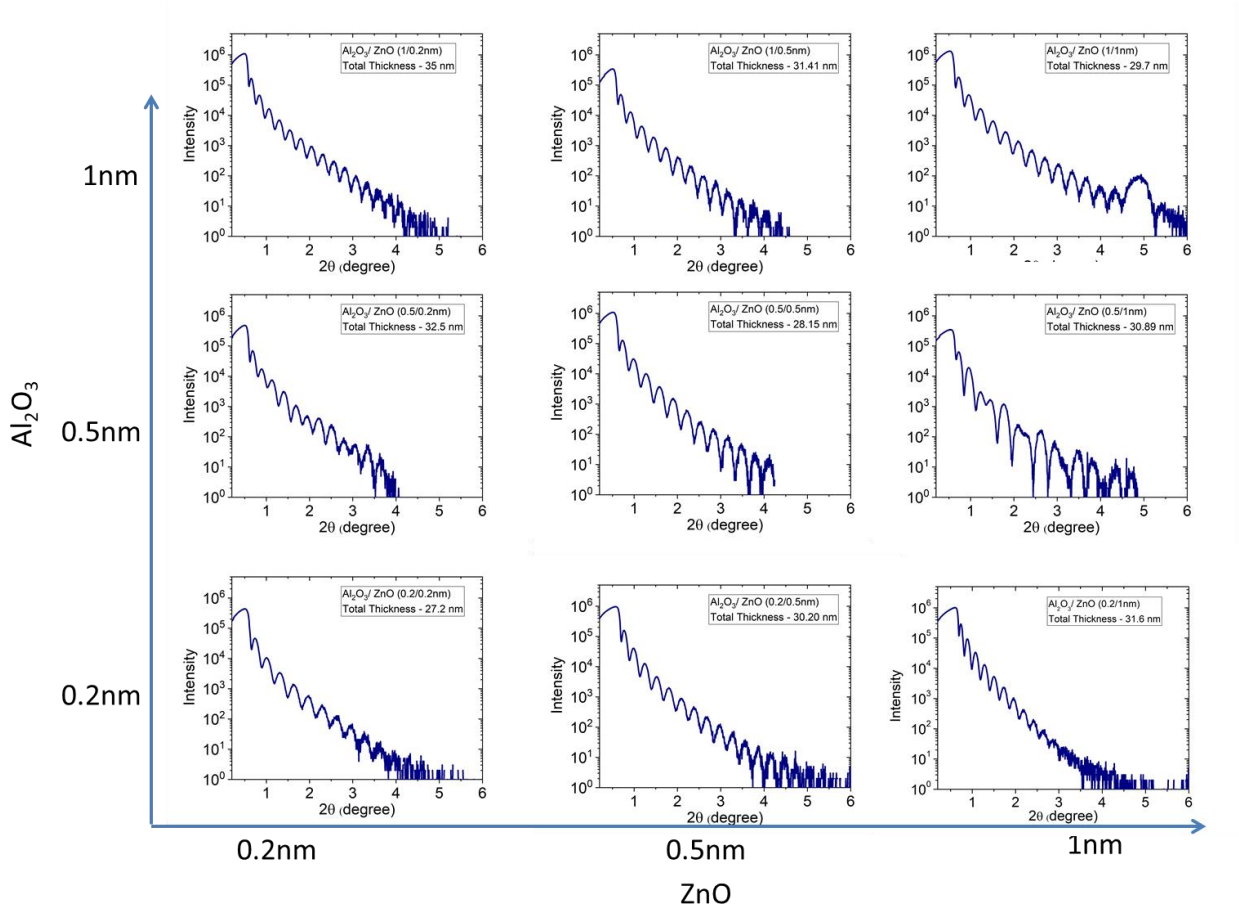

Figure 66 XRR spectra of the Al_2O_3/ZnO laminates deposited under vacuum.

Al_2O_3/ZnO laminates deposited at vacuum

In chapter 3, a detailed analysis of single films deposited at different oxygen pressures has been presented. For Al_2O_3, the vacuum deposited single films showed similar behavior as the films deposited at 0.005 mbar (Figure 31 in section 3.1.2). However, the ZnO film deposited at vacuum was found to have oxygen sub-stoichiometry and a high conductivity was observed. Therefore, the laminates deposited at vacuum are expected to have a high mobile charge density

in ZnO layer, with an accumulation of these charges at the Al_2O_3 – ZnO interface. Figure 66 shows the XRR spectra of the laminates deposited under vacuum. The total thickness of all laminates is in the range of 30 nm (± 10 %). The slope of the XRR spectra suggests that the laminates deposited at vacuum have a lower roughness as compared to the laminates deposited at 0.005 mbar. The bilayer peak in Al_2O_3/ZnO (1/1 nm) showed again a bilayer periodicity in the laminates.

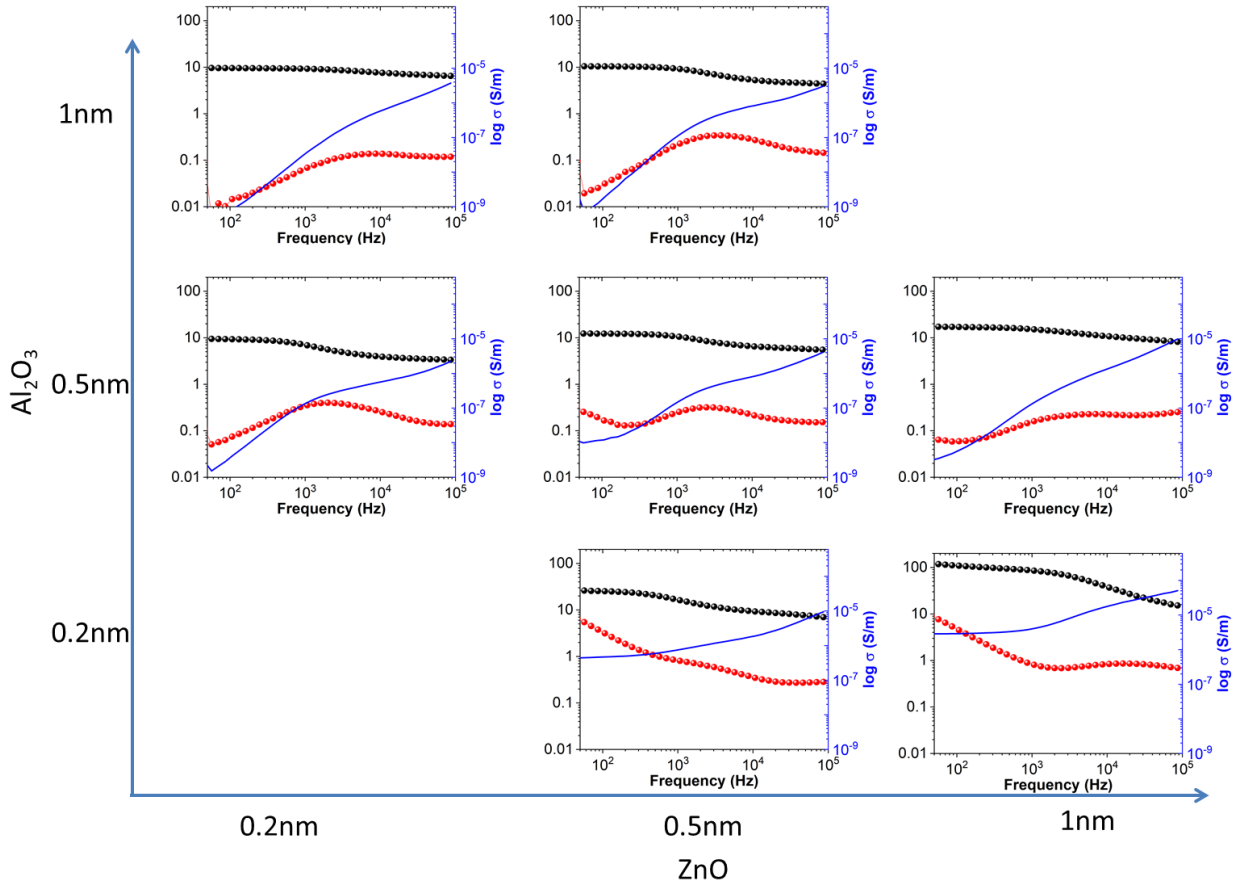

Figure 67 Dielectric properties of Al_2O_3/ZnO laminates deposited under vacuum. In every graph, the black dots represent the dielectric constant and the red dots the dielectric losses (both left y-axis), the blue line shows the ac conductivity (right y-axis).

The dielectric properties of the samples deposited at vacuum are similar as in the case of the 0.005 mbar sample series. The dielectric results of laminates with the configurations (1/1 nm) and (0.2/0.2 nm) could not be measured accurately, because of silver paste sticking to the electrodes, but based on the behavior of the other laminates, it is clear that these laminates

would have behaved similar to the laminates in the 0.005 mbar series. Figure 67 shows the dielectric properties of laminates as a function of frequency and individual layer thickness.

As discussed before, it was expected that the laminates deposited under vacuum would have a high mobile charge density in the ZnO layer to be accumulated at the internal interfaces of the laminate. However, such an effect is not observed. This behavior could be due to an oxygen exchange between the Al_2O_3 layers and the ZnO layer. Generally, Al_2O_3 is considered as an extremely stable oxide in crystalline form when the Al atoms are coordinated with 6 oxygen atoms. However, in this case, Al_2O_3 is amorphous with a thickness in the sub-nanometric range, so the possibility of oxygen exchange cannot be denied, especially with the vicinity of a strongly under-oxidized ZnO. With such an oxygen exchange, the ZnO layer would be slightly less oxygen-deficient in the laminate, explaining the apparently similar behavior to the 0.005 mbar series. For an individual layer thickness of Al_2O_3 of 0.5 and 1 nm, for all ZnO thicknesses, the dielectric properties of laminates are dominated by the Al_2O_3 and low losses are observed, similar to the laminates deposited at 0.005 mbar. When the thickness of Al_2O_3 is 0.2 nm, a rise in the dielectric constant is observed and for Al_2O_3/ZnO (0.2/1 nm) a dielectric constant of 101 was obtained at 200Hz. This rise in the dielectric constant is due to the presence of MW effect at the interface.

Al_2O_3/ZnO laminates deposited at 0.05 mbar

The laminates of Al_2O_3 /ZnO deposited at 0.05 mbar showed growth rate instabilities, and the total thickness of the laminates were not matching well with the calculated thicknesses from the calibrated deposition rates. At 0.05 mbar, single films of ZnO showed a low deposition rate with high roughness (Figure 47 in section 3.2.2), which causes the error in the calibration of the deposition rates. Here we are presenting only the data of the laminates, which have comparable thicknesses to the 0.005 mbar and vacuum series. Figure 68 shows the dielectric properties of the laminates with the individual thickness of (0.2/0.35 nm), (0.16/1.1 nm) and (0.53/1 nm). When the thickness of ZnO layer increases, the dielectric constant remains the same, but the tanδ has increased (comparing Al_2O_3/ZnO (0.2/0.35nm) and (0.16/1.1 nm)), as the ZnO layer deposited at 0.05mbar has a small defect density and the thickness of ZnO does not affect the accumulation of charges at the interface. However, when the content of Al_2O_3 increases in the

laminate, the decrease in the dielectric constant and losses can be observed as shown in Al_2O_3/ZnO (0.53/1 nm).

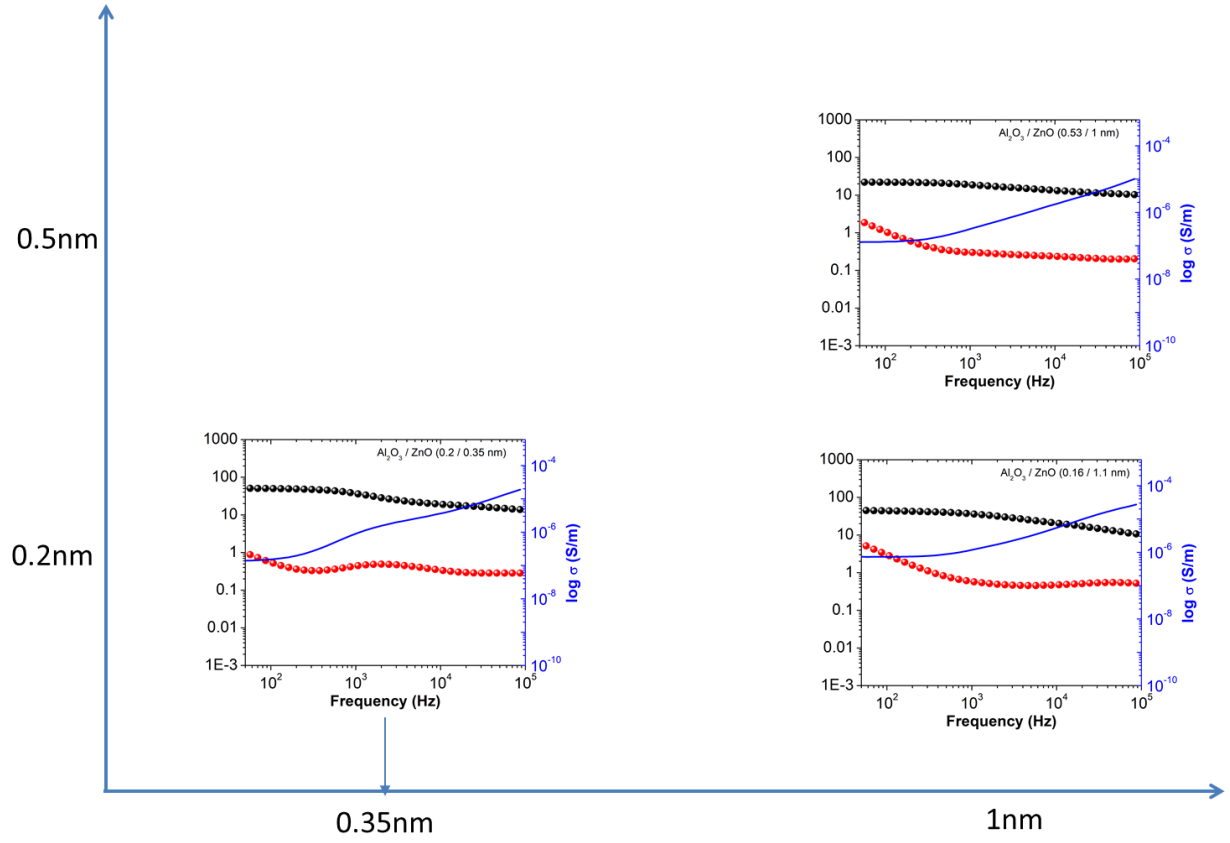

Figure 68 Dielectric properties of Al_2O_3/ZnO laminates deposited at 0.05mbar pressure (x axis represent the thickness of ZnO layer and y axis represent thickness of Al_2O_3 (nm)

Comparison of the Al_2O_3/ZnO (0.2/1 nm) laminate under different deposition pressures

From the data presented before, it has been observed that the MW effect was more pronounced, when the individual layer thickness of Al_2O_3 and ZnO are 0.2 and 1 nm, respectively. Here, a comparative study of Al_2O_3/ZnO (0.2/1 nm) laminates deposited at different deposition pressures is presented. Figure 69 shows the XRR spectra of Al_2O_3/ZnO (0.2/1 nm) laminates deposited at different deposition pressures. The XRR intensity reduces to zero, as 2θ increases above 4° for the vacuum and the 0.05 mbar samples, and 2.5° in the 0.005 mbar sample. The Bragg peak related to 1.2 nm bilayer thickness was expected to arise at 7.35°, but could not be observed due to this strong intensity decrease. The slope of the XRR spectra is related to the

roughness and it was observed that the laminate deposited at vacuum had a lower roughness as compared to the laminates deposited at 0.005 and 0.05 mbar. The thickness of the laminates was found to be 31.6nm, 33.3 nm and 24.9 nm for vacuum, 0.005mbar and 0.05 mbar respectively. The 0.05 mbar laminate has a lower thickness than expected because of the unstable growth rate, and the number of bilayers (30) in this laminate are different as compared to the laminates deposited at vacuum and 0.005 mbar (25).

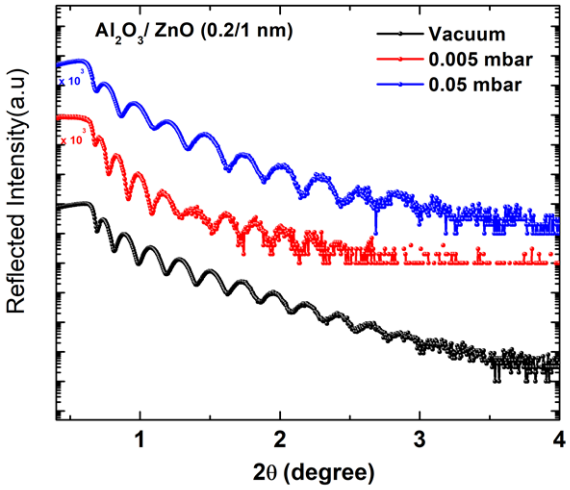

Figure 69 XRR spectra of Al_2O_3/ZnO (0.2/1 nm) laminates deposited at different oxygen pressure.

Figure 70 shows the dielectric constant and tanδ of the laminates as a function of the deposition pressure and the frequency. At low frequency, the enhancement of the dielectric constant is related to the MW effect in the laminates, however the effect is more apparent in the laminates deposited at 0.005 mbar as compared to the vacuum and 0.05 mbar. The laminate deposited at 0.05 mbar has the smallest dielectric constant with comparatively low losses, which was expected, as the single film of ZnO deposited at 0.05 mbar pressure has a low oxygen vacancy density and hence a lower charge density. Therefore, fewer charges are accumulated at the interface, and the low polarization leads to a smaller dielectric constant, though the MW effect is still present. The dielectric constant of the laminate deposited at 0.005mbar is the highest of the three laminates, and the losses are also slightly higher. Therefore, the change of the deposition pressure seems to have a stronger influence on the ZnO individual layers, where the mobile charge density increases for low pressures, than on the Al_2O_3 layers.

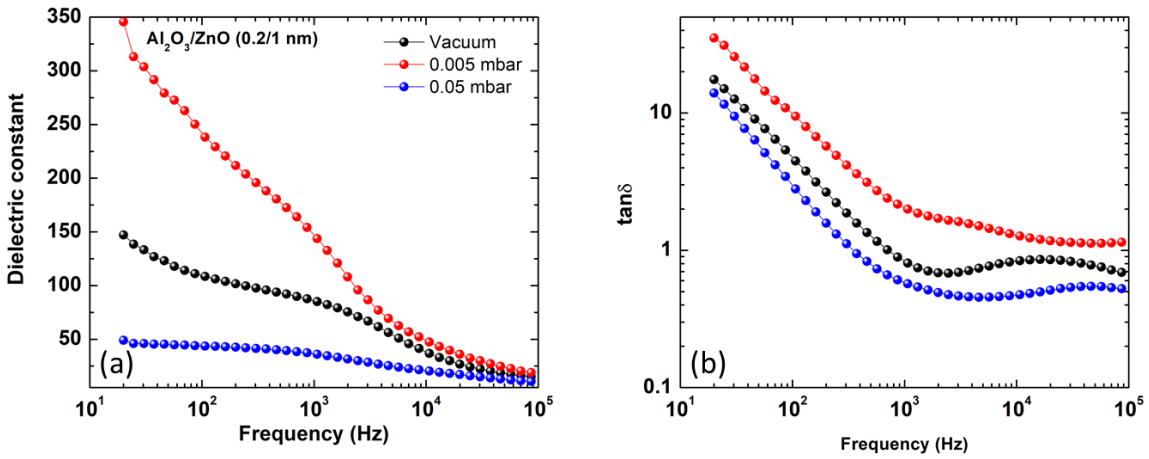

Figure 70 Dielectric constant and tanδ of Al_2O_3/ ZnO (.2/1 nm)

For further understanding, the equivalent circuit analysis was conducted for the laminates deposited at vacuum and 0.005 mbar, in order to fit the experimental data with the mathematical model, as explained in section 2.4.3. The resistivity, dielectric constant and the thickness of the individual layers as well as for the interface were determined (Table 5).

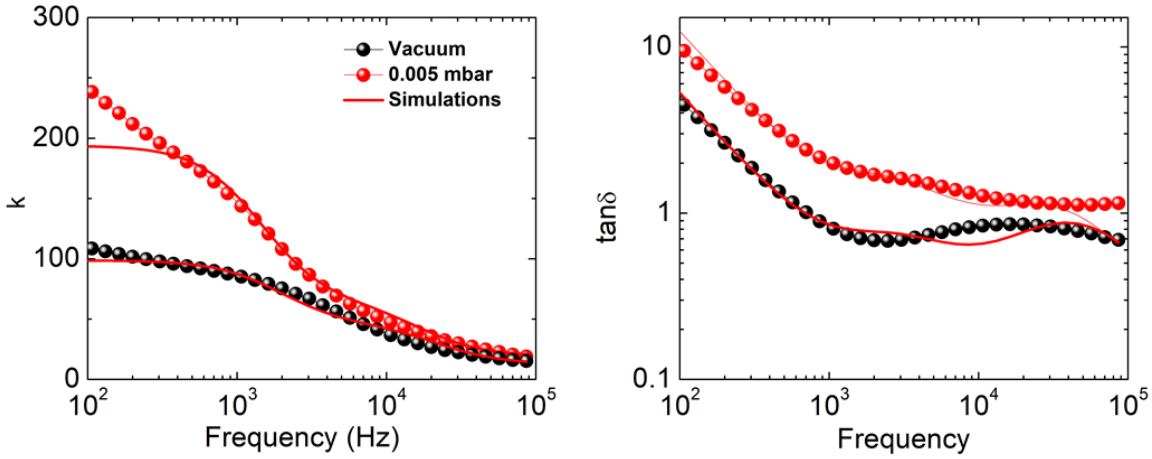

Figure 71 Simulation and experimental data for the laminates deposited at 0.005mbar and at vacuum

The thickness of the individual layers fitted well with the experimental values. The resistivity of ZnO layer was found to be unchanged with the deposition pressure, which ensures that some oxygen exchange has happened in case of the vacuum deposited films. However, the dielectric constant slightly enhances for the 0.005 mbar laminate, indicating that the origin of the stronger

MW effect is related to an enhanced charge density. The resistivity of the Al_2O_3 layer increases somewhat in the case of 0.005 mbar, while the resistivity of the interface layer remains similar in both cases. Thus, the change of the macroscopic properties is related to only small changes in the constituent characteristics, underlining the importance of a high level of control of the growth process to attain reproducible properties, but also the difficulty to predict the MW effect in complex systems as sub-nanometric laminates.

		Al_2O_3	ZnO	Interface
Al_2O_3/ZnO (0.2/1 nm) Deposited at 0.005 mbar	Resistivity Ω - m	1.9×10^5	1.5×10^4	2.5×10^5
	Dielectric Constant	14	14.81	110
	Thickness (nm)	0.17	0.98	0.15
Al_2O_3/ZnO (0.2/1 nm) Deposited at vacuum	Resistivity Ω - m	3.5×10^6	1.5×10^4	9.3×10^4
	Dielectric Constant	11.41	9.68	29.96
	Thickness (nm)	0.12	0.90	0.25

Table 5 Simulated data for individual layers in Al_2O_3/ZnO laminate deposited at vacuum and at 0.005mbar pressure

4.3. Y_2O_3/ZnO laminates

As explained in section 1.4.2, Y_2O_3 is a potential material to be used in high-k laminates on Si because of its high dielectric constant, good thermodynamic stability with Si and a high conduction band offset with Si. A Study by J. Kwo et al has shown that an intermediate layer of Y_2O_3 between the Si substrate and a ZnO film has shown good insulation properties and also restricts the formation of a SiO_2 layer at the surface of the substrat, as the heat of formation of Y_2O_3 is less than that of SiO_2 [112]. The laminates of Y_2O_3 and ZnO have not been explored extensively so far, in this dissertation we explored the possibility of replacing Al_2O_3 to enhance the MW effect at the interface of insulator and the ZnO layer.

4.3.1. Structural properties

After calibrating the deposition rates as explained in chapter 2, the deposition rates were found to be 0.0016 nm/pulse and 0.005 nm/pulse, respectively, for Y_2O_3 and ZnO. Based on these deposition rates, it has been observed that the nucleation of ZnO on a Y_2O_3 layer is easier than

on an Al_2O_3 layer. The sub-nanometric laminates of Y_2O_3 and ZnO were prepared with a total thickness of 30 nm ± 10%. Figure 72 shows the XRR spectra of Y_2O_3/ZnO laminates, in the same way than in the other sections of this chapter. The Y_2O_3/ZnO (1/1 nm) laminate shows again the bilayer periodicity. The slopes of spectra of all the laminates are similar, which indicates that the roughness of the films is in the same range.

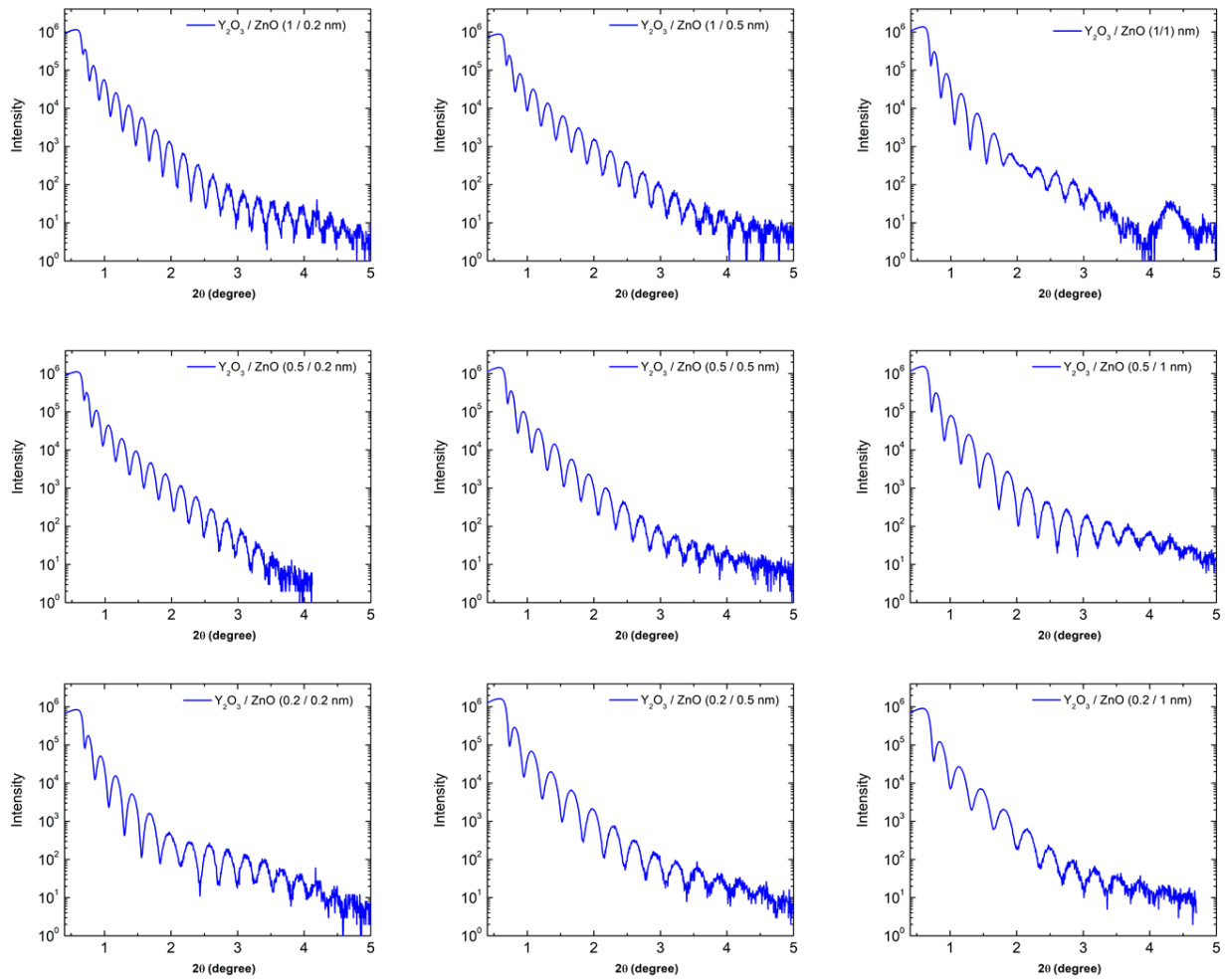

Figure 72 XRR spectra of Y_2O_3/ZnO laminates

For each sample, the dielectric constant and the losses are measured as a function of the frequency in the range of 10^2 to 10^5 Hz. In Figure 73, the dielectric properties of the Y_2O_3/ZnO laminates for different individual layer thickness configurations (0.2, 0.5 and 1 nm) are drawn. The dielectric constant for all the laminates was found in the range of 11 to 15 while the tanδ

was found between 0.001 and 0.2 in the measured frequency range. These laminates did not show any trace of MW effect unlike Al_2O_3/ZnO laminates.

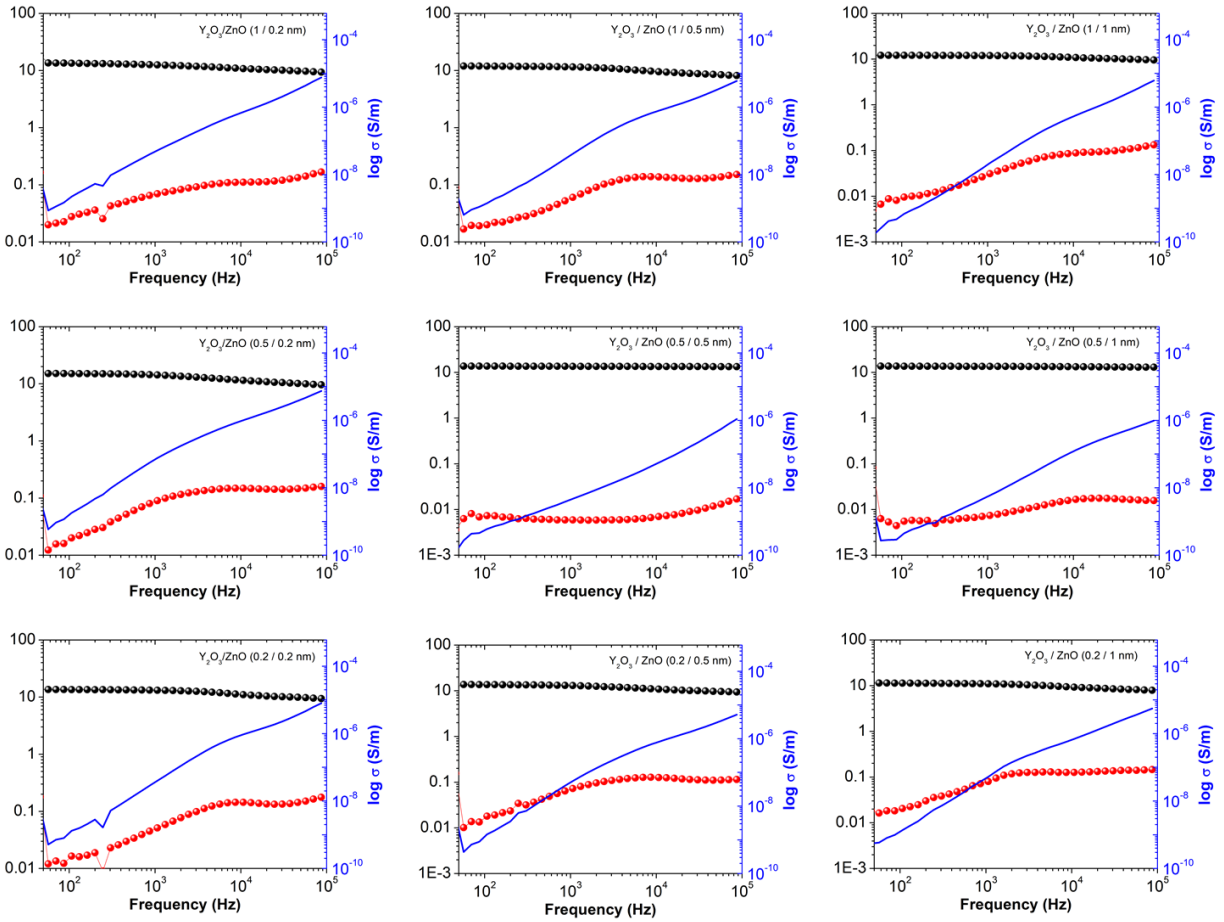

Figure 73 Dielectric properties of Y_2O_3/ZnO laminates

The single films of Y_2O_3 and ZnO deposited at the same deposition conditions showed dielectric constants of 12.5 and 110, respectively, at 200 Hz (sections 3.2.1 and 3.3.1). However, the laminate dielectric properties were found to be dominated by the Y_2O_3 layer, even when the thickness of Y_2O_3 layer is only 0.2 nm in the laminate. This indicates that the mobile charge density in the ZnO layers inter-grown with the Y_2O_3 layers has been reduced, which is probably due to chemical changes. The majority mobile charges in the ZnO layer have been affected by the presence of the Y_2O_3, an oxygen exchange could be possibly kill the introduction of charges to accumulate at the interface of the Y_2O_3 and ZnO.

4.4. Important effects in laminates

Based on the analysis of all laminates of Al_2O_3/ZnO, Y_2O_3/ZnO and Al_2O_3/Y_2O_3, it has become clear that in order to obtain a substantial MW effect in the laminates, a sufficient charge density in the semiconductor layer (ZnO) is required to accumulate at the interface. In the case of Al_2O_3/Y_2O_3 and Y_2O_3/ZnO, the absence of the MW effect can be understood with the absence of the mobile charges in ZnO layer. Also, we can conclude that the interface plays a critical role in defining the MW effect in the laminates. The resistance and capacitance of the interface affects the dielectric properties in laminates, which can be a tuned based on the thickness of each layer and the deposition pressure. Two important effects taking place in the laminates are pointed out by the here realized study:

(i) Growth effect

The growth of sub-nanometric laminates is very tricky, as the interface becomes an important part of the laminates, regarding its volume. The equivalent circuit simulations have shown an electrical interface thickness of around 0.2 nm, which is also the minimal value taking into account the perturbation of one atomic layer at each side of the interface. Depending on the individual layer thicknesses in the laminate, this value corresponds to about 20% to 50% of the total laminate volume. These interfaces also introduce electrical perturbations, due to the vicinity of different elements. The electrically rough interfaces may add up extra energy states in the band gap and will reduce the conduction band offset of the insulator and semiconductor layer, leading to a MW effect with high losses. However, a less rough interface will have a high resistance, which will limit the working frequency to very low values.

(ii) Chemical effect

The electrical properties of ZnO are highly dependent on its defect density. A high defect density (oxygen vacancies majorly) will ensure a high mobile charge concentration to accumulate at the interface. But it seems that the oxygen exchange between the insulator and semiconductor layer in sub-nanometric laminates reduces the mobile charges to accumulate at the interface. Such an oxygen exchange effect is extremely hard to control, even for a material reputed to be extremely

stable concerning the oxygen exchange, as Al_2O_3, this effect cannot be avoided, probably due to the high number of interfaces in the laminates.

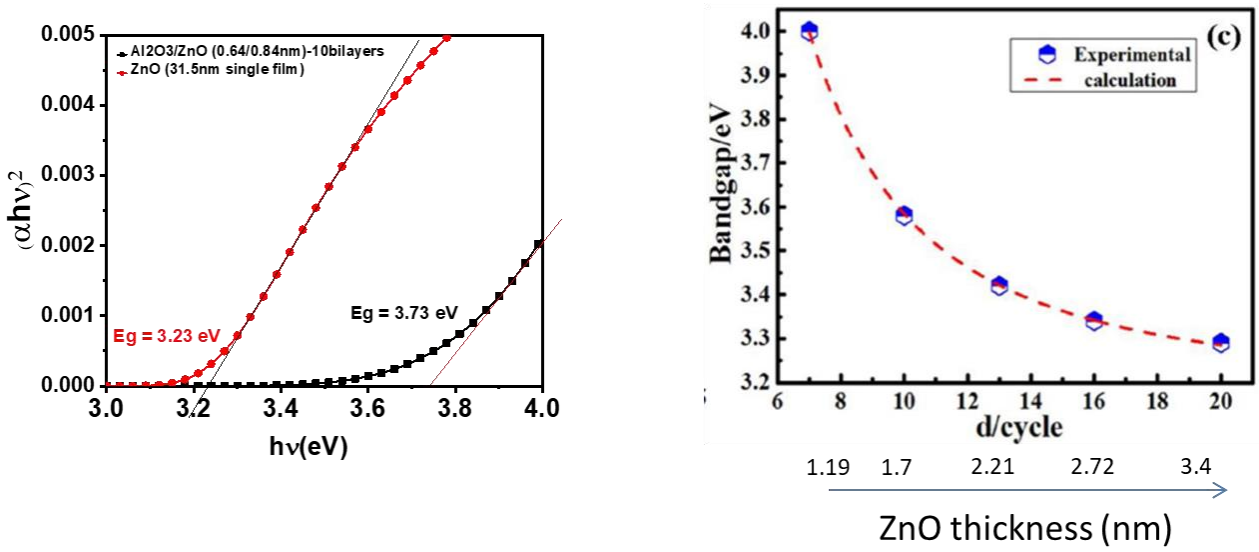

Figure 74 Measurements of the band gap in an Al_2O_3/ZnO (0.64/0.84 nm) laminate and a 31.5 nm thick ZnO single film. On the right side, the variation of the band gap of ZnO in Al_2O_3/ZnO nanolaminates are shown, reproduced from [113]

Another effect may also play a role, which is the band gap size of the ZnO in the laminate. In Al_2O_3/ZnO nanolaminates, it was observed that the ZnO bad gap undergoes a substantial change [113]. In nanometric ZnO films, the band gap was found to be in the range of 3.2 eV [113] . In laminates with an individual layer thickness of the ZnO of some nanometer, the band gap has a size of about 3.2 eV. This value increases to about 4 eV in layers of about 1 nm (Figure 74). We were not able to conduct a full study on the band gap of the ZnO in the subnanometric laminates shown in this chapter, but thanks to the collaboration with J. Cardin and Ch. Labbé from the CIMAP (Caen), it was possible to make some test measurements. These results, obtained by optical measurements on an Al_2O_3/ZnO (0.64/0.84 nm) laminate and a ZnO single film, have shown a similar effect in our laminates. While the band gap in the single film is about 3.2 eV wide, the one in the laminate is about 3.7 eV. It is complicated to estimate the effects of such a band gap change on the macroscopic dielectric properties, especially as the Al_2O_3 band gap of the sub-nanometric individual layers may change strongly compared to the bulk values. Also, the band alignment in the laminates is difficult to apprehend. However, such a band gap change will

change the depth of the potential well of the accumulated charges at the interface, and therefore probably the MW effect. A more systematic study of this effect was conducted on a sample series with thicker ZnO layers, which will be discussed in the next chapter (section 5.1.1).

Chapter 5 Optimization of the dielectric stack

In the previous chapter, we have shown the successful creation of the Maxwell-Wagner (MW) effect in the Al_2O_3/ZnO sub-nanometric laminates. The highest dielectric constant of about 300 was encountered in the Al_2O_3/ZnO (0.2/1 nm) laminates grown under an oxygen pressure of 0.005 mbar. However, the properties leave some space still for further optimization, especially regarding the dielectric losses. Also, the maximum value was found at the thick limit of the tested ZnO individual layer thickness. Therefore, in this chapter, some further optimization possibilities are pursued, namely the thickness optimization of the ZnO individual layer thickness (section 5.1.1), and subsequently a new optimization of the Al_2O_3 individual layer thickness (section 5.1.2). In earlier studies, approaches concerning rather the overall dielectric stack were shown to be also useful: the introduction of thicker Al_2O_3 films at the laminate/electrode interfaces (section 05.2.1) and of a TiN layer at the interface with the Si (section 5.2.2).

All laminates presented in this chapter were grown under the standard conditions, namely at 100 °C and under a pressure of 0.005 mbar. In these series, as the ZnO individual layer thickness is strongly enhances, the total number of bilayers was kept constant at 15. The total thickness of the laminates changes therefore between the laminates. The structural properties of the laminates in this chapter were analyzed also, but will not be shown here, as they are similar to what was observed in the previous chapter. All laminates show a high quality laminate structure, indicated by the Bragg peak related to the artificial periodicity, and comparable roughnesses.

5.1. Optimization the individual layer thickness in Al_2O_3/ZnO laminates

The MW effect was observed in Al_2O_3/ZnO (0.2/1 nm) laminate. However, high dielectric losses and high ac conductivity limits its applicability in the electronic industry. In order to reduce the dielectric losses by maintaining or increasing the dielectric constant, the individual layer thickness of the ZnO and the Al_2O_3 layers were further optimized, going to the nanometric range. Figure 75 shows the configuration of the nanometric laminates used to optimize the dielectric properties of Al_2O_3 /ZnO laminates.

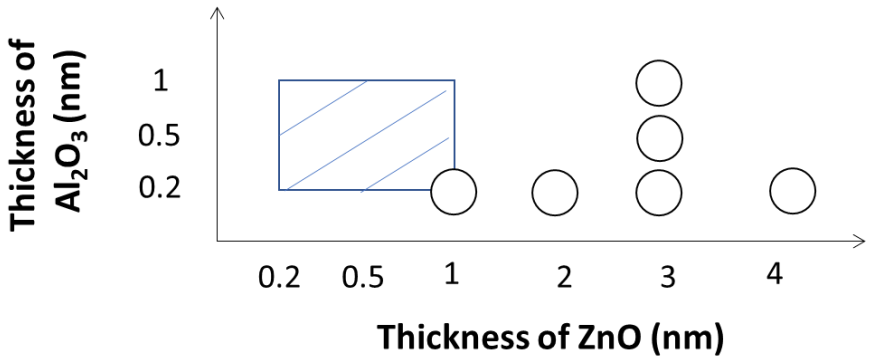

Figure 75 Thickness optimization. The rectangular section shows the sub-nanometric thickness range tested in the previous chapter; the circles indicate the individual layer thickness tested in this chapter.

5.1.1. Optimization of ZnO thickness

The semiconductor layer of ZnO in the laminate acts as the charge provider to obtain the charge accumulation at the interface, necessary for the MW effect. From the studies in the sub-nanometric laminates, we observe that when the thickness of the Al_2O_3 layer is 0.2 nm and thickness of ZnO is 1 nm in the laminate, the MW effect was present. For further enhancing the dielectric constant of the laminate, a series of samples with a fixed Al_2O_3 thickness of 0.2nm and a varying ZnO thickness (1, 2, 3, 4 nm) were prepared (as shown by the black circles in Figure 75). The same calibration method is followed as explained in section 2.3.2 to deposit these laminates. However, it has been observed that the deposition rate of ZnO was increasing with increasing thickness of the ZnO layer, hence, a mismatch with the targeted thickness of ZnO layer was observed. The finally obtained individual layer thickness of the ZnO layers were found to be 1.8, 2.8 and 4.4 nm in the laminates. The dielectric properties of these laminates were studied in frequency range of 10^2 to 10^5 Hz.

Figure 76 shows the dielectric properties of Al_2O_3/ZnO laminates as a function of the thickness of ZnO at a constant thickness of Al_2O_3 of 0.2 nm. All the laminates show a high tanδ, which indicates a highly conductive behavior of the films. A high charge density in ZnO layer and an insufficient Al_2O_3 layer thickness leads to a high leakage through these laminates. A maximum of the dielectric constant (and the dielectric losses) is observed for a ZnO individual layer thickness of about 3 nm.

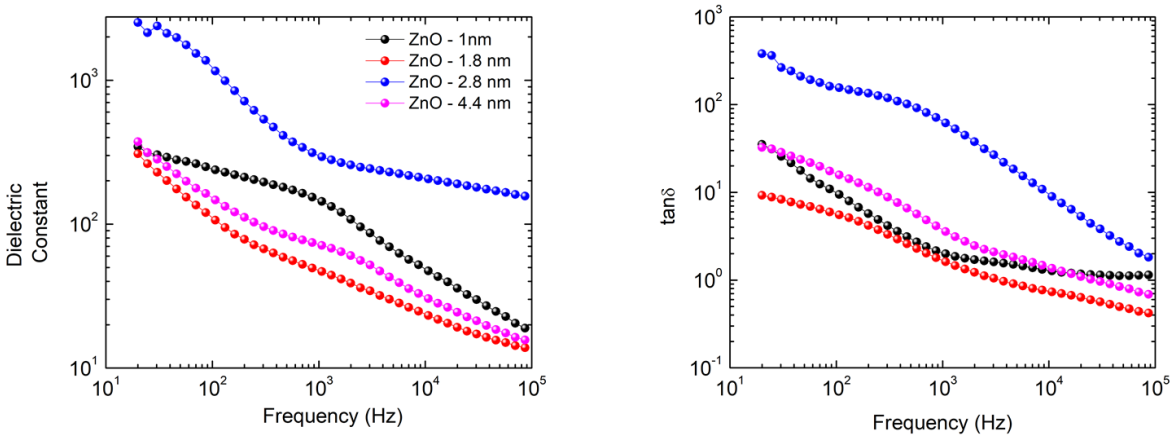

Figure 76 Dielectric properties of Al_2O_3/ZnO laminates as a function of the individual layer thickness of ZnO, at a constant individual layer thickness of Al_2O_3 of 0.2 nm

For further understanding of the behavior of these laminates, ellipsometry was performed in the wavelength range of 200 to 800 nm and the optical bandgap was calculated by extrapolating the linear part in the curve of $(\alpha h\nu)^2$ versus photon energy (hν) to intersect the abscissa [114], where h is the Planck constant, μ is the frequency of the incident photon and α is the absorption coefficient. Studies on Al_2O_3/ZnO laminates have shown that the optical bandgap of the laminates is a function of the thickness of the ZnO layer [114, 115], when the thickness decreases, the optical band gap increases. Jin Li et al explained that as the band gap of ZnO (3.3 eV) lies within the bandgap of Al_2O_3 (8.6 eV), a quantum well structure could be expected and when the thickness of the ZnO layer reduces below the Bohr radius of the ZnO (2.3 nm), the quantum effects play a role in the dielectric properties of the laminates [113]. The optical band gap of the laminates as a function of ZnO thickness is summarized in Figure 77. As the thickness of ZnO layer increases, a reduction in optical band gap was observed with a minimum at ZnO thickness of 1.8 nm and again an increase in the bandgap was observed as the thickness further decreases. This in contrast to what was observed in the nanolaminates, where the band gap tends to decrease with increasing thickness in the same thickness range (Figure 74 in section 4.4). Also, the preliminary measurements on a Al_2O_3/ZnO (0.64/0.84 nm) laminate showed higher values (shown in the same figure), more in accordance with the values found in literature. Probably, the effect at the origin of this returned thickness dependence for the laminates with nanometric ZnO and sub-nanometric Al_2O_3 is related to the extremely thin individual layer thickness of the Al_2O_3

layers. Both the preliminary and the cited measurements were made on a laminate with a thicker Al_2O_3 layer. This difference in thickness may change the electronic interaction between the ZnO layers, which would lead to a modified band gap. The here observed high tanδ values show that a high charge density, which is only moderately decoupled between the ZnO layers, is present.

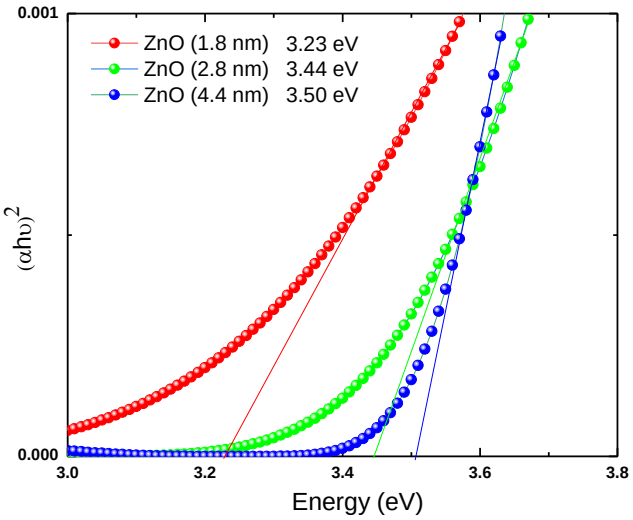

Figure 77 $(\alpha hv)^2$ as a function of photon energy of Al_2O_3/ZnO laminates as a function of ZnO thickness

Although, the underlying effect of this change of the bandgap modification with the ZnO individual layer thickness is not understood clearly and more studies are necessary, the obtained results indicate that the ZnO band gap is not a governing factor of the MW effect in the laminates. The dielectric properties show a maximum MW effect for the laminate with a ZnO individual layer thickness of 2.8 nm, while the ZnO band gap has a monotonous thickness dependence. It is not possible to explain the maximum of the MW effect with such a thickness dependence of the band gap. Thus, it seems that ZnO band gap modifications are not a critical factor for the determination of the MW effect in the laminates.

Based on the obtained dielectric properties, we have selected a ZnO thickness of 3 nm for the further optimization of the laminate structure. For this thickness, the highest dielectric constant was observed, although the losses were also very high. However, the further optimization will address the improvement of the charge confinement in the laminates, so that we have opted for

the ZnO thickness, which ensures a high charge density in ZnO layer, and therefore an important MW effect.

5.1.2. Optimization of Al_2O_3 thickness

After the optimization of the ZnO thickness, a series of laminates fixing the thickness of the ZnO layer at 3nm and varying the thickness of Al_2O_3 (0.2, 0.5 and 1nm) were prepared. The aim of this study was to obtain a critical thickness of the Al_2O_3 layer, which ensures low dielectric losses through the laminate while maintaining the high dielectric constant.

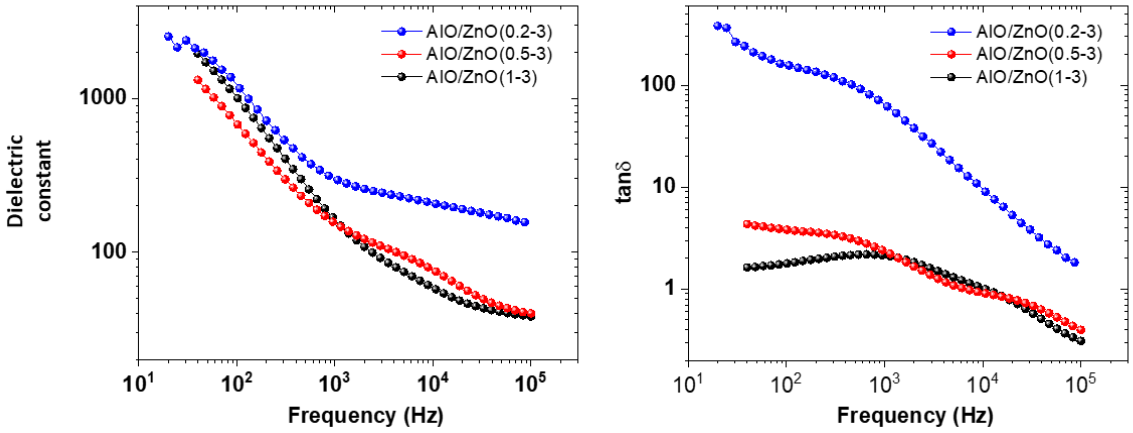

Figure 78 Dielectric properties of Al_2O_3/ZnO laminates as a function of the thickness of Al_2O_3 at a constant ZnO individual layer thickness of 3nm

The dielectric properties of the laminates as a function of the individual layer thickness of Al_2O_3 with a constant individual layer thickness of ZnO at 3nm are shown in Figure 78. As the individual layer thickness of Al_2O_3 increases, a strong reduction in the dielectric losses can be seen with a limited effect on the dielectric constant. This reduction is related to the thicker potential barrier provided by the Al_2O_3 layer for mobile charges in ZnO. For laminates with 1 nm thick Al_2O_3 layers, the tanδ value reduces to 1.8 at 200Hz while maintaining the dielectric constant of 800. The laminate with 0.5 nm thick Al_2O_3 layers shows a tanδ of 3 and a dielectric constant of 500. Based on this optimization we can conclude that 1nm thick Al_2O_3 can limit the conduction of charges through the laminate and facilitates the MW effect by accumulating them at the interface. However, a slight decrease of the relaxation frequency is observed, compared to the laminates with 0.2 nm thick Al_2O_3 individual layers. This can be also understood by the

better insulating properties of the Al_2O_3 layers, which lead to an enhancement of the resistivity of the interface component, and therefore to a reduction of the relaxation time of the MW effect (equation (13) in section 1.2.3). The coordinated optimization of the dielectric constant, the dielectric losses and the working frequency is therefore a tricky thing in these MW laminates.

5.2. Optimization of the dielectric stack

Earlier studies conducted on Al_2O_3/TiO_2 sub-nanometric laminates have shown important effects of the dielectric stack (apart from the individual layer thicknesses) on the dielectric properties of MW sub-nanometric laminates, both for ALD grown [47 116] and PLD grown [50] laminates. It was observed, that the introduction of thick Al_2O_3 layers at the interface between the laminate and the electrodes may lead to a strong decrease of the dielectric losses, while maintaining the dielectric constant at an acceptable level. This was attributed to the insulating effect of these layers, which maintain the charges inside the laminate and reduce therefore the overall losses. Also, rthe introduction of a TiN layer at the interface either with the bottom or the top electrode was found to be beneficial to reduce the dielectric losses and to enhance the MW effect. Therefore, we have also pursued these approaches for the optimization of the dielectric properties of the Al_2O_3/ZnO laminates.

For these optimizations, laminates with optimized individual layer thicknesses of 1 nm for the Al2O3 layers and 3 nm for the ZnO layers were used. They were grown under standard conditions by fixing the number of bilayers to 15.

5.2.1. Introduction of thick Al_2O_3 layers at the electrode interfaces

For this study, thick Al_2O_3 layers were introduced at the interface between the laminate and the electrodes of an Al_2O_3/ZnO (1/3 nm) laminate. The Al_2O_3 layers were grown under the same conditions as the laminates, i.e. at 100 °C and an oxygen pressure of 0.005 mbar. The single layers grown under these conditions show bulk like dielectric properties (section 3.1.1), ensuring good insulating properties. Three different samples were deposited: one with a 5 nm thick Al_2O_3 layer at the interface with the Si wafer, thus at the bottom electrode, one with a 5 nm thick Al_2O_3 layer at the interface with the top electrode, and one with 2.5 nm thick Al_2O_3 layer both at the bottom and the top interface. The smaller Al_2O_3 thickness for the samples with both top and bottom

interfacial layer was chosen as to keep the total Al_2O_3 thickness at the same value through the three samples. In this way, the influence of the interfacial Al_2O_3 capacitance on the apparent dielectric constant is the same for all three samples.

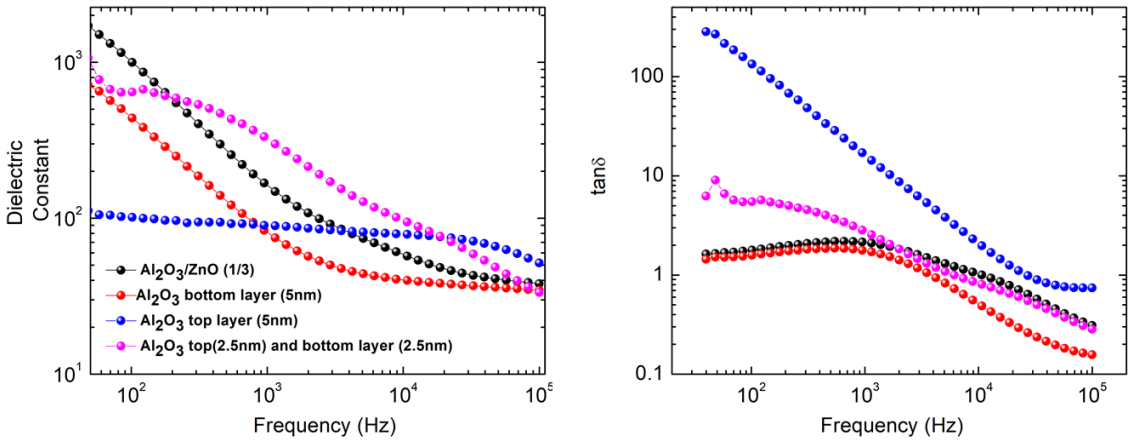

Figure 79 Dielectric constant and losses for a Al_2O_3/ZnO (1/3 nm) laminate, and for the same laminate with thick Al_2O_3 layers introduced at the interface with the top, the bottom, and both electrode interfaces

The dielectric properties of the reference laminate and the three samples with interfacial layers are shown in Figure 79. When introducing a 5 nm Al_2O_3 layer at the bottom interface, the dielectric constant decreases, while the tanδ stays similar comparted to the reference laminate without interfacial Al_2O_3 layers. In the case of an interfacial layer at the top electrode, the dielectric constant decreases strongly, while tanδ increases strongly. In the samples with interfacial Al_2O_3 layers both at the bottom and the top interface, the dielectric constant stays roughly comparable to the reference laminate, although the relaxation frequency increases, but tanδ increases also. Therefore, the interfacial Al_2O_3 layers do not have the expected effect to decrease the dielectric losses. None of the samples show a clear decrease of the losses compared to the reference laminate.

The reason of this affect is not clear, especially because the three samples with interfacial Al_2O_3 layers do not show a coherent evolution. The fact that the introduction of a bottom Al_2O_3 layer does not strongly alter the dielectric properties, regarding the losses and the relaxation frequency, indicates that the presence of the bottom layer does not strongly alter the properties of the laminates. The decrease of the dielectric constant can be explained by the series

capacitance of the Al_2O_3 interfacial layer. This decrease indicates at the same time, that the Al2O3 layer seems to retain its bulk properties as observed for the single films. Therefore, the bottom interfacial layer does not alter the growth or the structural properties of the laminates. On the other hand, the sample with the top interfacial layer shows profound changes of the dielectric properties. The strong increase of the losses, as well as a strong increase of the relaxation frequency cannot be explained without a modification of the laminate dielectric properties. The reason for this modification is not clear, as only another layer was introduced at the top of the laminate, directly after its growth. A degradation of the laminate quality seems to be unlikely, and a bad deposition quality of the Al_2O_3 layer can also not be responsible for such profound changes. Finally, the properties of the sample with two interfacial layers can be interpreted as a mixture of the effects of the bottom and the top interfacial layers. The relaxation frequency is enhanced and the losses also, but not as strongly as in the sample with only the top interfacial layers.

The observed properties indicate that the introduction of thick Al_2O_3 layers at the interfaces with the electrodes does not have the expected effect of charge confinement in the Al_2O_3/ZnO laminates, contrary to what was observed for Al_2O_3/TiO_2 laminates. The reason for this behavior stays unclear at the moment, and further studies have to be conducted to clarify the ongoing effects.

5.2.2. Introduction of a* TiN layer

Titanium nitride, TiN, is an alternative electrode material, widely used in microelectronics studies, because of its compatibility with Si based CMOS systems, binary oxide dielectrics, and a modified work function in comparison to Si [117]. In earlier studies on Al_2O_3/TiO_2 sub-nanometric laminates, the introduction of a TiN layer between the laminate and the Si or Ag interface has shown beneficial effects, principally regarding the importance of the MW effect. For ALD grown laminates, the use of a TiN electrode was mandatory in order to establish the MW effect in the laminates [47] , while in PLD grown laminates, the introduction of such a layer enhanced strongly the MW effect [50] . The exact role of the TiN layer was not clearly established, but the change

in work function, as also a good chemical compatibility and adhesion properties with Al_2O_3 [118] may have their role in the observed modifications of the MW effect in sub-nanometric laminates.

For this study, we have used (001) Si substrates covered with a crystalline TiN film of about 300 nm, provided by IPdiA. The roughness of these substrates are comparable with bare Si substrates, allowing for the growth of sub-nanometric laminates on top. The structural characterization of the Al_2O_3/ZnO laminates, grown under standard conditions, did not show an important alteration of the laminate quality, which is comparable to the other laminates used in this thesis. The optimized laminate structure of Al_2O_3/ZnO (1/3 nm) was used, both as a "bare" laminate, as well as with thick Al_2O_3 interfacial layers. The configuration of the interfacial layers is the same as those studied in the previous section.

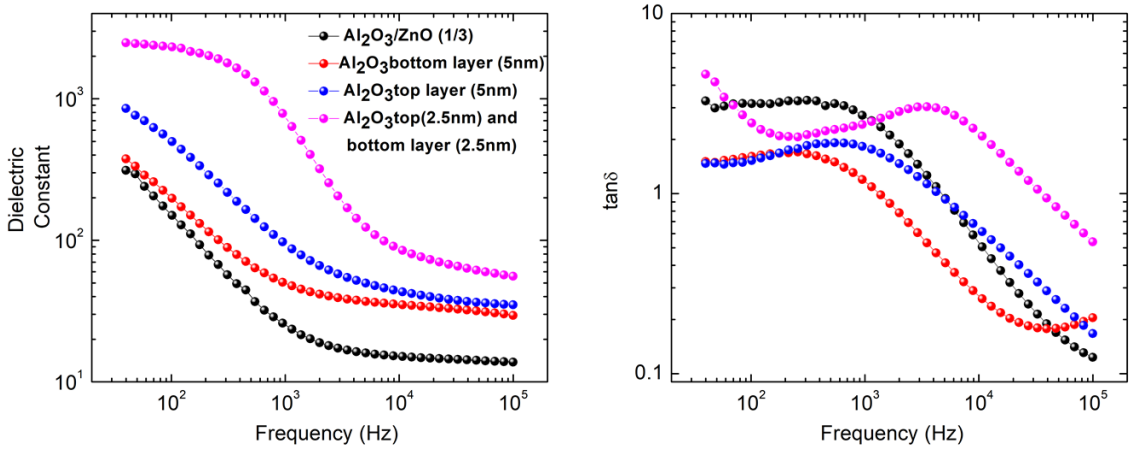

Figure 80 Dielectric constant and losses for a Al_2O_3/ZnO (1/3 nm) laminate grown in a Si/TiN substrate, and for the same laminate with thick Al_2O_3 layers introduced at the interface with the top, the bottom, and both electrode interfaces

Figure 80 shows the dielectric properties of the different dielectric stacks on the TiN-covered Si substrates. Compared to the laminate directly deposited in Si (Figure 79), the bare Al_2O_3/ZnO (1/3 nm) laminate does not show significant changes in the frequency dependence, except a slightly lower dielectric constant of 400 at low frequency. The losses are slightly enhanced to a value of about 3 (compared to 2 for the bare Si substrate). Therefore, the TiN layer does not alter strongly the observed properties of the Al_2O_3/ZnO (1/3 nm) laminate. This observation, contrary to what was observed in Al_2O_3/TiO_2 laminates, indicates that the TiN layer does not enhance the

MW effect further, but that even in laminates directly deposited on Si, the MW effect is already maximally exploited.

Figure 80 also shows the properties of the laminates with interfacial Al_2O_3 layers. Here, significant changes are observed in comparison with the stacks grown directly in Si. When regarding the sample with a 5 nm Al_2O_3 layer at the bottom interface, again, the dielectric properties are similar to what is observed for the laminate without interfacial layers, but the dielectric constant enhances slightly. Taking into account the series capacitance of the interfacial Al_2O_3 layer, this enhancement indicates that the laminate dielectric constant is enhanced by the presence of the interfacial layer. The dielectric losses decrease, compared to the bare laminate. This can be understood by the charge confining effect of the interfacial layer. The laminate with a top interfacial Al_2O_3 layer confirms these findings. Again, the dielectric constant increases, even more strongly than in the case of the bottom interfacial layer. The losses stay on the same level as for the bottom interfacial layer, indicating again a charge confinement effect.

The most important differences are observed for a laminate with interfacial layers at both electrode interfaces. Here, the dielectric constant increase strongly to a value of about 2000. At the same time, the relaxation frequency increases to a value of about 10^3 Hz, extending the working frequency range. The losses are intermediate compared to the bare laminate and the laminates with only one interfacial layer, and additionally showing an uprise at low frequencies. This may be because for the dielectric stack with two interfacial layers, a smaller value of the Al_2O_3 thickness was chosen. The losses are situated slightly above 1, which is an excellent value for dielectric materials with a dielectric constant above 1000.

Therefore, although the presence of the TiN layer does not have a strong influence on the properties of the bare laminate, it does have a strong combined influence together with the interfacial layers. The expected behavior of the interfacial layers is observed, i.e. a better confinement of the charges inside the laminate, limiting the losses, but even more, enhancing the dielectric constant. This can be understood considering that with a smaller leakage of the charges into the electrodes, they can be more efficiently accumulated at the internal interfaces of the laminates. This strong interaction of the interfacial layers with the presence of the TiN electrode does not seem to stem from a growth induced effect. The bare laminate on the TiN

shows similar properties as on the Si substrate. But even more, the laminate with only a top Al_2O_3 layer shows the beneficial effect of the interfacial layer only when deposited on the TiN-covered Si. Chemical effects, modifying the charge density in the laminate can be excluded, too, as the internal structure of the laminate does not change. Therefore, the observed effect seems to be purely electronic in nature, but we are not able to deduce the exact character based on the shown observations.

Although, the combined effect of the TiN layer and the Al_2O_3 interfacial layers stays a mystery at this point, it improves strongly the dielectric properties. With a dielectric constant of about 2000 and dielectric losses in the range of 1, this laminate-based dielectric is still not ideal, but approaches clearly the manageable property range for application in high-density capacitances or gate dielectrics. Further optimization of the thickness of the Al_2O_3 interfacial layers may allow to reduce the losses even further, with a limited effect on the dielectric constant, if charge accumulation in the laminate is still enhanced by the interfacial layers. Further studies are necessary, but Al_2O_3/ZnO laminates do clearly show promising results for applications, where relatively high losses can be tolerated.

Conclusions

The miniaturization of the electronic devices and a need for the high energy storage triggered the research for the high-density capacitances. Initially, the need for high density capacitances was fulfilled by reducing the thickness of the dielectric (SiO_2), until a minimum thickness was reached where the tunneling through the SiO_2 creates problems of high losses through the dielectric. This effect shows the necessity of new dielectric materials, and over the last few decades, various materials (binary oxides, ternary oxides and laminates) have been explored for this purpose.

This thesis was an effort to develop a new high dielectric constant material for the application in high density capacitances. We explored the sub-nanometric laminates of binary oxides by performing structural analysis and dielectric properties analysis. Al_2O_3, Y_2O_3 and ZnO are used to develop laminate structures of Al_2O_3/ZnO , Al_2O_3/Y_2O_3 and Y_2O_3/ZnO by Pulsed Laser Deposition. In order to optimize the deposition parameters for each material, single films of binary oxides were deposited by varying the deposition temperatures and the deposition oxygen pressures. As a first step, we have presented a detailed analysis of dielectric properties of single films of Al_2O_3, Y_2O_3 and ZnO as a function of deposition temperature and deposition pressure.

Al_2O_3 films grown at different temperatures showed amorphous behavior and a negligible influence on the dielectric properties. However, the deposition pressure has a strong influence on the structural and dielectric properties. As the deposition pressure increases, the films became rougher and an effect on the stoichiometry was also observed with an increase in O/Al ratio at high deposition pressure. The deposition pressure affected also the dielectric properties of the films and an enhancement in dielectric constant and dielectric losses is observed. This could be related to the presence of topological defects, related to the roughness of the films, and of chemical defects, related to the presence of interstitial oxygen pairs in the films deposited at high oxygen pressure.

The study of ZnO single films showed that, as the deposition temperature of the film increases, the crystallinity of the film improves. At 200 °C, we observed the presence of crystalline order in the ZnO films, which was further intensified as the temperature reached 300°C. A direct influence of the crystallinity of the films on the dielectric properties was also observed, so that

for further studies, a deposition temperature of 100° C was selected. The deposition pressure affects the stoichiometry of ZnO films, and deposition at low pressure causes a high density of the oxygen vacancies in film. These oxygen vacancies were found to induce a high conduction and dielectric losses.

From these preliminary studies, the standard deposition parameters for the laminate structures were selected: a deposition temperature of 100°C and a deposition oxygen pressure of 0.005mbar. These deposition parameters ensure the amorphous nature of films, with a high, but not too high, charge concentration in ZnO. Sub-nanometric laminates of Al_2O_3/Y_2O_3, Al_2O_3/ZnO, and Y_2O_3/ZnO were deposited. The Al_2O_3/Y_2O_3 laminates did not show a Maxwell-Wagner effect, as expected from the absence of a charge containing material. The sub-nanometric laminates of Al_2O_3 and ZnO did show the Maxwell – Wagner effect at the interface of the insulating (Al_2O_3) and the semiconducting (ZnO) layers. The artificial bilayer periodicity of the laminates was observed by the X-ray analysis. The individual layer thickness of each constituent plays a critical role in defining the dielectric properties, and we have observed that the laminate Al_2O_3/ZnO (0.2/1 nm) showed a high dielectric constant of 211 at 200 Hz due to the Maxwell-Wagner effect. The equivalent circuit analysis showed that the interface properties are the governing factors. Dielectric properties as a function of deposition pressure were also studied, and the oxygen exchange between the individual layers was pointed out as one of the main influence on the properties of these laminate structures. For the Y_2O_3/ZnO, no Maxwell-Wagner effect was observed in the sub-nanometric individual layer thickness range, probably due to an oxygen exchange at the internal interfaces, suppressing the charge density of the ZnO layers.

To further enhance the Mawxell-Wagner effect and to reduce the losses, an optimization of the individual layer thickness reaching the nanometric thickness range was carried out. We found that Al_2O_3/ZnO (1/3 nm) laminates showed the most promising results with a dielectric constant of 800 and tanδ of 1.8 at 200Hz. This shows that, in order to obtain a Maxwell-Wagner effect in this system, the sub-nanometric thickness of the individual layers in the laminates are not required. For industrial application, this is a beneficial factor. Further, by the optimization of the dielectric stack, the best properties were obtained for the Al_2O_3/ZnO (1/3) laminate

deposited on TiN with a 2.5 nm thick Al_2O_3 layer at the interface of both electrodes and the laminate. The dielectric constant of 2500 with the tanδ of 2 at 200Hz was obtained for this dielectric stack. Even at high frequency the dielectric constant was found to be higher than the constituents of laminate. However in this thesis we focused on the low frequency dielectric properties.

For the industrial application, the obtained dielectric constant of 2000 is an important enhancement, especially as it is based on amorphous binary oxides. The currently used high-k oxide, HfO_2, has a dielectric constant of 25. However, the dielectric losses of the ZnO-based laminates is still too high. For future dielectrics, laminates of Al_2O_3/ZnO can be an interesting solution, if we would be able to limit the tanδ, even at the cost of a reduction of the dielectric constant by an order of 10. This is likely to be achievable with further optimization of the laminate and its dielectric stack, first of all by the thickness of the interfacial Al_2O_3 layers. For industrial application, a large surface area deposition technique allowing for the deposition in trench structures would be a necessity. Hence, in the future it would be interesting to develop the deposition of these laminates using the Atomic layer deposition technique.

Summary

This dissertation is an effort to develop new high dielectric constant materials for high- density capacitances and presents a detailed study of dielectric properties of amorphous sub-nanometric laminates (Al_2O_3/ZnO, Y_2O_3/ZnO and Al_2O_3/Y_2O_3) deposited by Pulsed Laser Deposition (PLD). In order to determine the optimal conditions for the deposition of the sub-nanometric laminates, single films of Al_2O_3, Y_2O_3 and ZnO were studied in a first step and the effect of the main deposition parameters on the single film properties were established. For the laminate structures, the effect of the internal interfaces of the laminate on the dielectric properties have been studied and presented in detail. A high dielectric constant is obtained in Al_2O_3/ZnO laminates by the Maxwell – Wagner effect, because of the accumulation of charges at the internal interfaces of the laminate. Equivalent circuit analysis has been carried out to determine the main electrical characteristics of the sub-nanometric individual layers and their interfaces. The activation energies of the charge carriers in the laminates were deduced from high-temperature impedance spectroscopy. The effect of the deposition pressure and individual layer thickness of the constituent materials on the dielectric properties of the laminates are studied and the importance of an optimal individual thickness for each material is highlighted. For further optimization of the Maxwell-Wagner effect with low associated dielectric losses, the individual layer thickness was enhanced into the nanometric scale, and the total dielectric stack has been adapted.

Appendix 1

Calculation of O/Al ratio using XRR curve fitting

The X-ray scattering length, obtained by GenX fitting of the XRR data, is related to the stoichiometry of the materials. For example, we can express the complex scattering length of Al_xO_y as:

$$SL_{Al_xO_y} = (x * f'_{Al} + y * f'_O) + i.(x * f''_{Al} + y * f''_O)$$

Where f'_{Al} and $'f'_O$ are the real part of the atomic form factor of Al and O, and f''_{Al} and f''_O are the imaginary part of the atomic form factor under Cu Kα radiation. The values of atomic form factors were taken from the Henke table [78]. By fitting the real and imaginary part of complex scattering length, we were able to get two equations as:

$$SL'_{Al_xO_y} = (x * f'_{Al} + y * f'_O)$$

$$SL''_{Al_xO_y} = (x * f'_{Al} + y * f'_O)$$

By solving these equations values of x and y were calculated, where x represents the number of atoms of Al and y represents number of atoms of O.

References:

[1] X. Hao, “A review on the dielectric materials for high energy-storage application,” *J. Adv. Dielectr.*, vol. 03, no. 01, p. 1330001, 2013, doi: 10.1142/s2010135x13300016.

[2] J. Yota, R. Ramanathan, K. Kwok, J. Arreaga, T. Ko, and H. Shao, “In search of higher density mim capacitor for GaAs RF power applications,” *Proc. - Electrochem. Soc.*, vol. PV 2005-04, pp. 315–329, 2005, doi: 10.1149/ma2005-01/13/591.

[3] S. Kimura, “Capacitor over bitline (COB) DRAM cell and its contributions to high density DRAMs,” *Int. Symp. VLSI Technol. Syst. Appl. Proc.*, pp. 79–80, 2008, doi: 10.1109/VTSA.2008.4530807.

[4] Ethan Mollick, “Establishing Moore ’ s Law,” *IEEE Comput. Soc.*, Vol 28 , pp. 62–75, 2006.

[5] G. E. Moore, “Cramming more components onto integrated circuits, Reprinted from Electronics, volume 38, number 8, April 19, 1965, pp.114 ff.,” *IEEE Solid-State Circuits Soc. Newsl.*, vol. 11, no. 3, pp. 33–35, 2009, doi: 10.1109/n-ssc.2006.4785860.

[6] M. T. Heath, “A tale of two laws,” *Int. J. High Perform. Comput. Appl.*, vol. 29, no. 3, pp. 320–330, 2015, doi: 10.1177/1094342015572031.

[7] K. E. Bean, “Anisotropic etching of silicon,” *IEEE Trans. Electron Devices*, vol. 25, no. 10, pp. 1185–1193, 1978, doi: 10.1109/T-ED.1978.19250.

[8] J. vom Dorp, T. Erlbacher, A. J. Bauer, H. Ryssel, and L. Frey, “Dielectric layers suitable for high voltage integrated trench capacitors,” *J. Vac. Sci. Technol. B, Nanotechnol. Microelectron. Mater. Process. Meas. Phenom.*, vol. 29, no. 1, p. 01AB04, 2011, doi: 10.1116/1.3525283.

[9] S. Lombardo, J. H. Stathis, B. P. Linder, K. L. Pey, F. Palumbo, and C. H. Tung, “Dielectric breakdown mechanisms in gate oxides,” *J. Appl. Phys.*, vol. 98, no. 12, 2005, doi: 10.1063/1.2147714.

[10] D.R. Wolters and A.T.A. Zegers-van Duijnhoven, “Tunneling in thin SiO_2,” *R. Soc.*, vol. 354, pp. 2327–2350, 1996, [Online]. Available: https://doi.org/10.1098/rsta.1996.0103.

[11] M. Städele, B. R. Tuttle, and K. Hess, “Tunneling through ultrathin SiO_2 gate oxides from microscopic models,” *J. Appl. Phys.*, vol. 89, no. 1, pp. 348–363, 2001, doi: 10.1063/1.1330764.

[12] F. Kremer and A. Schönhals, *Broadband dielectric spectroscopy*. Springer 2003.

[13] P. Walke *et al.*, "Giant dielectric constant in TiO_2/Al_2O_3 nanolaminates grown on doped silicon substrate by pulsed laser deposition," *J. Appl. Phys.*, vol. 115, no. 9, 2014, doi: 10.1063/1.4867780.

[14] W. Li, O. Auciello, R. N. Premnath, and B. Kabius, "Giant dielectric constant dominated by Maxwell-Wagner relaxation in Al_2O_3 / TiO_2 nanolaminates synthesized by atomic layer deposition," *Appl. Phys. Lett.*, vol. 96, no. 16, 2010, doi: 10.1063/1.3413961.

[15] W. Li and R. W. Schwartz, "Maxwell-Wagner relaxations and their contributions to the high permittivity of calcium copper titanate ceramics," *Phys. Rev. B - Condens. Matter Mater. Phys.*, vol. 75, no. 1, pp. 1–4, 2007, doi: 10.1103/PhysRevB.75.012104.

[16] J. Liu, C. G. Duan, W. N. Mei, R. W. Smith, and J. R. Hardy, "Dielectric properties and Maxwell-Wagner relaxation of compounds $ACu_3Ti_4O_{12}$ (A=Ca,Bi 2/3 ,Y 2/3,La 2/3)," *J. Appl. Phys.*, vol. 98, no. 9, pp. 1–6, 2005, doi: 10.1063/1.2125117.

[17] L. Liu, T. Rojac, D. Damjanovic, M. Di Michiel, and J. Daniels, "Frequency-dependent decoupling of domain-wall motion and lattice strain in bismuth ferrite," *Nat. Commun.*, vol. 9, no. 1, pp. 1–10, 2018, doi: 10.1038/s41467-018-07363-y.

[18] R. Chau *et al.*, "Application of high-κ gate dielectrics and metal gate electrodes to enable silicon and non-silicon logic nanotechnology," *Microelectron. Eng.*, vol. 80, no. SUPPL., pp. 1–6, 2005, doi: 10.1016/j.mee.2005.04.035.

[19] J. Robertson, "High dielectric constant oxides," *Eur. Phys. JournalApplied Phys.*, vol. 184, no. 3, pp. 177–184, 2004, doi: 10.1051/epjap.

[20] J. Sponsored, "International Technology Roadmap for Semiconductors 2002 Update," *Update*, 2002. https://ece.northeastern.edu/edsnu/mcgruer/class/eceu606/2002Update.pdf

[21] G. He, L. Zhu, Z. Sun, Q. Wan, and L. Zhang, "Integrations and challenges of novel high-k gate stacks in advanced CMOS technology," *Prog. Mater. Sci.*, vol. 56, no. 5, pp. 475–572, 2011, doi: 10.1016/j.pmatsci.2011.01.012.

[22] K. J. Hubbard AND D. G. Schlom, "Thermodynamic stability of binary oxides in contact with silicon," *J. Mater. Res.*, vol. 11, no. 11, pp. 2757–2776, 1996, doi:

10.1017/CBO9781107415324.004.

[23] E. L. Albuquerque and M. S. Vasconcelos, “Structural, electronics and optical properties of CaO,” *J. Phys. Conf. Ser.*, vol. 100, no. PART 4, 2008, doi: 10.1088/1742-6596/100/4/042006.

[24] M. D. Groner, J. W. Elam, F. H. Fabreguette, and S. M. George, “Electrical characterization of thin Al2O3 films grown by atomic layer deposition on silicon and various metal substrates,” *Thin Solid Films*, vol. 413, no. 1–2, pp. 186–197, 2002, doi: 10.1016/S0040-6090(02)00438-8.

[25] A. Posadas, F. J. Walker, C. H. Ahn, T. L. Goodrich, Z. Cai, and K. S. Ziemer, “Epitaxial MgO as an alternative gate dielectric for SiC transistor applications,” *Appl. Phys. Lett.*, vol. 92, no. 23, pp. 1–5, 2008, doi: 10.1063/1.2944865.

[26] M. Sterrer, N. Nilius, S. Shaikhutdinov, M. Heyde, T. Schmidt, and H. J. Freund, “Interaction of water with oxide thin film model systems,” *J. Mater. Res.*, vol. 34, no. 3, pp. 360–378, 2019, doi: 10.1557/jmr.2018.454.

[27] J. H. Choi, Y. Mao, and J. P. Chang, “Development of hafnium based high-k materials - A review,” *Mater. Sci. Eng. R Reports*, vol. 72, no. 6, pp. 97–136, 2011, doi: 10.1016/j.mser.2010.12.001.

[28] M. Kadoshima *et al.*, “Rutile-type TiO2 thin film for high-k gate insulator,” *Thin Solid Films*, vol. 424, no. 2, pp. 224–228, 2003, doi: 10.1016/S0040-6090(02)01105-7.

[29] M. Ben Elbahri, A. Kahouli, B. Mercey, W. Prellier, and U. Lüders, “Effects of oxygen pressure during deposition on the dielectric properties of amorphous titanium dioxide thin films,” *J. Phys. D. Appl. Phys.*, vol. 15, no. 17, 2019, doi: 10.1088/1361-6463/ab06a1.

[30] Y. W. Yoo, W. Jeon, W. Lee, C. H. An, S. K. Kim, and C. S. Hwang, “Structure and electrical properties of Al-doped HfO_2 and ZrO_2 films grown via atomic layer deposition on Mo electrodes,” *ACS Appl. Mater. Interfaces*, vol. 6, no. 24, pp. 22474–22482, 2014, doi: 10.1021/am506525s.

[31] O. Auciello *et al.*, “Hybrid titanium-aluminum oxide layer as alternative high-k gate dielectric for the next generation of complementary metal-oxide-semiconductor devices,” *Appl. Phys. Lett.*, vol. 86, no. 4, pp. 1–4, 2005, doi: 10.1063/1.1856137.

[32] R. Lo Nigro, E. Schilirò, G. Greco, P. Fiorenza, and F. Roccaforte, “Laminated Al_2O_3-HfO_2 layers grown by atomic layer deposition for microelectronics applications,” *Thin Solid Films*, vol. 601, pp. 68–72, 2016, doi: 10.1016/j.tsf.2015.11.037.

[33] I. Iatsunskyi *et al.*, "Study on Structural, Mechanical, and Optical Properties of Al_2O_3-TiO_2 Nanolaminates Prepared by Atomic Layer Deposition," *J. Phys. Chem. C*, vol. 119, no. 35, pp. 20591–20599, 2015, doi: 10.1021/acs.jpcc.5b06745.

[34] H. J. Cho *et al.*, "New TIT capacitor with ZrO_2/Al_2O_3/ZrO_2 dielectrics for 60 nm and below DRAMs," *Solid. State. Electron.*, vol. 51, no. 11–12, pp. 1529–1533, 2007, doi: 10.1016/j.sse.2007.09.030.

[35] H. Hu *et al.*, "CMOS technology: High performance ALD HfO_2-Al_2O_3 laminate MIM capacitors for RF and mixed signal IC applications," *Sel. Semicond. Res.*, pp. 323–326, 2011, doi: 10.1142/9781848164079_0006.

[36] S. J. Ding *et al.*, "Evidence and understanding of ALD HfO_2-Al_2O_3 laminate MIM capacitors outperforming sandwich counterparts," *IEEE Electron Device Lett.*, vol. 25, no. 10, pp. 681–683, 2004, doi: 10.1109/LED.2004.835791.

[37] P. K. Park, E. S. Cha, and S. W. Kang, "Interface effect on dielectric constant of HfO_2/Al_2O_3 nanolaminate films deposited by plasma-enhanced atomic layer deposition," *Appl. Phys. Lett.*, vol. 90, no. 23, pp. 1–4, 2007, doi: 10.1063/1.2746416.

[38] Chandreswar Mahata *et al.*, "Comparative Study of Atomic-Layer-Deposited Stacked (HfO2/Al2O3) and Nanolaminated (HfAlOx) Dielectrics on In0.53Ga0.47As," Appl. Mater. Interfaces 2013, 5, 4195−4201.

[39] I. Krylov, B. Pokroy, M. Eizenberg, and D. Ritter, "A comparison between HfO_2/Al_2O_3 nano-laminates and ternary Hf_xAl_yO compound as the dielectric material in InGaAs based metal-oxide-semiconductor (MOS) capacitors," *J. Appl. Phys.*, vol. 120, no. 12, 2016, doi: 10.1063/1.4962855.

[40] Y. Liang, N. D. Theodore, J. Curless, and C. Tracy, "Physical and electrical properties of nanolaminated HfO 2/ LaAlO 3HfO 2 dielectric on Si," *J. Appl. Phys.*, vol. 99, no. 6, pp. 2004–2007, 2006, doi: 10.1063/1.2186026.

[41] K. Kukli, J. Ihanus, M. Ritala, and M. Leskela, "Tailoring the dielectric properties of HfO_2-Ta_2O_5 nanolaminates," *Appl. Phys. Lett.*, vol. 68, no. 26, pp. 3737–3739, 1996, doi: 10.1063/1.115990.

[42] Q. Zhang, J. Li, and X. Bi, "Semiconducting ZnO effect on Maxwell-Wagner relaxation in HfO_2/ZnO nanolaminates fabricated by atomic layer deposition," *J. Phys. D. Appl. Phys.*, vol. 47, no. 50, 2014, doi: 10.1088/0022-3727/47/50/505302.

[43] F. Benner *et al.*, " Atomic layer deposited high- κ nanolaminates for silicon surface passivation ," *J. Vac. Sci. Technol. B, Nanotechnol. Microelectron. Mater. Process. Meas. Phenom.*, vol. 32, no. 3, p. 03D110, 2014, doi: 10.1116/1.4863499.

[44] V. Mikhelashvili, E. Garshtein, and G. Eisenstein, "Characteristics of Al_2O_3/TiO_2 nanolaminates and AlTiO thin films on Si," *IEEE Electron Device Lett.*, vol. 27, no. 5, pp. 344–346, 2006, doi: 10.1109/LED.2006.873879.

[45] G. Zhang, H. Wu, C. Chen, T. Wang, J. Yue, and C. Liu, "Transparent and flexible capacitors based on nanolaminate Al2O3/TiO2/Al2O3," *Nanoscale Res. Lett.*, vol. 10, no. 1, 2015, doi: 10.1186/s11671-015-0784-8.

[46] G. Lee, B. K. Lai, C. Phatak, R. S. Katiyar, and O. Auciello, "Tailoring dielectric relaxation in ultra-thin high-dielectric constant nanolaminates for nanoelectronics," *Appl. Phys. Lett.*, vol. 102, no. 14, 2013, doi: 10.1063/1.4790838.

[47] A. Kahouli *et al.*, "Structural and Dielectric Properties of Subnanometric Laminates of Binary Oxides," *ACS Appl. Mater. Interfaces*, vol. 7, no. 46, pp. 25679–25684, 2015, doi: 10.1021/acsami.5b06485.

[48] A. Kahouli, O. Lebedev, V. H. Dao, M. Ben Elbahri, W. Prellier, and U. Lüders, "Electrical characteristics and conduction mechanisms of amorphous subnanometric Al_2O_3-TiO_2 laminate dielectrics deposited by atomic layer deposition," *Appl. Phys. Lett.*, vol. 109, no. 20, 2016, doi: 10.1063/1.4967534.

[49] A. Kahouli, Marwa Ben Elbahri, O. Lebedev and U. Lüders "Capacitance – voltage characteristics of sub-nanometric Al_2O_3 / TiO_2 laminates : dielectric and interface charge densities," *J. Phys. Condens. Matter*, vol. 29, no. 275301, 2017.

[50] M. Ben Elbahri, A. Kahouli, B. Mercey, O. Lebedev, W. Donner, and U. Lüders, "Study on the dielectric properties of Al_2O_3/TiO_2 sub-nanometric laminates: Effect of the bottom electrode and the total thickness," *J. Phys. D. Appl. Phys.*, vol. 51, no. 6, 2018, doi: 10.1088/1361-6463/aaa4df.

[51] J. N. Zeng, J. K. Low, Z. M. Ren, T. Liew, and Y. F. Lu, "Effect of deposition conditions on optical and electrical properties of ZnO films prepared by pulsed laser deposition," *Appl. Surf. Sci.*, vol. 197–198, pp. 362–367, 2002, doi: 10.1016/S0169-4332(02)00425-7.

[52] G. D. Wilk, R. M. Wallace, and J. M. Anthony, “High-κ gate dielectrics: Current status and materials properties considerations,” *J. Appl. Phys.*, vol. 89, no. 10, pp. 5243–5275, 2001, doi: 10.1063/1.1361065.

[53] R. G. Bankras, J. Holleman, and P. H. Woerlee, “Characterization of Pulsed Laser Deposited Al_2O_3 Gate Dielectric R.G.,” vol. 10, no. 1, pp. 19–20, 2013.

[54] S. D. Ponja, I. P. Parkin, and C. J. Carmalt, “Synthesis and material characterization of amorphous and crystalline (α-) Al2O3: Via aerosol assisted chemical vapour deposition,” *RSC Adv.*, vol. 6, no. 105, pp. 102956–102960, 2016, doi: 10.1039/c6ra24018f.

[55] S. Prasanna, R. G. Mohan, S. Jayakumar, M. D. Kannan, and V. Ganesan, “Dielectric properties of DC reactive magnetron sputtered Al 2O 3 thin films,” *Thin Solid Films*, vol. 520, no. 7, pp. 2689–2694, 2012, doi: 10.1016/j.tsf.2011.11.040.

[56] Y. Zhang *et al.*, “Investigation of the defect density in ultra-thin Al_2O_3 films grown using atomic layer deposition,” *Surf. Coatings Technol.*, vol. 205, no. 10, pp. 3334–3339, 2011, doi: 10.1016/j.surfcoat.2010.12.001.

[57] C. V. Ramana, V. H. Mudavakkat, K. K. Bharathi, V. V. Atuchin, L. D. Pokrovsky, and V. N. Kruchinin, “Enhanced optical constants of nanocrystalline yttrium oxide thin films,” *Appl. Phys. Lett.*, vol. 98, no. 3, pp. 98–101, 2011, doi: 10.1063/1.3524202.

[58] S. Zhang and R. Xiao, “Yttrium oxide films prepared by pulsed laser deposition,” *J. Appl. Phys.*, vol. 83, no. 7, pp. 3842–3848, 1998, doi: 10.1063/1.366615.

[59] M. Mishra, P. Kuppusami, T. N. Sairam, A. Singh, and E. Mohandas, “Effect of substrate temperature and oxygen partial pressure on microstructure and optical properties of pulsed laser deposited yttrium oxide thin films,” *Appl. Surf. Sci.*, vol. 257, no. 17, pp. 7665–7670, 2011, doi: 10.1016/j.apsusc.2011.03.156.

[60] R. J. Gaboriaud, F. Pailloux, P. Guerin, and F. Paumier, “Yttrium oxide thin films, Y_2O_3, grown by ion beam sputtering on Si,” *J. Phys. D. Appl. Phys.*, vol. 33, no. 22, pp. 2884–2889, 2000, doi: 10.1088/0022-3727/33/22/304.

[61] C. Durand *et al.*, “Microstructure and electrical characterizations of yttrium oxide and yttrium silicate thin films deposited by pulsed liquid-injection plasma-enhanced metal-organic chemical

vapor deposition," *J. Appl. Phys.*, vol. 96, no. 3, pp. 1719–1729, 2004, doi: 10.1063/1.1766412.

[62] J. Kwo *et al.*, "High ε gate dielectrics $Gd_2O_3$and Y_2O_3 for silicon," *Appl. Phys. Lett.*, vol. 77, no. 1, pp. 130–132, 2000, doi: 10.1063/1.126899.

[63] O. Pons-Y-Moll *et al.*, "Structural and optical properties of rare-earth-doped Y_2O_3 waveguides grown by pulsed-laser deposition," *J. Appl. Phys.*, vol. 92, no. 9, pp. 4885–4890, 2002, doi: 10.1063/1.1508422.

[64] P. Lei, J. Zhu, Y. Zhu, C. Jiang, and X. Yin, "Yttrium oxide thin films prepared under different oxygen-content atmospheres: Microstructure and optical properties," *Appl. Phys. A Mater. Sci. Process.*, vol. 108, no. 3, pp. 621–628, 2012, doi: 10.1007/s00339-012-6940-4.

[65] J. X. Zheng, G. Ceder, T. Maxisch, W. K. Chim, and W. K. Choi, "Native point defects in yttria and relevance to its use as a high-dielectric-constant gate oxide material: First-principles study," *Phys. Rev. B - Condens. Matter Mater. Phys.*, vol. 73, no. 10, pp. 1–7, 2006, doi: 10.1103/PhysRevB.73.104101.

[66] F. Jollet, C. Noguera, M. Gautier, N. Thromat, and J. Duraud, "Oxygen vacancies dependent phase transition of Y_2O_3 films," *J. Am. Ceram. Soc.*, vol. 74, no. 2, pp. 358–364, 1991, doi: 10.1016/j.apsusc.2017.03.145.

[67] Ü. Özgür *et al.*, "A comprehensive review of ZnO materials and devices," *J. Appl. Phys.*, vol. 98, no. 4, pp. 1–103, 2005, doi: 10.1063/1.1992666.

[68] S. M. Chou, L. G. Teoh, W. H. Lai, Y. H. Su, and M. H. Hon, "ZnO:Al thin film gas sensor for detection of ethanol vapor," *Sensors*, vol. 6, no. 10, pp. 1420–1427, 2006, doi: 10.3390/s6101420.

[69] Y. Y. Villanueva, D. R. Liu, and P. T. Cheng, "Pulsed laser deposition of zinc oxide," *Thin Solid Films*, vol. 501, no. 1–2. pp. 366–369, 2006, doi: 10.1016/j.tsf.2005.07.152.

[70] S. Faÿ and A. Shah, "Zinc oxide grown by CVD process as transparent contact for thin film solar cell applications," in *Springer Series in Materials Science*, vol. 104, 2008, pp. 235–302.

[71] M. D. McCluskey and S. J. Jokela, "Defects in ZnO," *J. Appl. Phys.*, vol. 106, no. 7, 2009, doi: 10.1063/1.3216464.

[72] T. Tynell and M. Karppinen, "Atomic layer deposition of ZnO: A review," *Semicond. Sci. Technol.*,

vol. 29, no. 4, 2014, doi: 10.1088/0268-1242/29/4/043001.

[73] Z. Jiwei, Z. Liangying, and Y. Xi, “Dielectric properties and optical propagation loss of c-axis oriented ZnO thin films deposited by sol-gel process,” *Ceram. Int.*, vol. 26, no. 8, pp. 883–885, 2000, doi: 10.1016/S0272-8842(00)00031-6.

[74] R. W. Dreyfus, Roger Kelly, and R. E. Walkup, “Laser-induced fluorescence studies of excimer laser ablation of Al2O3,” Appl. Phys. Lett. 49, 1478 (1986),

[75] S. A. Veldhuis, P. Brinks, T. M. Stawski, O. F. Göbel, and J. E. Ten Elshof, “A facile method for the density determination of ceramic thin films using X-ray reflectivity,” *J. Sol-Gel Sci. Technol.*, vol. 71, no. 1, pp. 118–128, 2014, doi: 10.1007/s10971-014-3336-2.

[76] M. Birkholz, *Thin Film Analysis by X-Ray Scattering*.Wiley 2006.

[77] M. Björck and G. Andersson, “GenX: An extensible X-ray reflectivity refinement program utilizing differential evolution,” *J. Appl. Crystallogr.*, vol. 40, no. 6, pp. 1174–1178, 2007, doi: 10.1107/S0021889807045086.

[78] B. L. Henke and E.M. Gullikson, “X-Ray interactions: Photoabsorption, Scattering,Transmission and reflection,” *Atomic Data and Nuclear Data Tables*, vol. 54, no. 2. pp. 181–342, 1993, doi: 10.1006/adnd.1993.1013.

[79] G. Vignaud and A. Gibaud, “REFLEX: A program for the analysis of specular X-ray and neutron reflectivity data,” *J. Appl. Crystallogr.*, vol. 52, pp. 201–213, 2019, doi: 10.1107/S1600576718018186.

[80] L. R. B. Elton and D. F. Jackson, “X-Ray Diffraction and the Bragg Law,” *Am. J. Phys.*, vol. 34, no. 11, pp. 1036–1038, 1966, doi: 10.1119/1.1972439.

[81] D. C. Sinclair and A. R. West, “Impedance and modulus spectroscopy of semiconducting $BaTiO_3$ showing positive temperature coefficient of resistance,” *J. Appl. Phys.*, vol. 66, no. 8, pp. 3850–3856, 1989, doi: 10.1063/1.344049.

[82] C. Århammar *et al.*, “Unveiling the complex electronic structure of amorphous metal oxides,” *Proc. Natl. Acad. Sci. U. S. A.*, vol. 108, no. 16, pp. 6355–6360, 2011, doi: 10.1073/pnas.1019698108.

[83] M. Choi, A. Janotti, and C. G. Van De Walle, “Native point defects and dangling bonds in α-Al_2O_3,”

J. Appl. Phys., vol. 113, no. 4, 2013, doi: 10.1063/1.4784114.

[84] B. Karunagaran, S. J. Chung, E. K. Suh, and D. Mangalaraj, "Dielectric and transport properties of magnetron sputtered titanium dioxide thin films," *Phys. B Condens. Matter*, vol. 369, no. 1–4, pp. 129–134, 2005, doi: 10.1016/j.physb.2005.08.006.

[85] R. D. Gould and A. K. Hassan, "A.c. electrical properties of thermally evaporated thin films of copper phthalocyanine," *Thin Solid Films*, vol. 223, no. 2, pp. 334–340, 1993, doi: 10.1016/0040-6090(93)90541-V.

[86] F. Argall and A. K. Jonscher, "Dielectric properties of thin films of aluminium oxide and silicon oxide," *Thin Solid Films*, vol. 2, no. 3, pp. 185–210, 1968, doi: 10.1016/0040-6090(68)90002-3.

[87] A. K. Jonscher, "FREQUENCY-DEPENDENCE OF CONDUCTIVITY IN HOPPING SYSTEMS," *J. Non. Cryst. Solids*, vol. 10, pp. 293–315, 1972.

[88] Y. N. Novikov, V. A. Gritsenko, and K. A. Nasyrov, "Charge transport mechanism in amorphous alumina," *Appl. Phys. Lett.*, vol. 94, no. 22, pp. 2007–2010, 2009, doi: 10.1063/1.3151861.

[89] G. Blaise, "Charge localization and transport in disordered dielectric materials," *J. Electrostat.*, vol. 50, no. 2, pp. 69–89, 2001, doi: 10.1016/S0304-3886(00)00027-9.

[90] A. I. Lakatos and M. Abkowitz, "Electrical properties of amorphous Se, As_2Se_3, and As_2S_3," *Phys. Rev. B*, vol. 3, no. 6, pp. 1791–1800, 1971, doi: 10.1103/PhysRevB.3.1791.

[91] Fabio Evangelisti, Michael Stiefel1 , Olga Guseva et al "Electronic and structural characterization of barrier-type amorphous aluminium oxide," *Electrochimica Acta*, vol. 224. pp. 503–516, 2017, doi: 10.1016/j.electacta.2016.12.090.

[92] M. Y. Yang, K. Kamiya, and K. Shiraishi, "Interstitial oxygen induced Fermi level pinning in the Al2O 3-based high-k MISFET with heavy-doped n-type poly-Si gates," *AIP Adv.*, vol. 3, no. 10, 2013, doi: 10.1063/1.4825071.

[93] L. G. Parratt, "Surface studies of solids by total reflection of x-rays," *Phys. Rev.*, vol. 95, no. 2, pp. 359–369, 1954, doi: 10.1103/PhysRev.95.359.

[94] M. Kisa, T. K. Minton, and J. C. Yang, "Structural comparisons of Si Ox and SiSi Ox formed by the exposure of silicon (100) to molecular oxygen and to hyperthermal atomic oxygen," *J. Appl. Phys.*, vol. 97, no. 2, 2005, doi: 10.1063/1.1835540.

[95] G. Y. Cho, S. Noh, Y. H. Lee, S. Ji, and S. W. Cha, "Study of Y_2O_3 Thin Film Prepared by Plasma Enhanced Atomic Layer Deposition," *ECS Trans.*, vol. 64, no. 9, pp. 15–21, 2014, doi: 10.1149/06409.0015ecst.

[96] M.H. Cho *et al.*, "Structural and electrical characteristics of Y_2O_3 films grown on oxidized Si(100) surface," *J. Vac. Sci. Technol. A Vacuum, Surfaces, Film.*, vol. 19, no. 1, pp. 192–199, 2001, doi: 10.1116/1.1331296.

[97] Y. P. Zhao, G. C. Wang, T. M. Lu, G. Palasantzas, and J. T. M. De Hosson, "Surface-roughness effect on capacitance and leakage current of an insulating film," *Phys. Rev. B - Condens. Matter Mater. Phys.*, vol. 60, no. 12, pp. 9157–9164, 1999, doi: 10.1103/PhysRevB.60.9157.

[98] A. Travlos, N. Boukos, G. Apostolopoulos, and A. Dimoulas, "Oxygen vacancy ordering in epitaxial layers of yttrium oxide on Si (001)," *Appl. Phys. Lett.*, vol. 82, no. 23, pp. 4053–4055, 2003, doi: 10.1063/1.1581985.

[99] H. J. Quah and K. Y. Cheong, "Deposition and post-deposition annealing of thin Y_2O_3 film on n-type Si in argon ambient," *Mater. Chem. Phys.*, vol. 130, no. 3, pp. 1007–1015, 2011, doi: 10.1016/j.matchemphys.2011.08.024.

[100] J. F. Verweij and J. H. Klootwijk, "Dielectric breakdown I: A review of oxide breakdown," *Microelectronics J.*, vol. 27, no. 7, pp. 611–622, 1996, doi: 10.1016/0026-2692(95)00104-2.

[101] V. Craciun, J. Elders, J. G. E. Gardeniers, and I. W. Boyd, "Characteristics of high quality ZnO thin films deposited by pulsed laser deposition," *Appl. Phys. Lett.*, vol. 65, no. 23, pp. 2963–2965, 1994, doi: 10.1063/1.112478.

[102] Z. Ghorannevis, M. T. Hosseinnejad, M. Habibi, and P. Golmahdi, "Effect of substrate temperature on structural, morphological and optical properties of deposited Al/ZnO films," *J. Theor. Appl. Phys.*, vol. 9, no. 1, pp. 33–38, 2015, doi: 10.1007/s40094-014-0157-1.

[103] R. Ondo-Ndong, G. Ferblantier, F. Pascal-Delannoy, A. Boyer, and A. Foucaran, "Electrical properties of zinc oxide sputtered thin films," *Microelectronics J.*, vol. 34, no. 11, pp. 1087–1092, 2003, doi: 10.1016/S0026-2692(03)00198-8.

[104] A. Kohan, G. Ceder, D. Morgan, and C. G. Van de Walle, "First-principles study of native point defects in ZnO," *Phys. Rev. B - Condens. Matter Mater. Phys.*, vol. 61, no. 22, pp. 15019–15027,

2000, doi: 10.1103/PhysRevB.61.15019.

[105] Paul H. Kasai, “Electron spin resonance studies of donors and acceptors in ZnO,” *Phys. Rev.*, vol. 130, no. 3, pp. 989–995, 1963, doi: 10.1103/PhysRev.130.989.

[106] J. López *et al.*, “Al_2O_3-Y_2O_3 ultrathin multilayer stacks grown by atomic layer deposition as perspective for optical waveguides applications,” *Opt. Mater. (Amst).*, vol. 72, pp. 788–794, 2017, doi: 10.1016/j.optmat.2017.07.011.

[107] E. G. Lizarraga-Medina *et al.*, “Al_2O_3-Y_2O_3 nanolaminated slab optical waveguides by atomic layer deposition,” *Opt. Mater. (Amst).*, vol. 103, no. March, pp. 3–8, 2020, doi: 10.1016/j.optmat.2020.109822.

[108] K. Y. Lin *et al.*, “Enhancement of effective dielectric constant using high-temperature mixed and sub-nano-laminated atomic layer deposited Y_2O_3/Al_2O_3 on GaAs(001),” *Microelectron. Eng.*, vol. 178, pp. 271–274, 2017, doi: 10.1016/j.mee.2017.05.018.

[109] J. López *et al.*, “Influence of the bilayer thickness on the optical properties of Al_2O_3-Y_2O_3 dielectric nanolaminate films grown by thermal atomic layer deposition,” *Mater. Res. Bull.*, vol. 87, pp. 14–19, 2017, doi: 10.1016/j.materresbull.2016.11.008.

[110] J. Li, M. Liu, and X. Bi, “Interface electron polarization based high-k Al_2O_3/ZnO nanolaminates with excellent temperature stability and ultrahigh energy-storage density by atomic layer deposition,” *J. Mater. Chem. A*, vol. 7, no. 17, pp. 10303–10318, 2019, doi: 10.1039/c9ta01487j.

[111] A. Janotti and C. G. Van De Walle, “Native point defects in ZnO,” *Phys. Rev. B - Condens. Matter Mater. Phys.*, vol. 76, no. 16, pp. 1–22, 2007, doi: 10.1103/PhysRevB.76.165202.

[112] W. R. Liu *et al.*, “Domain matching epitaxial growth of high-quality ZnO film using a Y_2O_3 buffer layer on Si (111),” *Cryst. Growth Des.*, vol. 9, no. 1, pp. 239–242, 2009, doi: 10.1021/cg8003849.

[113] J. Li and X. Bi, “Temperature- and frequency-dependent dielectric behaviors of insulator/semiconductor (Al2O3/ZnO) nanolaminates with various ZnO thicknesses,” *J. Phys. D. Appl. Phys.*, vol. 49, no. 28, 2016, doi: 10.1088/0022-3727/49/28/285301.

[114] A. A. Chaaya *et al.*, “Tuning optical properties of Al_2O_3/ZnO nanolaminates synthesized by atomic layer deposition,” *J. Phys. Chem. C*, vol. 118, no. 7, pp. 3811–3819, 2014, doi: 10.1021/jp411970w.

[115] R. Viter *et al.*, “Optical properties of ultrathin Al_2O_3/ZnO nanolaminates,” *Thin Solid Films*, vol. 594, pp. 96–100, 2015, doi: 10.1016/j.tsf.2015.10.018.

[116] W. Li, Z. Chen, R. N. Premnath, B. Kabius, and O. Auciello, “Controllable giant dielectric constant in AlOx/TiOy nanolaminates,” *J. Appl. Phys.*, vol. 110, no. 2, 2011, doi: 10.1063/1.3603002.

[117] L. P. B. Lima, J. A. Diniz, I. Doi, and J. Godoy Fo, “Titanium nitride as electrode for MOS technology and Schottky diode: Alternative extraction method of titanium nitride work function,” *Microelectron. Eng.*, vol. 92, pp. 86–90, 2012, doi: 10.1016/j.mee.2011.04.059.

[118] N. In Sang Jeon, Jaehoo Park, Dail Eom, Cheol Seong Hwang, Hyeong Joon Kim, Chan Jin Park, Hoon Young Cho, Jong-Ho Lee, “Post-Annealing Effects on Fixed Charge and Slow/Fast Interface States of TiN/Al2O3/p-Si Metal–Oxide–Semiconductor Capacitor,” *Jpn. J. Appl. Phys.*, vol. 42, no. 12, p. 1222, 2003, doi: 10.1088/0268-1242/2/12/008.